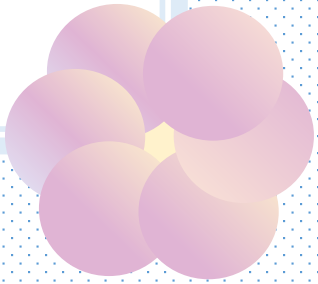




ANNUAL REPORT

2020



Kansai Photon Science Institute
Quantum Beam Science Research Directorate
National Institutes for
Quantum and Radiological Science and Technology

KPSI
ANNUAL
REPORT
2020

Contents

Preface	1
Activities of KPSI	3
User Facilities	9
Research Highlights	15
Publication Lists	55
The Kids' Science Museum of Photons	67
Appendix	71

はじめに

本年報では、関西光科学研究所(以下、関西研)において 2020 年度に実施された研究開発の主だった成果を紹介しています。関西研は国立研究開発法人量子科学技術研究開発機構(以下、量研)の研究開発拠点であり、けいはんな学研都市にある京都府木津地区と兵庫県播磨地区の 2 か所の研究サイトにおいて、量研における関西研のミッションである「レーザーや放射光による光科学技術の研究開発」を推進しています。木津地区では、世界トップレベルの高強度レーザー技術を基盤としたレーザー加速や X 線発生等のレーザー駆動の新しい放射線源開発、レーザーの短パルス性を活かした超高速計測技術開発、そして放射線影響や創薬に資する量子生命科学の最先端の研究開発を実施しています。また、播磨地区では、大型放射光施設 SPring-8 の 2 本の専用ビームライン等を活用した最先端の物質材料科学研究を展開するとともに、宮城県仙台市に設置が進められている次世代放射光施設の装置開発を行っています。

2020 年度は新型コロナウイルスの影響で、実験施設の約 3 ヶ月の運転停止や、研究所に併設するきつづ光科学館ふおとんが 1 年間通じて閉館するなど、多大な影響を受けましたが、所員一同の頑張りで、いくつかの素晴らしい研究成果を上げることができました。木津地区のレーザー科学分野においては、量子メス用のインジェクター実現に向けたレーザーシステム開発とそれを用いた炭素イオン加速実験の着実な進展や、J-KAREN レーザーを用いた実験により TNSA 法によるイオン加速機構のより深い理解が得られました。また超高速電子ダイナミクス研究においては、新しい化学反応経路の可視化の成功や、高密度電子が作る飛翔鏡によるテラヘルツ光のパルス圧縮や波長変換に向けた新しい試みなど、興味深い成果が出されています。量子生命科学領域においては、分子動力学シミュレーションを駆使したヌクレオソーム DNA や RNA 等の構造解析(予測)、クラスターDNA 損傷の空間分布の特性解明や損傷からの新しい突然変異生成経路の発見などの成果が生まれています。また、播磨地区においても、BL-14B1 の X 線回折計を用いた Co_3Ti 合金の高圧下での新規水素化物生成の詳細な観察や、磁性材料中の鉄原子からの蛍光 X 線の偏光状態を定量的に評価するための理論の確立など、数多くの優れた成果を挙げています。さらに、光技術の実用化についても、レーザーによるトンネル検査技術が国土交通省の技術カタログに掲載されるなど着実な進展を見せています。

関西研は、「光」を通じた我が国の量子科学技術の発展とイノベーション戦略に貢献する開かれた研究拠点としての役割を果たすべく、今後とも職員一同、より一層努力してまいります。皆様のご理解・ご協力を宜しくお願い申し上げます。

2021 年吉日
関西光科学研究所
所長 河内 哲哉



Preface

This annual report from the Kansai Photon Science Institute (KPSI) provides highlights on the scientific and technical research that was conducted over the 2020 fiscal year (FY2020).

KPSI is one of the research and development (R&D) bases of the National Institutes for Quantum and Radiological Science and Technology (QST). At KPSI's two R&D sites—the Kizu site in Keihanna Science City in Kyoto Prefecture and the Harima site in Hyogo Prefecture—R&D in optical science and technology is promoted using lasers and synchrotron radiation, which is the mission of the KPSI at QST. At the Kizu site, we are conducting cutting-edge research such as developing new types of laser-driven radiation sources based on world-class high-intensity laser technology, development of an ultrafast measurement methodology using ultrashort pulse technology, and quantum life science research to understand radiation effects and develop new medicines. At the Harima site, we are conducting state-of-the-art research in material science by utilizing the two beamlines (BL-14B1 and BL-11XU, SPring-8) at the synchrotron radiation facility SPring-8 and are developing equipment for the next-generation synchrotron radiation facility that is being constructed in Sendai, Miyagi Prefecture.

In FY2020, due to the influence of the new coronavirus COVID-19, the experimental facilities were shut down for about three months, and the Kids' Science Museum of Photon, which is attached to the research institute, was closed throughout the year. However, through the efforts of all the staff, we were able to achieve some wonderful research results. In the research field of laser science at the Kizu site, there has been steady progress in the development of a laser ion accelerator system and its use for carbon ion acceleration for the realization of quantum scalpels. Through experiments using the J-KAREN laser, we obtained deeper understanding of the ion acceleration mechanism in the TNSA scheme. In ultrafast electron dynamics, we successfully visualized new chemical reaction pathways and succeeded in new attempts to use a technique of flying mirror of high-density electrons for pulse compression and up-shift of terahertz radiation. In the field of quantum life-science, remarkable results have been produced, such as the structural analysis (prediction) of nucleosome DNA and RNA using molecular dynamics simulations, the elucidation of the spatial distribution of clustered DNA damage, and the discovery of a new mutation generation pathway due to the damage. In the research field of material science at the Harima site, we discovered new a hydride formation for the Co_3Ti alloy under high pressure using the x-ray diffractometer of BL-14B1 and established a theoretical framework for qualitatively evaluating the polarization of characteristic x-rays from iron atoms in magnetic materials. Furthermore, as an industrial application, the laser tunnel inspection technology has been adopted in the inspection support technology catalog of the Ministry of Land, Infrastructure, Transport, and Tourism.

KPSI will continue to fulfill its role as an open research center of the "science of light" and will contribute to quantum science and technology and the innovation strategy for Japan. We appreciate your understanding and cooperation.

Good day, 2021

KAWACHI Tetsuya., Director General of KPSI

Activities of KPSI

関西光科学研究所の主な動き

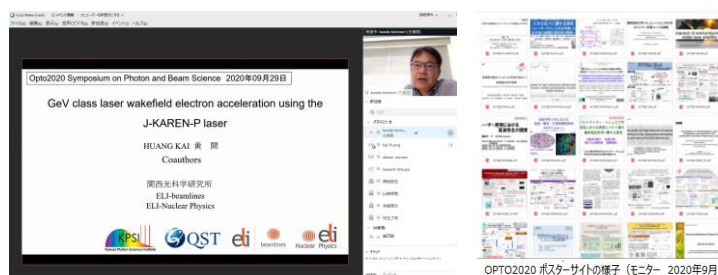
【シンポジウム・研究会の開催等】

2020年9月29日

「光・量子ビーム科学合同シンポジウム
2020（第5回）」開催

（Web開催・ポスターセッション：9月
18-29日）

大阪大学と量研との間で締結された包括協定に基づき、合同シンポジウムを開催しました。参加者は約200名、招待講演・口頭発表、ポスター発表、若手ポスター賞表彰、大阪大学近藤賞受賞記念講演、意見交換会が行われました。



左：招待講演（Web）Dr. Kai Huang, QST
右：ポスターセッション（Web入口画像）

2020年11月3日・文化の日

「セルゲイ ブラノフ上席研究フェローの外国人叙勲（旭日小綬章）」
功績概要：“科学技術分野における 日本の国際貢献の向上 に寄与”

令和2年度（2020年度）秋の叙勲において、QSTの上席研究フェローである Sergey Bulanov 博士が、外国人叙勲（Conferment of Decorations on Foreign Nationals）を受章される荣誉に浴されました。QSTからは平野俊夫理事長、関西光科学研究所有志によるビデオメッセージを作成しお祝いをお伝えしました。



左：平野俊夫理事長ビデオメッセージ、右：KPSIでのお祝いメッセージ撮影（管理棟エントランス）

2020年11月4～6日

「第4回 QST 国際シンポジウム —量子物質科学からのイノベーション—

（4th QST International Symposium —Innovation from Quantum Materials Science—）開催

（現地及びオンライン開催）

今回のメインテーマは“quantum materials science”（量子材料科学）であり、特に焦点を当てるトピックを、量子センシング、量子ビームによる材料分析、スピントロニクス材料としました。

一部の講演を高崎量子応用研究所で行い、全ての講演をオンラインで視聴できるようにして開催されました。このシンポジウムを通して、参加者は量子材料科学の最前線を探訪し、研究活動の「Quantum Leap（飛躍的進歩）」につながるインスピレーションを得たことと思われます。

特に十倉好紀先生（東京大学・理化学研究所）の特別講演は、磁気スキルミオンの観測と物性解明など顕著な業績のお話で、前日文化功労者の顕彰式があったばかりということもあり、聴衆に深い感銘を与えるものでした。

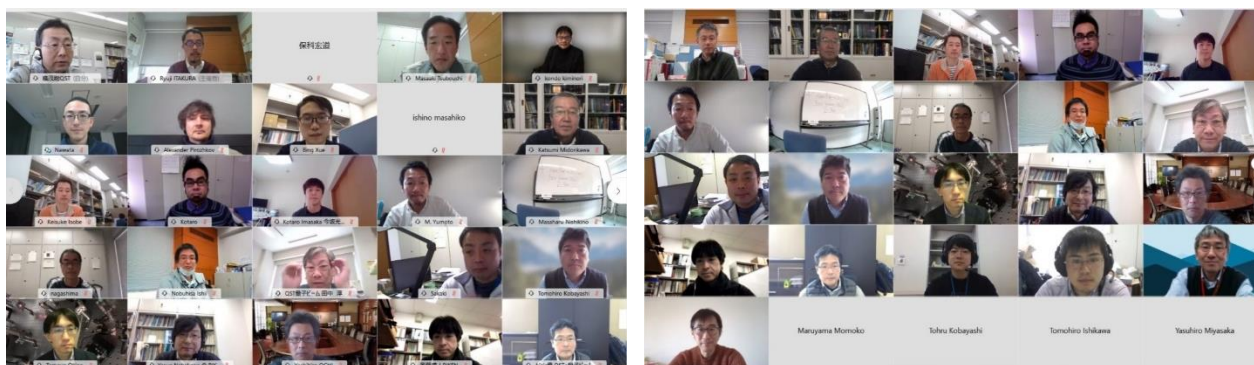


第4回 QST 国際シンポジウムポスター

2021年2月3日

「第4回 理研光量子工学研究センター・量研関西光科学研究所合同セミナー」（Web 開催）

本合同セミナーも第4回（4年目）を迎えました。昨年からの合宿形式となり、今回もその予定でしたが、新型コロナウイルス感染症の影響で他の行事と同様、オンライン開催としました。参加者は40名を越え、中堅から若手の計10名の方から、レーザー開発、イオンビームや中性子ビーム発生、テラヘルツ発生と利用、生命科学への展開についてご講演頂きました。



Web 上での参加者集合写真撮影（2021年2月3日）※一部、両方に写っている方もおります。

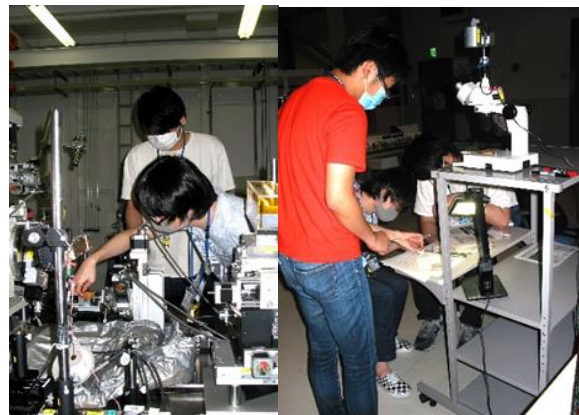
【主な出展等イベント】

QST 関西光科学研究所では、2020年度は新型コロナウイルス感染症拡大による影響があり、対面での活動の縮小を余儀なくされました。そのような状況下ではありましたが、新しく始まった Web 活用による研究成果紹介や展示、動画配信を行いました。

- 7月12～15日 「第20回 SPring-8 夏の学校」開催（大型放射光施設 SPring-8、兵庫県佐用町）
- 7月20、21日 「姫路・桜山公園まつり 科学の屋台村」出展 姫路市桜山公園（兵庫県姫路市）
- 10月17日 「播磨高原東中学校出前授業」（播磨科学公園都市、兵庫県たつの市）
- 10月27、28日 「京都スマートシティエキスポ2020」、「第14回けいはんなビジネスメッセ2020」同時開催へ出展（Web開催）
- 11月5～7日 「けいはんな R&D フェア（第1回）」出展（Web開催）



第20回 SPring-8 夏の学校参加者の全体集合写真
2020.7.14（写真提供：高輝度光科学研究センター）



SPring-8 QST ビームライン:BL11XU での実習の様子

プレスリリース（研究成果）

1) フェムト秒レーザー光の高次高調波によって薄膜の微細加工に成功！

— 極端紫外光の回折限界集光が拓く微細加工の最前線 — （2020年5月15日）

<https://www.qst.go.jp/site/press/40919.html>

論文タイトル：Surface processing of PMMA and metal nano-particle resist by sub-micrometer focusing of coherent extreme ultraviolet high-order harmonics pulses

2) 発光による衝突後効果の変化を利用するアト秒「ストップウォッチ」

— 原子の内殻過程をアト秒で追及する新しい手法 — （2020年5月29日）

<https://www.qst.go.jp/site/press/41136.html>

論文タイトル：Fluorescence Time Delay in Multistep Auger Decay as an Internal Clock

3) テラヘルツ光照射による細胞内タンパク質重合体の断片化

— THz パルス光が衝撃波として生体内部へ到達する可能性を発見 — （2020年6月2日）

<https://www.qst.go.jp/site/press/41250.html>

論文タイトル：Propagation of THz irradiation energy through aqueous layers: Demolition of actin filaments in living cells

- 4) レーザー光による固体内電子運動の操作で光の発生制御に成功
— 超高速な光制御・スイッチング素子や新しい光源の開発に期待 — (2020年6月17日)
<https://www.qst.go.jp/site/press/41693.html>
論文タイトル: Modifying angular and polarization selection rules of high-order harmonics by controlling electron trajectories in k-space
- 5) 高強度のレーザー光による世界最大の電場発生を実証
— 重イオン加速器の飛躍的な小型化に期待 — (2020年7月16日)
<https://www.qst.go.jp/site/press/42392.html>
論文タイトル: Dynamics of laser-driven heavy-ion acceleration clarified by ion charge states
- 6) 光と固体の量子力学的な相互作用による新たな光の発生機構を解明
— 高次高調波光の発生機構の解明に向けた新たな知見 — (2020年7月29日)
<https://www.qst.go.jp/site/press/42650.html>
論文タイトル: Role of virtual band population for high harmonic generation in solids
- 7) 物体内部のらせん構造の向きを識別する X 線顕微鏡
— 高性能機能材料デバイスで生じる X 線光渦を用いた新しい観察法 — (2020年7月31日)
<https://www.qst.go.jp/site/press/42631.html>
論文タイトル: X-ray microscope for imaging topological charge and orbital angular momentum distribution formed by chirality
- 8) 長波長赤外での強光子場の実現とアト秒 X 線源の開発に大きく前進
— 共振器型自由電子レーザーの世界最高変換効率を達成 — (2020年10月6日)
<https://www.qst.go.jp/site/press/44450.html>
論文タイトル: Record high extraction efficiency of free electron laser oscillator
- 9) テラヘルツ光が姿を変えて水中を伝わる様子の観測に成功!
— これまでの常識を覆すテラヘルツ光の新たな活用法として期待 — (2020年10月28日)
<https://www.qst.go.jp/site/press/45262.html>
論文タイトル: Plane photoacoustic wave generation in liquid water using irradiation of terahertz pulses
- 10) 分子内を歩き回る水素の姿を捉えた!
— 化学反応の新しいルート「ローミング過程」の可視化に成功 — (2020年11月27日)
<https://www.qst.go.jp/site/press/46129.html>
論文タイトル: Capturing roaming molecular fragments in real time

1 1) 鉄の磁石の「表面の謎」を解明!

— 一原子層単位の深さ精度で磁性探査する新技術を開発 — (2020年12月4日)

<https://www.qst.go.jp/site/press/46399.html>

論文タイトル: Magnetic Friedel Oscillation at the Fe(001) Surface: Direct Observation by Atomic-Layer-Resolved Synchrotron Radiation ^{57}Fe Mössbauer Spectroscopy

1 2) 高性能な磁石や磁性材料の開発へ

— X線磁気発光分光学の幕開け「X線磁気円偏光発光」のメカニズムを理論的に解明 — (2020年12月23日)

<https://www.qst.go.jp/site/press/46994.html>

論文タイトル: Effects of conduction electron excitation on x-ray magnetic circularly polarized emission in itinerant ferromagnets

1 3) 遺伝子発現のカギはDNAのねじれ方

— ヌクレオソームの全原子の挙動を計算、DNAの性質を明らかに — (2021年2月9日)

<https://www.qst.go.jp/site/press/20210209.html>

論文タイトル: Torsional stress can regulate the unwrapping of two outer half superhelical turns of nucleosomal DNA

User Facilities

主要な施設・装置

木津地区

○J-KAREN-P レーザー装置

【装置概要】

世界トップクラスの極短パルス超高強度レーザーです。最大 30 J のレーザーエネルギーを 30 フェムト秒 (1 フェムトは 1000 兆分の 1) の時間に閉じ込めることにより 1000 兆ワットの超高強度を実現します。(右の写真は強力な励起レーザーの光で緑色に光っています。)



【供給装置性能】

- ・ターゲット照射エネルギー：~10 J/pulse
- ・コントラスト比： $<10^{-11}$ (プラズマミラー建設中)
- ・中心波長：810 nm
- ・繰り返し：0.1 Hz ~ シングルショット
- ・パルス幅：30~50 フェムト秒
- ・集光強度： $\sim 10^{20}\text{-}10^{22}$ W/cm²

上記以外のパラメータもお問い合わせ下さい

【主要な研究課題】

レーザー高度化技術開発、イオン、電子、X線等の量子ビーム源開発

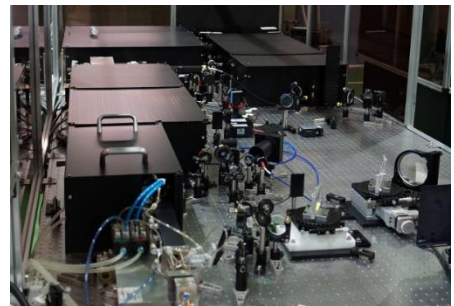
○QUADRA-T レーザーシステム

【装置概要】

1秒間に3000発のレーザーパルスが繰り返せる高平均出力ピコ秒パルスレーザーです。

【装置性能】

- ・照射エネルギー：10 mJ/pulse
- ・波長：1030 nm
- ・繰り返し：3 kHz
- ・パルス幅：約 1 ピコ秒



【主要な研究課題】

高繰り返し高出力レーザー (パラメトリック増幅器等) の開発、高強度テラヘルツ光源の開発

播磨地区

播磨地区では大型放射光施設 SPring-8 に 2 本の QST 専用ビームラインを設置しているほか、日本原子力研究開発機構 (JAEA) の専用ビームラインにも複数の放射光専用実験装置を常設しています。一方で、QST 専用ビームラインにも、JAEA の専用実験装置が常設されています。

○BL11XU (QST 極限量子ダイナミクス I ビームライン)

【装置概要】

SPring-8 標準の真空封止アンジュレータを光源とし、マルチ結晶交換システムを装備することで、広範囲のエネルギー領域の高輝度放射光 X 線を高効率に利用できるビームラインです。

【装置性能】

- ・光源：真空封止アンジュレータ
- ・エネルギー領域：6～70 keV
- ・分光結晶：Si(111)、Si(311)
- ・実験装置：放射光メスバウアー分光装置、共鳴非弾性 X 線散乱装置、及び表面 X 線回折計

1. 放射光メスバウアー分光装置

^{57}Fe 、 ^{61}Ni 等のメスバウアー核種を対象とした放射光メスバウアー分光が可能で、物質の電子、磁気状態から格子振動状態に関する情報などを得ることができます。

2. 共鳴非弾性 X 線散乱装置

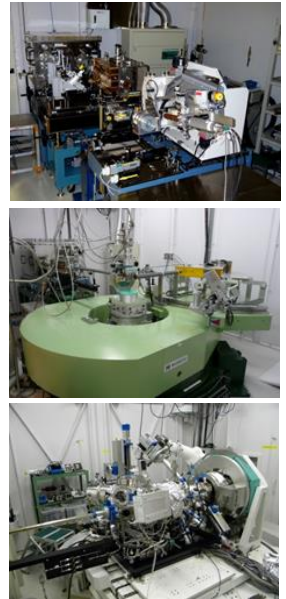
2m 長アームに搭載した球面湾曲型集光式アナライザー結晶による背面反射を用いることで、高分解能の X 線分光を行い、散乱光の方位や入射光とのエネルギー差から、運動量移行を伴う固体内素励起が観察できます。

3. 表面 X 線回折計

分子線エピタキシー (MBE) チェンバーを搭載した表面構造解析用装置で、窒化物を含む半導体結晶などの成長過程を、X 線回折法を用いてその場観察・リアルタイム観察することができます。

【主要な研究課題】

金属薄膜の原子層単位での磁性探査、白金系燃料電池触媒の電子状態解析、半導体量子ドットや半導体多層膜の成長過程のリアルタイム解析



○BL14B1 (QST 極限量子ダイナミクス II ビームライン)

【装置概要】

偏向電磁石を光源とすることで、連続スペクトルを持つ白色 X 線や高エネルギーの単色 X 線が利用可能なビームラインです。全反射ミラーや分光結晶の曲げ機構によって、試料位置への集光が可能となっています。

【装置性能】

- ・光源：偏向電磁石
- ・エネルギー領域：白色 X 線 (5～150 keV)、単色 X 線 (5～90 keV)
- ・実験装置：高温高圧プレス装置、汎用四軸 X 線回折計及び分散型 XAFS 測定装置 (JAEA)

1. 高温高圧プレス装置

高温高圧の条件下にある試料を、白色 X 線を用いたエネルギー分散型 X 線回折法やラジオグラフィ法、単色 X 線を用いた XAFS (X 線吸収微細構造) 法や角度分散型 X 線回折法によって調べることができます。

【主要な研究課題】

高圧下での金属水素化物形成過程のその場観察



2. 汎用四軸 X 線回折計

令和 2 年 3 月に RI 実験棟から移設。令和 2 年度はビーム利用実験に向けた調整・予備実験等を実施。高エネルギー単色 X 線を利用した回折法により、大型構造材料中の応力・ひずみ、結晶方位分布計測ができます。

【主要な研究課題】

応力・ひずみ、結晶方位の三次元分布測定、及び照射実験等、様々な研究に活用予定。



○BL22XU (JAEA 専用ビームライン) における放射光専用実験装置

1. ダイヤモンドアンビルセル回折計 (JAEA BL22XU)

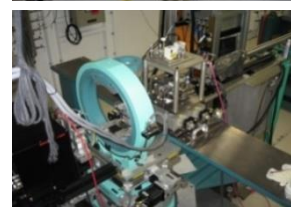
大型イメージングプレート検出器と高エネルギー X 線を利用することにより、高圧下での単結晶 X 線回折及び粉末 X 線回折実験、X 線全散乱測定及び原子二体分布関数 (PDF) 解析が可能な装置です。

2. 大型 X 線回折計

共鳴 X 線散乱による電子軌道状態の観測、スペックル回折によるドメイン構造の研究、応力・ひずみ分布測定などの回折マッピングなど多目的に利用する四軸回折計です。

【主要な研究課題】

水素貯蔵合金の水素吸蔵過程の時分割その場 X 線回折測定、負の熱膨張材料、超伝導体、f 電子系化合物、コヒーレント X 線を利用したスペックル散乱によるナノドメイン観察。応力・ひずみの三次元分布測定、等



施設の稼働実績

○木津地区

2020 年度の運転時間は J-KAREN-P は 1436 時間、QUADRA-T は 1526 時間、その他装置は合計 1403 時間でした。J-KAREN-P は後期より、コントラスト比を上げるためのプラズマミラー導入作業を開始しました。

実施課題件数

装置名称	独自研究	受託研究	共同研究	施設共用
J-KAREN-P レーザー装置	3	1	0	2
QUADRA-T レーザーシステム	3	1	0	0
kHz チタンサファイアレーザー	5	2	1	0
X 線回折装置	1	0	1	0

○播磨地区

2020 年度の SPring-8 蓄積リングの運転時間は 5352 時間で、放射光利用時間はそのうちの 4536 時間でした。量研、原子力機構とも専用ビームラインでは 20%程度の調整時間と新型コロナウイルス感染拡大防止のための利用休止時間 (約 15%程度) を除き、放射光利用時間で独自研究や受託研究、外部利用者への施設共用と研究支援を行っています。

実施課題件数

ビームライン	独自研究	受託研究	共同研究	施設共用
BL11XU	4	0	1	11
BL14B1	6	0	3	9
BL22XU	1	0	2	7

利用日数

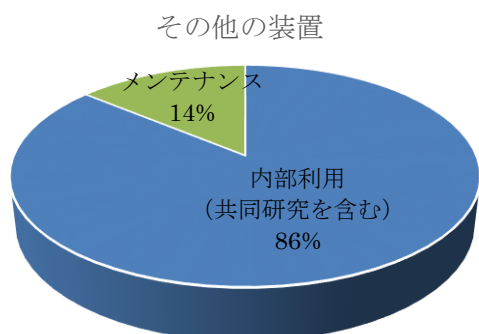
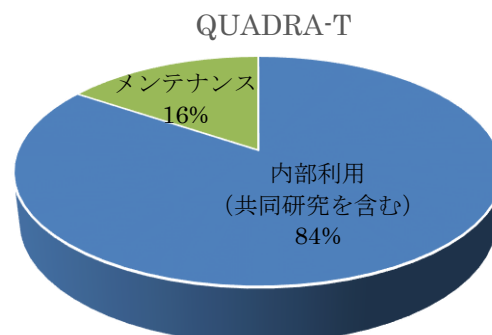
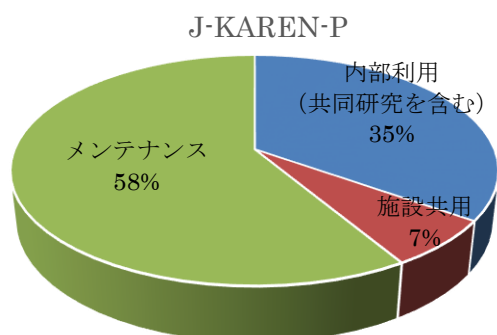
ビームライン	独自研究	受託研究	共同研究	施設共用
BL11XU	61	0	20	34
BL14B1	22	0	15	30
BL22XU	4	0	17	12

*件数、日数ともに QST の利用のみ

*日数は 3 シフトを 1 日とした。

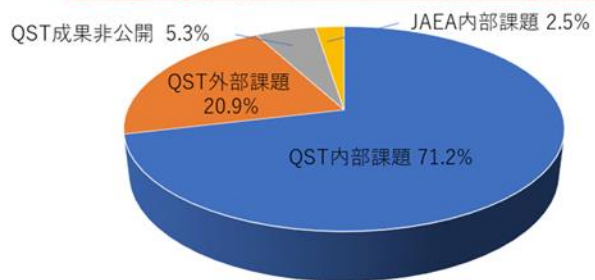
施設の利用状況

○木津地区

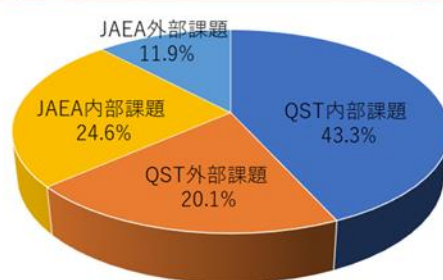


○播磨地区

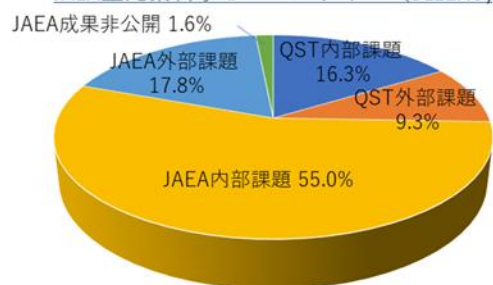
QST極限量子ダイナミクス I ビームライン (BL11XU)



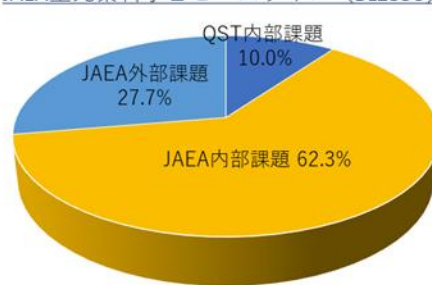
QST極限量子ダイナミクス II ビームライン (BL14B1)



JAEA重元素科学 I ビームライン (BL22XU)



JAEA重元素科学 II ビームライン (BL23SU)



Research Highlights

Advanced Photon Research Activities

Kiminori Kondo

Department of Advanced Photon Research



In the department of Advanced Photon Research, the primary research focus is the science and technology of advanced lasers. High-peak-power laser technology, high-repetition-rate and high-stability laser technology, and ultrashort-pulse technology are of particular importance. These technologies are developed in-house and applied to various objects. The largest laser system at the Kansai Photon Science Institute (KPSI) is the petawatt (PW)-class high-peak-power laser J-KAREN-P. This system has been upgraded since obtaining a supplementary budget in FY2012, and the lengthy commissioning operation was completed three years ago. Internal users at the KPSI and external users have used the system in its PW-class operation mode. In fiscal year 2020, 20% of the total machine time has been shared with external users, a decrease from 30% in FY2019. This decline in external usage results from a decline in the total machine time. The total machine time has been limited to maintain a sufficient duration for designing and constructing a large aperture plasma mirror system for J-KAREN-P. This includes an estimation of the beam quality by candidate suppliers. However, despite the original decline in external usage, some ion acceleration experiments have been postponed to the next fiscal year (FY2021) to compensate for the shutdown in FY2020 due to Covid-19, as can be imagined. Therefore, after the cancellation of the state of emergency, an extreme focused intensity of over 10^{21} W/cm² on targets with extremely high-contrast suppression of the optical component proceeding to the main pulse has been supplied to the users. This high-power laser infrastructure is maintained by the Laser Facility Operation Office, Advanced Laser Group, and High-Intensity Laser Science Group. The Advanced Laser Group not only maintains J-KAREN-P to

deliver optimal laser pulses, but also develops and introduces new technology to maintain J-KAREN-P in world-class conditions. Dr. Kiriya reports the investigation and improvement of pre-pulse generation by post-pulse in the J-KAREN-P laser system, which is important for producing high quality high-peak-power laser pulses. The High-Intensity Laser Science Group mainly studies laser-driven ion acceleration, laser electron acceleration, and relativistic high-order harmonic generation with J-KAREN-P at the KPSI.

One of the most important applications is the development of a laser-driven secondary radiation source. An extremely intense optical field can be formed by focusing an extremely high peak power to a small spot size. Atoms and molecules exposed to this extremely intense field are immediately ionized by field ionization. The corresponding optical intensity on the atomic unit is only 3×10^{16} W/cm², which is much lower than that generated with J-KAREN-P. The generated free electrons move along the extremely intense optical field, and ultra-relativistic quiver motion is induced. These energetic quivering electrons induce the generation of various secondary radiations. This suggests the possibility of a compact energetic quantum beam source without the use of conventional accelerator technology. If this technology is established and applied to various fields, a type of destructive innovation could occur. Dr. Nishiuchi explains the dynamics of laser-driven heavy-ion acceleration as clarified by ion charge states, which is key knowledge for developing a laser driven ion accelerator. For studying laser driven ion acceleration, the estimation of the spectrum of energetic electrons is a critical issue. These energetic electrons drive the extreme acceleration sheath

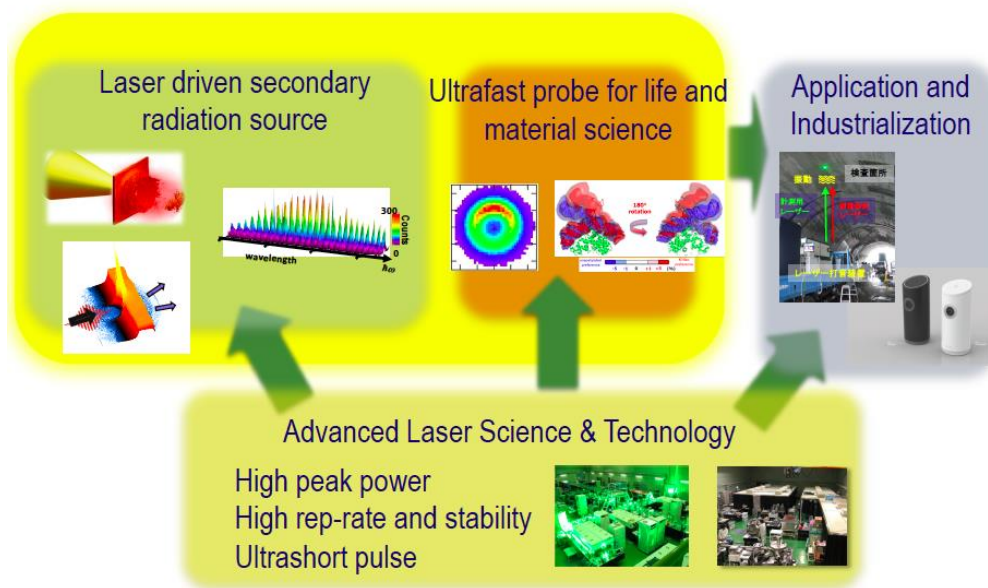


Fig.1 Research and development at the Department of Advanced Photon Research.

field at the rear side of a thin foil target. Dr. Sakaki created a new algorithm using L1 regularization for measuring electron energy spectra. He introduced this new algorithm to estimate a more realistic electron spectrum in the reconstruction of the spectrum from the experimentally obtained raw spectrum. One of the most important applications of laser-driven energetic particles are quantum scalpels, which is a new heavy-ion cancer therapy machine that is planned to be developed within the next six years. The development of a quantum scalpel is the one of the main projects at the National Institutes for Quantum and Radiological Science and Technology (QST). The injector of the quantum scalpel is based on the laser-driven carbon accelerator. The JST-MIRAI research and development program (large-scale type) began in November of 2017. The aim of this program is to demonstrate a proof of concept (POC). In addition to an ion accelerator, a laser plasma electron accelerator is also under development at the KPSI within the MIRAI program. In this program, the demonstration of a POC of the laser driven heavy ion injector must be shown by the end of FY2026. Therefore, the X-ray Laser Group shutdown the 0.1 Hz x-ray laser driver (TOPAZ) and began to develop a high quality 10 Hz x-ray laser driver in the previous fiscal year (FY2019). This system is based on a commercial 10 TW/10 Hz chirped pulse amplification (CPA) Ti:sapphire laser system. For stable operation, the front end of this system is based on a 100 Hz LD pump solid-state laser. By using a double CPA structure, very high quality 30 TW laser pulses will be generated not only for 10 Hz x-ray laser operation, but also for the stable ion beam generation for the MIRAI project. With this system, results that are more precise should be extracted in ion acceleration experiments using a suitable ion spectrometer. Dr. Kojima explains the development of a compact Thomson parabola spectrometer with a variable energy range that can measure the angular distribution of low-energy laser-driven accelerated ions. As an application of the intense x-ray laser, Dr. Ishino reports the soft x-ray laser beamline for surface processing and damage studies.

As mentioned above, the focused laser intensity of over 10^{21} W/cm² has been achieved with J-KAREN-P, while 10^{23} W/cm² has been reported by CoReLS in South Korea. One of the most challenging tasks in experimental research is achieving a Schwinger field of 10^{29} W/cm², in which a vacuum can be broken down to pair creation. Dr. Koga reports the creation of an electron-positron pair in electric fields generated by micro-bubble implosions. By using the novel idea of micro-bubble implosions, a Schwinger field might be generated.

Another important application of advanced laser science and technology is an ultrafast probe for life and material science. THz radiation is also mainly developed at the Ultrafast Dynamics Group for material science. Until three years ago, the C-Phost project had been performed by the Ultrafast Dynamics Group.

Strong THz radiation is generated with QUADRA-T, a kHz 10-mJ ps laser system. These radiation and laser systems are used for various ultrafast dynamics research. Dr. Tsubouchi reports on the relativistic Doppler reflection of terahertz light from a moving plasma front in an optically pumped Si wafer. Related to the study of ultrafast molecular science, Dr. Endo details the capture of roaming fragments from the dissociation of formaldehyde in real-time. He has analyzed the experimentally obtained Coulomb explosion images to demonstrate a new dissociation mechanism. For life science applications, a bright and stable short pulse laser system has been developed and applied to a two-photon microscope for observing the neuron dynamics in mouse brains at the National Institute of Radiological Sciences (NIRS). This research has demonstrated notable results after the unification of NIRS and JAEA four years ago. In this fiscal year, for probing a deeper part in brain, a three-photon microscope is under development following the previous fiscal year. Moreover, the ultrashort probe has been upgraded to the attosecond regime. The attosecond research at the KPSI could thus commence. The related study of CPS laser fabrication has also been ongoing. This research is supported by the Q-LEAP program, which started three years ago. This project will be undertaken by the Ultrafast Dynamics Group and the X-ray Laser Group. The X-ray Laser Group studies the interaction between intense x-rays and solid materials with the laser-plasma-based x-ray laser at the KPSI and SXFEL at SACLA. Intense x-ray fabrication is an important fine structure fabrication technology, which has advanced current laser fabrication technology.

In a manner, the most important application of our advanced laser science and technology is industrialization. The new SIP program for the development of nondestructive tunnel inspection technology began last year, following the previous SIP program that finished three years ago. This technology is being tested for its commercial application at the venture company Photon-Labo. One of the key tools of nondestructive tunnel inspections is the high-average-power high-repetition-rate intense laser technology. This technology is used for contact with the inner surface of the concrete tunnel to induce an acoustic wave inside the wall. To induce an acoustic wave with a sufficient amplitude, a 2-J pulse with a 10-Hz repetition rate system has been developed and successfully loaded onto an inspection vehicle. This technology is closely related to the development of high-average-power high-peak-power laser systems, which could be used in the laser-driven carbon ion injector in the quantum scalpel. Medical applications are an additional important consideration. By using high power laser technology, a strong and compact infrared laser can be developed for various medical uses including blood glucose measurements. Additionally, Dr. Aoyama presents the potential application of this technology to the field of pathology.

Clarification of the dynamics of laser-driven heavy-ion acceleration by ion charge states

Mamiko Nishiuchi

High Intensity Laser Science Group, Department of Advanced Photon Research



In the past decade since a fast high energy proton beam was observed from the interaction between a high power laser pulse and a solid density target, the majority of ion acceleration research has focused on low-Z ions, such as protons ($Z = 1$) or carbon ($Z = 6$) [1]. This is because the laser intensity was insufficient to expel the electrons around the heavy nuclei efficiently, which is a key requirement for the efficient acceleration of heavy ions by the laser. Recent progress in laser technology has produced petawatt (PW) lasers with focused intensity nearing 10^{22} W/cm² [2], whose laser field is strong enough to strip the electrons surrounding the heavy nuclei and accelerate the heavy ions towards higher energies [1]. These results greatly encourage the application of a compact heavy ion accelerator system, as conventional sources of low-Z ions are already relatively compact, and high-Z sources cannot achieve high energies and charge states, resulting in heavy-ion accelerator complexes being extremely large with unavoidable beam emittance growth.

To realize the applications, even higher Z and higher energy beams are required. Unfortunately, the ionization dynamics and the interplay with the acceleration mechanisms are far from being fully understood, as the laser-irradiated target is a highly non-equilibrium, dense, and high-energy density plasma in an unexplored parameter regime. Furthermore, target surface contaminants effectively shield the target ions, preventing efficient acceleration without special treatment.

Therefore, we investigated experimentally, analytically, and numerically the ionization and acceleration dynamics of highly charged silver ions from foils driven by a femtosecond PW-class laser pulse focused to a peak intensity of 5×10^{21} W/cm² [3]. By varying the silver foil thickness, the suppression of the maximum proton energy with thinner targets is demonstrated while simultaneously increasing the charge state and the maximum energies of the silver ions. With an optimum target thickness of 500 nm, high flux, highly charged, high-energy ions are observed, while for the thinnest target of 50 nm, the maximum charge state and energy increased while the flux is reduced and the acceleration is less controllable. Combining analytical considerations with numerical hydrodynamic and particle-in-cell (PIC) simulations, it is demonstrated that the surface contaminant at the rear surface is pre-accelerated and effectively blown off during the intrinsic relativistic rising edge in PW-class laser pulses, resulting in reduced contaminant ion energies and enhanced acceleration of bulk target ions. The bulk electron temperature in the target reached ~ 10 keV, resulting in significant ionization by collision of the silver M-shell and L-shell. These highly charged silver ions could subsequently be extracted by strong sheath fields of ~ 40 to 80 TV/m at the target rear, without being shielded by surface contaminants.

The simulations show that the increase in charge state from the thinnest targets is due to additional field ionization by the intense field of the laser as it bores through the target. Therefore, by careful observation of the ion charge state, we have been able to investigate the transition between collisional and field ionized

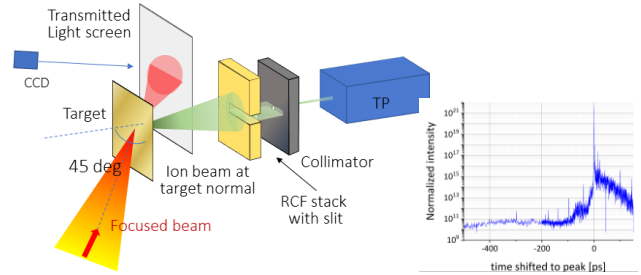


Fig. 1: (Left) Experimental set-up of experiment at J-KAREN-P and (Right) temporal contrast of the laser.

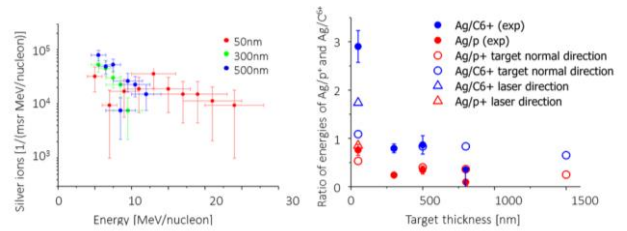


Fig. 2: (Left) Experimentally observed silver L-shell spectra for varying target thicknesses and (Right) the ratio of the maximum energy of silver ions to that of a fully stripped carbon (blue circles) or proton (red circles).

heavy-ion acceleration. The investigation of the ionization and acceleration mechanisms of highly charged ions therefore provides a path for improving the control and capabilities of laser-driven heavy-ion sources, a key component for next-generation heavy-ion accelerators.

The experiment was performed at the J-KAREN-P facility at the Kansai Photon Science Institute [4], as shown in Fig. 1 (left). The J-KAREN-P laser was focused onto a thin silver target with thicknesses ranging from 50 to 800 nm. The contrast of the laser was measured using a third order cross-correlator (Fig. 1 right), and used to simulate the pre-pulse expansion using a hydrodynamics code (FLASH). Radiochromic film (RCF) stacks measured the proton beam profile on a single shot basis along the target normal direction, 50 mm behind the target. A slit in the center of the RCF stacks allowed coexistence with a Thomson parabola (TP) for concurrent quantification of the ion spectra [5] in the target normal direction (Fig. 2).

Figure 2(left) shows the spectra of the highly charged silver ions (L-shell, $Z^* = 38-45$) detected with the TP for targets with thickness of 50, 300, and 500 nm, where Z^* denotes the ionization charge state. The highest maximum energy of the silver was found for the 50 nm target ($26(\pm 5)$ MeV/nucleon with $Z^* = 45(\pm 2)$), decreasing for the 300 and 500 nm foils to >10 MeV/u, with a Z^* of ~ 40 . For the 800 nm target, we could not unambiguously observe any signal from the silver ions in the energy range above the detection limit of 5 MeV/nucleon, setting an upper limit on the silver ion energies. However, in the energy

range of 5 to 10 MeV/nucleon a higher silver flux was observed with the 300 and 500 nm targets than for 50 nm. At the same time, the observed proton maximum energies on the RCF gradually decreased from ~ 47 MeV for the 800 nm target to ~ 35 MeV for the 50 nm target. Target thicknesses greater than 500 nm resulted in proton beams with smooth spatial distributions along the target normal, indicating that the acceleration mechanisms for the thicker target is dominated by target normal sheath acceleration (TNSA), which is also supported by the lack of observed transmitted light through the target. However, for thinner targets, the spatial uniformity of the proton beam worsened considerably, suggesting laser-pre-pulse-driven pre-expansion of the rear surface or a different acceleration mechanism. Figure 2(right) shows the ratio between the maximum energies of the silver and protons, and silver and C6+, indicated by red and blue points respectively. As the target thickness decreases, the ratio of silver ion energy to contaminant energy clearly increases.

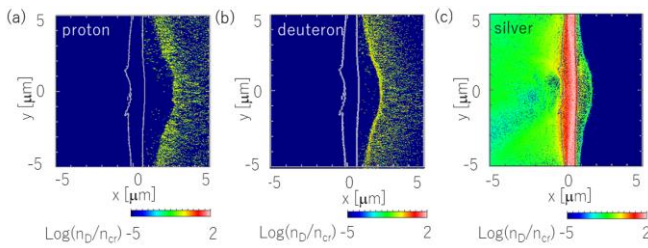


Fig. 3: Density distribution of the (a) protons, (b) deuterons, and (c) silver ions at the peak of the main pulse for the 500 nm silver target.

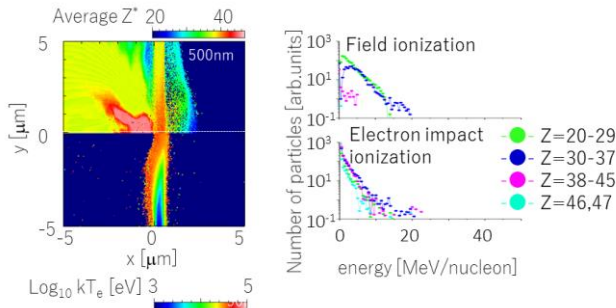


Fig. 4: In the left panel, the (upper) average charge state distributions and (lower) temperature distribution in the 500 nm target are shown, while in the right panel, the spectra of silver ions with a momentum $p_x > 0$ are shown. Those in the upper (lower) row are ions whose last ionization was due to field (electron impact) ionization.

The PIC simulation was performed to investigate the ionization mechanisms of the accelerated silver ions using the PICLS code [6]. The result of the hydrodynamical simulation was used as an input to the PIC simulation. Figure 3 shows the density distribution of the ions at the peak of the main pulse arrival, showing contaminants effectively detach from the target rear and moving over $\sim 2 \mu\text{m}$, where the density drops below the relativistic critical density γn_{cr} . However, the silver bulk is not significantly deformed and maintains a steep density profile on the rear surface with an electron density higher than γn_{cr} . Therefore, a large sheath field is, excited at the rear of the silver target instead of in the detached contaminant plasma. Its strength reaches 52 TV/m at maximum and takes 50 fs to decrease to 80 percent of the maximum. Figure 4 (left) shows the average silver charge state (upper) and bulk electron temperature distribution (lower) 35 fs after the main pulse arrival. The temperature of the bulk of the target rises to >10 keV, sufficient to collisionally

ionize the silver ions up to the L -shell, which was observed in the experiment.

However, the conditions differ drastically for the 50 nm target. The 50 nm target is strongly expanded by the pre-pulses and rising edge well before the main pulse arrives, although it remained initially opaque to the laser. The laser field ionized highly charged silver ions at the front of the target. These ions were pushed forward by the radiation pressure of the laser toward the target rear to be accelerated by the strong sheath field. The experimentally observed high charge states of silver cannot be only achieved by the field strength of the sheath field, requiring the laser field as well.

Even though we observe highly charged high-energy silver ions from the 50 nm target, the transition of the dominant acceleration scheme from TNSA to hole boring (HB) and TNSA is strongly dependent on the rising edge of the main pulse, which is not easy to control even for state-of-the-art PW class lasers. A small change in target thickness or laser rising edge can significantly change the interaction and generated ion beam. Thus, for a stable source of highly charged high-energy ions with a good collimation, using a slightly thicker target and relying on the collisional ionization and extraction by the TNSA may be optimal for many applications.

In conclusion, we have investigated and elucidated the dynamics of ultra-intense laser-driven heavy-ion acceleration. Highly charged high-energy silver ions were accelerated by a short pulse petawatt class laser interacting with a silver target with an optimum thickness (500 nm), with ionization being dominated by electron collisional ionization inside the target, which was heated to over ~ 10 keV by high-intensity short laser pulses. However, for the higher energy silver ions generated by the thinnest targets, the dominant ionization process shifts to field ionization by the laser. In this case, the acceleration is the combination of hole boring driven by photon pressure at the target front- and the rear-side sheath field acceleration. This comprehensive understanding of laser-driven heavy ion acceleration dynamics paves the way for controlling the production of highly charged high-energy heavy-ion beams with PW class high-intensity short-pulse lasers.

Acknowledgments

The author would like to thank all the co-authors on the paper: N. P. Dover, M. Hata, H. Sakaki, Ko. Kondo, H. F. Lowe, T. Miyahara, H. Kiriya, J. K. Koga, N. Iwata, M. A. Alkhimova, A. S. Pirozhkov, A. Ya. Faenov, T. A. Pikuz, A. Sagisaka, Y. Watanabe, M. Kando, K. Kondo, E. J. Ditter, O. C. Ettlinger, G. S. Hicks, Z. Najmudin, T. Ziegler, K. Zeil, U. Schramm, and Y. Sentoku. The author is also grateful to the J-KAREN-P operations team for their support. This work was partially supported by the JST-Mirai Program Grant No. JPMJMI17A1, Japan. M.N. was supported by JST PRESTO Grant No. JPMJPR16P9 and Kakenhi Grant No. 16K05506. M.N. was supported by the QST President's Strategic Grant (QST International Research Initiative (AAA98)) and Creative Research (ABACS). M.N. and N.P.D. were supported by a JSPS Post-doctoral Fellowship and Kakenhi Project No. 15F15772. M.N. and H.S. were supported by the Mitsubishi Foundation (ID: 28131).

References

1. H. Daido *et al.*, Rep. Prog. Phys. **75**, 056401 (2012).
2. A. S. Pirozhkov *et al.*, Opt. Express **25**, 20486 (2017).
3. M. Nishiuchi *et al.*, Phys. Rev. Rep., **2**, 033081 (2020).
4. H. Kiriya *et al.*, Opt. Lett. **43**, 2595 (2018).
5. M. Nishiuchi *et al.*, Rev. Sci. Instrum. **91**, 093305 (2020).
6. Y. Sentoku *et al.*, J. Comput. Phys. **227**, 6846 (2008).

New algorithm using L1 regularization for measuring electron energy spectra

Hironao Sakaki



High-Intensity Laser Science Group, Department of Advanced Photon Research

Electron magnetic spectrometers are a commonly used diagnostic tool for measurement of the energy spectrum of electron beams. In our research, they are used to measure the electron energy spectrum produced during laser-driven particle acceleration. They are important tools to investigate the physics of the high intensity laser-matter interaction. We have published that the high-speed and high reliability of the tool was demonstrated by fusing the L1 regularization algorithm and electron magnetic spectrometers¹, and explain this method in this report.

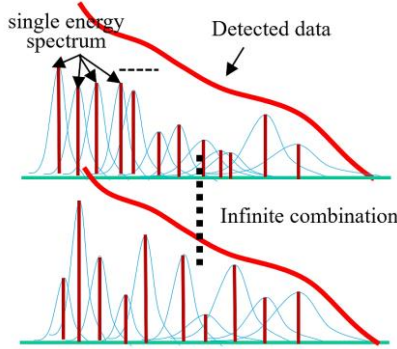


Fig. 1 An infinite number of combinations exists of light blue distributions that produce detection data (red line). The deconvolution process becomes an ill-posed problem and crosstalk complicates the separation of the individual sources.

Figure 1 is an approximate schematic of the measurement of detected electrons with a broadband energy distribution with an electron magnetic spectrometer. In the case of a single energy, one spectrum with the energy dispersion can be obtained; however, for a broadband energy distribution, the detected data (the red line) convoluted by the single distributions. Recovering the spectrum from the detected data from an electron spectrometer is a problem known in the signal processing field as source separation (SS), in which multiple sources (electrons of different energies) are mixed and combined in the measurement, resulting in an overlapping signal on the detector (crosstalk). Thus, the spectrum deconvolution process can become a mathematically ill-posed problem and crosstalk complicates the separation of the individual energy spectra. The current optimization method has a problem in that the solution cannot be uniquely determined in the SS problem, and in such a case, it is necessary to make an initial guess close to the solution so that the deconvolution process can lead to an optimal solution. The analysis of physics data requires objective analysis, and thus it is better that the initial value is chosen randomly. However, in general analysis, the initial value often includes the analyst's subjectivity. To improve measurement resolution, "sparse coding", a method of converting input data into a combination of bases and using L1 regularization to retain only the minimum number of bases required to reproduce the input, has recently become widespread². With appropriate consideration of the

hardware configuration, an optimal result can be reproduced even from poorly resolved signals. This idea gives a mathematical solution to the ill-posed problem, in assuming the mathematical condition of "sparse (minimal parameter)". By giving mathematical conditions to the solution, the retrieved spectrum allows removal of analyst subjectivity (Fig. 2).

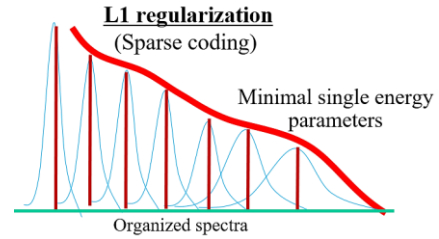


Fig. 2 Assuming a mathematical condition of "detected data is composed of minimal single energy spectra (minimal parameters)." Sparse coding organizes the spectrum into a simple discrete distribution.

Here, L1-constrained Huber loss minimization (L1CHLM), a type of L1 regularization algorithm, is used. The algorithm is as follows³:

1. Initialize parameter θ , e.g., randomly or by ordinary Least Squares, $\theta_1 \leftarrow \Phi^{\dagger}y$.
2. Compute the weight matrix \mathbf{W} and regularization matrix Θ from the current solution θ as $\mathbf{W} = \text{diag}(w_1, \dots, w_N)$ and $\Theta = \text{diag}(|\theta_1|, \dots, |\theta_b|)$, where the weight w_i is defined using residual $r_i = y_i - f_{\theta}(z_i)$ as $w_i = \begin{cases} 1 & (|r_i| \leq \eta), \\ \eta/|r_i| & (|r_i| > \eta). \end{cases}$
3. Compute the solution θ based on the weight matrix \mathbf{W} regularization matrix Θ as $\theta_{n+1} \leftarrow (\Phi^T \mathbf{W} \Phi + \lambda \Theta)^{-1} \Phi^T \mathbf{W} y$. Here, λ is the L1 regularization factor that optimized for the system, and n is the number of iterations.
4. The calculated θ_i is positively constrained with a ramp function with a small minimum cut off. $\theta_i = \max(10^{-10}, \theta_i)$.
5. Iterate 2 – 4 until $\|\theta_{n+1} - \theta_n\|$ converges.

As shown in Figure 2, the sparse coding algorithm produces a discrete distribution. This is a natural result of the L1 constraint, such that the spectrum is expressed by a minimum number of response functions for the spectrometer's detector. However, even if the retrieved spectrum is produced by sparse coding that is mathematically correct, it cannot accurately reproduce the real electron energy spectrum. Therefore, we reconsidered the physical meaning of this spectrum from the result of the sparse coding.

The solution consists of the N_{sp} distribution in which the degree of sparsity depends on the spectral width of the detector

response function Φ , giving a step size of dE_{sp} that the L1CHLM algorithm automatically selects, as shown in Fig. 3 (a). This is a physical interpretation that is given to the solution as a sparse spectrum is an integrated value of mixed electron energy distributions that are in the automatically optimized peak position interval of dE_{sp} . To determine the correct interpretation of the physical spectrum, we instead regard the automatically optimized peak position interval dE_{sp} as an optimized bin width of the spectrum, and N_{sp} is normalized with this bin width (Fig. 3 (b)). This procedure is referred to as "decoding", in contrast to sparse coding. By this decoding, an electron distribution with an optimized energy bin width is reproduced from the sparse coding result (Fig. 4(c) red line) that closely matches the original input spectrum (Fig. 4(c) pink dot-line).

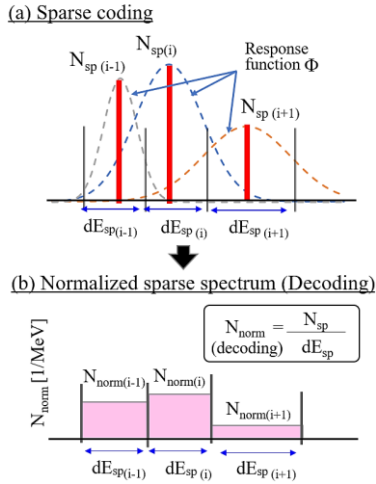


Fig. 3 (a) The concept of sparse coding. (b) Spectral normalization with optimized dE_{sp} . Here, this is termed as decoding.

The sparse decoding and a previous technique (stochastic gradient descent algorithm, SGDA) were compared to the geometry of the electron spectrometer using the beam transport simulation (PHITS code) with an electron temperature of $Te = 5.0$ MeV. SGDA needs an initial value for rapid convergence. Figure 4(a) shows the result of the optimization with various initial values of $Te = 1.0$ to 15.0 MeV.

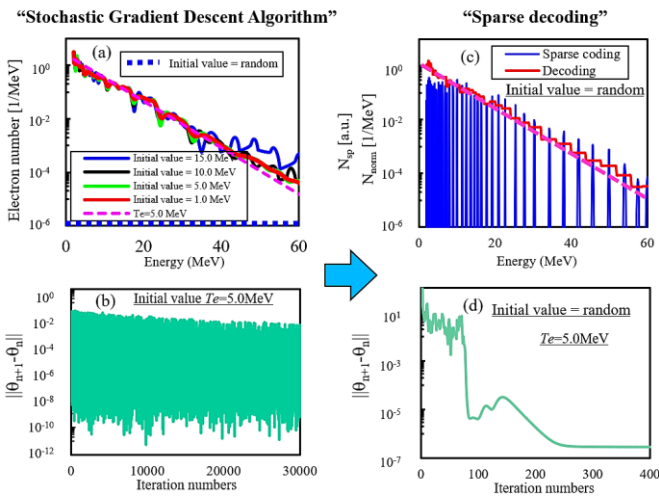


Fig. 4 (a) The result of the SGDA, assuming various initial values of Te from 1.0 to 15.0 MeV. (b) Convergence of the norm of the parameter with the SGDA when initial value is $Te = 5.0$ MeV. (c) The result of the sparse coding for a random initial value. (d) Convergence of the norm of the parameter with sparse coding for a random initial value.

The input was reproduced for initial values of 1.0 MeV and 15.0 MeV. In cases where the initial value was greater than 10.0 MeV, the high-energy part of the retrieved spectrum did not match the source spectrum (Fig. 4(a) pink dot-line). A correct spectrum cannot be obtained unless a value close to the correct spectrum is used as an initial value. If the initial value is chosen randomly, the norm of the parameter does not converge, even after more than 30000 iterations, and no solution can be obtained (Fig. 4(b)). Alternatively, the parameter changes during the algorithm iterations, showing a rapid convergence as the number of iterations increases (Fig. 4(d)). Compared to the SGDA, as the number of iterations increases, the norm of the parameter from the sparse coding converges rapidly in less than 300 iterations and reaches a stable value. This is two orders faster than the stochastic gradient descent. The sparse decoding results (Fig. 4(b) red line) also agree with the source spectrum (Fig. 4(b) pink dot-line) with an error of 4% or less, demonstrating the effectiveness of this method.

When used for actual measurements, algorithms often fail to perform well due to noise generated in the measurement system. Therefore, a verification was carried out by the J-KAREN-P laser system.

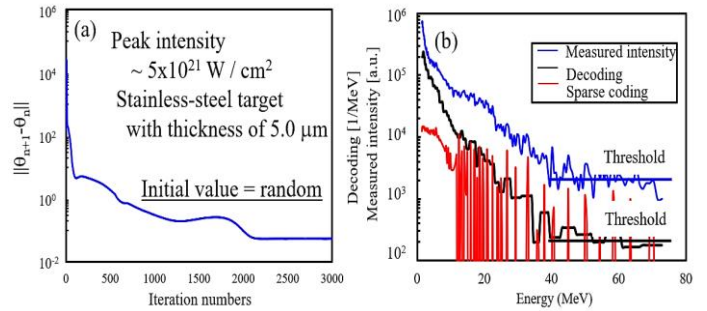


Fig. 5 (a) The convergence of the norm when sparse coding the measurement results. (b) Measured intensity of the detector (blue line), and after sparse coding (red line) and decoding (black line).

Figure 5(a) shows the convergence of the norm of the parameters during the sparse coding, demonstrating that the algorithm is not affected by noise. This algorithm uses a random initial value; however, the parameters converge after 2000 iterations on the measured data. Figure 5(b) shows the final spectrum after decoding (black line). The small peak at 20 MeV on the measured data is from crosstalk. The decoded signal shows decreasing crosstalk.

In conclusion, we have demonstrated a magnetic spectrometer for electron energy spectrum diagnosis, or the "source separation" problem, and performed an analysis via sparse techniques. This analysis concept of automatic bin width optimization obtained from sparse coding could be a novel spectrum diagnostic method for not only electron spectroscopy but also for other spectral measurements.

Acknowledgments

We would like to thank Professor Sugiyama, who is a director for RIKEN Center for Advanced Intelligence Project, for important comments on L1CHLM.

References

1. H. Sakaki, et al., Rev. Sci. Inst., 91, 075116 (2020).
2. David L. Donoho, IEEE TRANS. ON INFO. 52, 4 (2006).
3. M. Sugiyama, "Introduction to Statistical Machine Learning", Elsevier Inc, 279-293 (2015).

Vacuum Pair Creation via Ultrahigh Intensity Laser Induced Micro-Bubble Implosions

James K. Koga



High Intensity Laser Science Group, Department of Advanced Photon Research

The breakdown of air such as by lightning, engine spark plugs, or stove ignitors, occurs frequently in our daily lives. However, quantum electrodynamics (QED), which describes the interactions of electrons and photons, predicts that even in the absence of air (i.e., a vacuum), electrons and positrons can be still be produced if sufficiently large electric fields are generated [1-3]. These electric fields are predicted to be incredibly large. Whereas, for example, the typical electric field to breakdown air is 3×10^6 V/m [4] the QED vacuum breakdown voltage is predicted to be 1.32×10^{18} V/m [1-3]. This is nearly one trillion times larger!

Ultra-high intensity lasers made possible with the development of chirped pulse amplification (CPA) [5] are one means of achieving such electric fields. Currently, laser intensities of over 10^{22} W/cm² [6-9] or equivalent electric fields of over approximately 3×10^{14} V/m have been achieved. Although this is over 100 million times the air breakdown field, it is still lower than the QED breakdown field. Next generation lasers are expected to reach 10^{23} W/cm² (approximately 9×10^{14} V/m) or higher [10]; however, even these lasers will have electric fields far below the QED breakdown field. Other methods for pair creation from vacuums include focusing multiple colliding laser pulses (MCLPs) to lower the breakdown threshold [11-13] and colliding high-energy electron beams with MCLPs [14].

In this study, another method to achieve vacuum breakdown via micro-bubble implosions is considered [15]. In a micro-bubble implosion, a solid with a spherical empty cavity on the order of microns is irradiated by an ultra-intense laser to produce hot electrons [15]. Laser intensities on the order of 10^{21} - 10^{23} W/cm² produce electrons with temperatures ranging from 10-100 MeV [16], which fill the cavity, generating uniform electrostatic fields inside and outside the cavity that drive a spherically uniform implosion of the ions in the material [15,16] (see Fig. 1). The imploded core of ions can generate extremely large electric

fields that can approach the breakdown fields [16].

It was found that by choosing appropriate materials the breakdown field can be achieved using the properties of next generation laser systems [17]. The number of electron-positron pairs created from the vacuum from electromagnetic fields confined within a finite volume over finite time [2,3,18-20] was determined by varying the initial average electron density injected into the cavity from ultrahigh intensity lasers and the initial cavity radius. The typical parameters of a solid hydrogen target with a density of 5×10^{22} cm⁻³ was used with a cavity with a 2- μ m radius and an initial average injected electron density of 5×10^{21} cm⁻³ [15]. It was found that pair creation is easier to achieve by increasing the initial average electron density in the cavity [17]. This could be done by coating the target surface with a high-Z material such as plastic [16] or gold. This would allow pair production in a vacuum with approximately 200 to 300 petawatt lasers with energies of approximately 2 to 3 kJ [17]. In addition, even with electric fields below the breakdown field for pair production, externally injected electrons or photons of sufficiently high-energy pair production could be induced [17].

These possibilities make micro-bubble implosions an interesting subject for the study of electron-positron pair production in a vacuum.

Acknowledgments

The author thanks the collaborators this research, M. Murakami, A. V. Arefiev, Y. Nakamiya, S. S. Bulanov, and S. V. Bulanov for their contributions and efforts.

References

1. F. Sauter, Über das Verhalten eines Elektrons im homogenen elektrischen Feld nach der relativistischen Theorie Diracs, Z. Phys. 69 (11) (1931) 742-764.

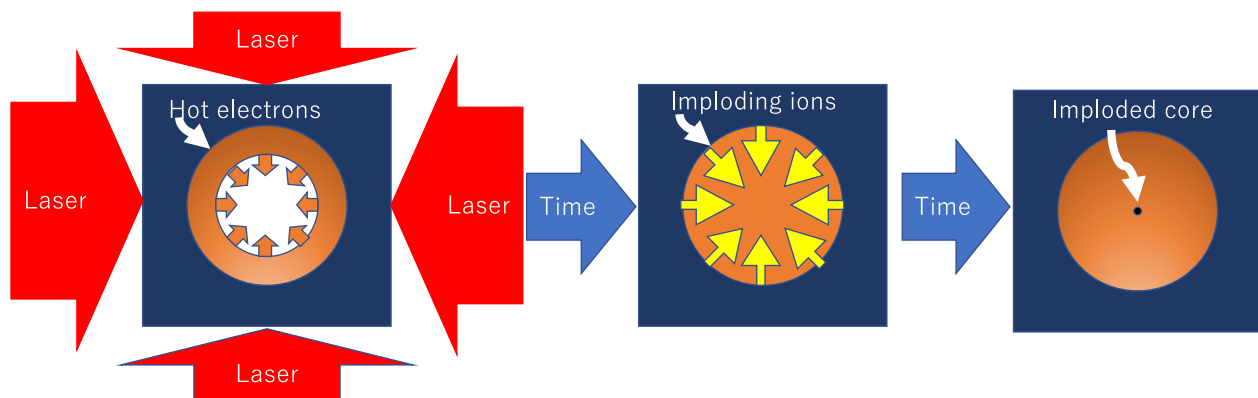


Fig. 1. Schematic of the micro-bubble implosion: (1) a hollow spherical cavity in a solid material (blue region) irradiated on the surface by ultra-high intensity lasers, thus producing hot electrons streaming from the surface (orange areas) into the cavity; (2) the cavity fills with these hot electrons, resulting in an electric field at the surface of the cavity walls (yellow arrows), which pulls the ions in the solid towards the center of the cavity; and (3) the ions converge at the center of the cavity to produce a ultrahigh density core (black circle) with a large electrostatic field.

2. W. Heisenberg, H. Euler, Folgerungen aus der Diracschen Theorie des Positrons, *Z. Phys.* 98 (11) (1936) 714-732.
3. J. Schwinger, On gauge invariance and vacuum polarization, *Phys. Rev.* 82 (1951) 664-679.
4. https://en.wikipedia.org/wiki/Electrical_breakdown
5. D. Strickland, G. Mourou, Compression of amplified chirped optical pulses, *Opt. Commun.* 55 (6) (1985) 447-449.
6. A.S. Pirozhkov, Y. Fukuda, M. Nishiuchi, H. Kiriyama, A. Sagisaka, K. Ogura, M. Mori, M. Kishimoto, H. Sakaki, N.P. Dover, K. Kondo, N. Nakanii, K. Huang, M. Kanasaki, K. Kondo, M. Kando, Approaching the diffraction-limited, bandwidth-limited Petawatt, *Opt. Express* 25 (17) (2017) 20486-20501.
7. H. Kiriyama, A.S. Pirozhkov, M. Nishiuchi, Y. Fukuda, K. Ogura, A. Sagisaka, Y. Miyasaka, M. Mori, H. Sakaki, N.P. Dover, K. Kondo, J.K. Koga, T.Z. Esirkepov, M. Kando, K. Kondo, High-contrast high-intensity repetitive petawatt laser, *Opt. Lett.* 43 (11) (2018) 2595-2598.
8. V. Yanovsky, V. Chvykov, G. Kalinchenko, P. Rousseau, T. Planchon, T. Matsuoka, A. Maksimchuk, J. Nees, G. Cheriaux, G. Mourou, K. Krushelnick, Ultra-high intensity-300-TW laser at 0.1 Hz repetition rate, *Opt. Express* 16 (3) (2008).
9. J.W. Yoon, C. Jeon, J. Shin, S.K. Lee, H.W. Lee, I.W. Choi, H.T. Kim, J.H. Sung, C.H. Nam, Achieving the laser intensity of 5.5×10^{22} W/cm² with a wavefront-corrected multi-PW laser, *Opt. Express* 27 (15) (2019) 20412-20420.
10. C.N. Danson, C. Haefner, J. Bromage, T. Butcher, J.-C.F. Chanteloup, E.A. Chowdhury, A. Galvanauskas, L.A. Gizzi, J. Hein, D.I. Hillier, et al., Petawatt and exawatt class lasers worldwide, *High Power Laser Sci. Eng.* 7 (2019) e54.
11. S.S. Bulanov, V.D. Mur, N.B. Narozhny, J. Nees, V.S. Popov, Multiple colliding electromagnetic pulses: a way to lower the threshold of e^+e^- pair production from vacuum, *Phys. Rev. Lett.* 104 (2010) 220404.
12. S.S. Bulanov, T.Z. Esirkepov, A.G.R. Thomas, J.K. Koga, S.V. Bulanov, Schwinger limit attainability with extreme power lasers, *Phys. Rev. Lett.* 105 (2010) 220407.
13. A. Gonoskov, I. Gonoskov, C. Harvey, A. Ilderton, A. Kim, M. Marklund, G. Mourou, A. Sergeev, Probing nonperturbative QED with optimally focused laser pulses, *Phys. Rev. Lett.* 111 (2013) 060404.
14. J. Magnusson, A. Gonoskov, M. Marklund, T.Z. Esirkepov, J.K. Koga, K. Kondo, M. Kando, S.V. Bulanov, G. Korn, C.G.R. Geddes, C.B. Schroeder, E. Esarey, S.S. Bulanov, Multiple colliding laser pulses as a basis for studying high-field high-energy physics, *Phys. Rev. A* 100 (2019) 063404.
15. M. Murakami, A. Arefiev, M.A. Zosa, Generation of ultrahigh field by micro-bubble implosion, *Sci. Rep.* 8 (1) (2018) 7537.
16. M. Murakami, A. Arefiev, M.A. Zosa, J.K. Koga, Y. Nakamiya, Relativistic proton emission from ultrahigh-energy-density nanosphere generated by microbubble implosion, *Phys. Plasmas* 26 (4) (2019) 043112.
17. J.K. Koga, M. Murakami, A.V. Arefiev, Y. Nakamiya, S.S. Bulanov, S.V. Bulanov, Electron-positron pair creation in the electric fields generated by micro-bubble implosions, *Physics Letters A*, Volume 384, Issue 34, 2020.
18. N.B. Narozhny, S.S. Bulanov, V.D. Mur, V.S. Popov, e^+e^- pair production by a focused laser pulse in vacuum, *Phys. Lett. A* 330 (1) (2004) 1-6.
19. N.B. Narozhny, S.S. Bulanov, V.D. Mur, V.S. Popov, On e^+e^- pair production by colliding electromagnetic pulses, *JETP Lett.* 80 (6) (2004) 382-385.
20. S.S. Bulanov, N.B. Narozhny, V.D. Mur, V.S. Popov, Electron-positron pair production by electromagnetic pulses, *J. Exp. Theor. Phys.* 102 (1) (2006) 9-23.

Investigation and improvement of pre-pulse generation by post-pulses in the J-KAREN laser system



Hiromitsu Kiriya

Advanced Laser Group, Department of Advanced Photon Research

With the continuous evolution of ultra-high peak power chirped-pulse amplification (CPA) laser technology [1], 1 PW to 10 PW power lasers and $10^{22}/\text{cm}^2$ or more focused intensities have become available [2]. Any pre-pulses with intensities of 10^{10} - 10^{11} W/cm² prior to the main pulse are capable of ionizing solid targets, which will then significantly influence the laser-plasma interaction process. Therefore, as an increasing number of facilities are providing highly focused intensities, the temporal contrast has become a major issue in all high-intensity laser-plasma experiments over the last two decades. Here, the investigation of the behavior of the pre-pulses generated by post-pulses at the J-KAREN-P laser facility is reported. Based on our experience and understanding of pre-pulse removal, we have achieved a high temporal contrast of 10^{12} and removed most of the pre-pulses.

It is essential to remove post-pulses to eliminate pre-pulses. Post-pulses do not directly affect the laser-plasma interaction process and can be ignored. However, in a CPA system, the duration of the stretched pulse is longer as compared with the time difference between the main and post-pulses, and these pulses overlap in time and interfere with each other. The frequency chirp and the delay between these pulses results in spectral interference. This sinusoidal spectral modulation can change the optical properties of the optical elements in the laser chain. The time-dependent optical properties can then modulate the spectral phase due to the intensity dependence of the B-integral (defined as the measure of the nonlinear phase shift of light) accumulated in the optical elements. The compressor converts this modulation by the post-pulse to a new pre-pulse [3-7]. These pre-pulses with relatively high intensities must be eliminated in order to avoid unwanted plasma formation or significant modification of the experimental target conditions before the arrival of the main pulse. Thus, it is important to investigate and remove the pre-pulses generated by post pulses, along with the accumulated B-integral values in the laser chain.

The creation of the real pre-pulses from post-pulses generated by internal reflections in the optical components in the laser chain was experimentally investigated through the nonlinear processes associated with the B-integral. The experiments were performed at the petawatt laser facility J-KAREN-P [8,9]. The laser pulses were stretched to approximately 0.5 ns and compressed down to approximately 40 fs. To generate the post-pulses, 1- and 11.8-mm thick, uncoated, plane-parallel plates made of fused silica were inserted into the laser beam perpendicular to its axis and placed before the Ti:sapphire pre-amplifier. The typical reflectivity was 3.4% per surface of the plane-parallel plates to generate post-pulses by internal reflections. As the stretched pulse duration was longer than the time difference between the main and post-pulses, the post-pulse generated by a 1-mm thick plane-parallel plate and main pulse overlapped in time considerably, while in contrast, the post-pulse generated by a 11.8-mm thick plate and main pulse only partially overlapped.

Figure 1 shows the temporal contrast of the pre-pulses from the post-pulses generated with the plane-parallel plates with thicknesses of 1 mm (Figure 1(a)) and 11.8 mm (Figure 1 (b)). The measurements were performed with output energies at the exit of the operating amplifiers of 1.8 and 26 J, resulting in different values for the B-integral of the pulses accumulated in the laser chain due to the different pulse intensities. The intensities of the beam before and after the compressor with the output energies at the exit of the operating amplifiers of 1.8 and 26 J were reasonably attenuated to $18 \text{ MW}/\text{cm}^2$ and $0.1 \text{ TW}/\text{cm}^2$, respectively. For the plane 1-mm thick parallel plate, the theoretical estimate fits the experimental data reasonably well [2]. The magnitude of the real pre-pulse peak contrast rises monotonically with the increasing B-integral. For the pre-pulses from the 11.8-mm thick plane-parallel plate, three interesting features are observed. First, the exact positions of the real pre-pulses in time do not coincide with the post-pulse at 118 ps after main pulse. The real pre-pulse peak is delayed by 4.8 to 113.2 ps. Second, the real pre-pulses are significantly asymmetrically distorted and broadened. Third, the real pre-pulse peak contrast is significantly suppressed. Although the real pre-pulse contrast for the 1-mm thick plate degraded to 6.8×10^{-4} , the degradation for the 11.8-mm thick plate only reached 3.8×10^{-6} . The real pre-pulse peak contrast measured with the 11.8-mm thick plate is much lower as compared with the theoretical prediction, by approximately two orders of magnitude [2]. The magnitude of the real pre-pulse peak contrast is degraded and the pulse duration of the delayed real pre-pulse is broadened with the increased B-integral values. The degradation of the real pre-pulse peak contrast for the 11.8-mm thick plate is much smaller than that for the 1-mm thick plate.

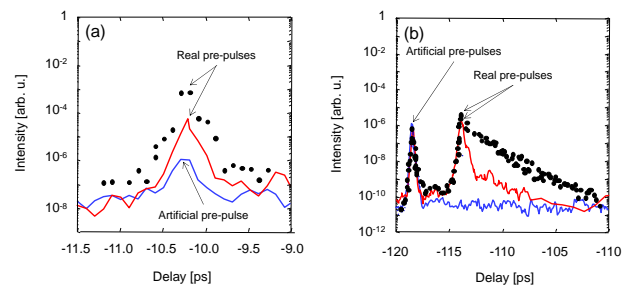


Figure 1. Pre-pulse contrast in the J-KAREN-P laser system with plane-parallel plates with thicknesses of (a) 1 mm and (b) 11.8 mm. The blue lines are for calibration (the plane-parallel plate was placed after the compressor). The red lines and black filled circles were obtained at output energies of 1.8 and 26 J, respectively. These energies correspond to B-integrals of 0.25 and 0.85 rad, respectively.

The experiment with the 1-mm thick plane-parallel plate confirms that the real pre-pulse generation is due to the nonlinearity of the refractive index and the real pre-pulse peak

contrast agrees reasonably well with the theoretical prediction [2]. However, in the experiment with the 11.8-mm thick plane-parallel plate, the real pre-pulses were delayed and asymmetrically broadened. This mechanism is not yet understood. Although the post-pulses generated by the 1-mm thick plane-parallel plate almost fully overlap with the main pulse before recompression (by 98%), the post-pulses generated by the 11.8-mm thick plane-parallel plate only overlap partially (by 75%). The smaller overlap percentage indicates a smaller interference, resulting in a narrower spectral bandwidth modulation and, due to its nonlinear nature, smaller energy transfer to generate real pre-pulses. Therefore, the real generated pre-pulses have a broader pulse duration and lower peak intensity. The dispersion of these real pre-pulses accumulated in the laser chain with many optics differs widely from that of the main pulse. Thus, these real pre-pulses are not allowed to compress to the same pulse duration as the main pulse since the compressor is set and optimized for the main pulse dispersion. The asymmetrically distorted, real pre-pulse shape, i.e., the significantly extended tail starting from the pre-pulse peak indicative of positive, higher odd-order dispersion, is also likely to be combined with self-phase modulation. The modulated portion had shorter wavelength components, which are later in time in the present positive, chirped-laser system. Therefore, the real generated pre-pulses are delayed in time. In order to fully understand and evaluate the real pre-pulses generated by post-pulses through the nonlinear process, additional and further research, both theoretical and experimental, is required and will be reported in future works.

Figure 2 (a) shows the measured contrast of the J-KAREN-P laser system with output pulse energies of approximately 1 and 10 J. According to the above results, we have identified real and artificial pre-pulses generated by the post-pulses. In order to remove the post-pulses from the Ti:sapphire crystals windows and Faraday isolator, new crystals and windows with a small wedge were introduced, and the Faraday isolator was removed as the current laser system has sufficient isolation. In order to suppress the pre-pulse generated by the post-pulse from the oscillator, we are preparing to install a plasma mirror system. The pre-pulses except for a pre-pulse at -40 ps have been removed, as shown in Figure 2 (b).

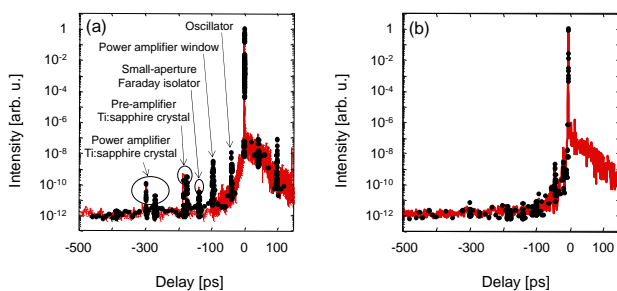


Figure 2. (a) Previous and (b) current temporal contrast of the J-KAREN-P laser system with output energies of approximately 1 (solid red line) and 10 J (black filled circles).

Pre-pulse generation by post-pulses due to the nonlinear coupling associated with the B-integral was experimentally investigated at the J-KAREN-P PW facility. According to the knowledge and experience obtained from this investigation, the origins of the pre-pulses generated through nonlinear coupling by the post-pulse have been identified. By introducing small-wedged optics, the pre-pulses at the J-KAREN-P PW facility were eliminated.

Acknowledgments

The author thanks Yasuhiro Miyasaka, Akito Sagisaka, Koichi Ogura, Mamiko Nishiuchi, Akira Kon, Alexander S. Pirozhkov, Yuji Fukuda, Nicholas P. Dover, Kotaro Kondo, James K. Koga, Masaki Kando, Kiminori Kondo, Stefan Bock, Tim Ziegler, Tomas Püschel, Karl Zeil, and Ulrich Schramm. This research was funded by the Japan Society for the Promotion of Science (grant number: JP 20H01882).

References

1. D. Strickland and G. Mourou, "Compression of amplified chirped optical pulses," *Opt. Commun.* **56**, 219–221 (1985).
2. C. N. Danson, C. Haefner, J. Bromage, T. Butcher, J.-C. F. Chanteloup, E. A. Chowdhury, A. Galvanauskas, L.A. Gizzi, J. Hein, D. I. Hillier et al., "Petawatt and exawatt class lasers worldwide," *High Power Laser Sci. Eng.* **7**, e54 (2019).
3. N. V. Didenko, A. V. Konyashchenko, A. P. Lutsenko, S. Y. Tenyakov, "Contrast degradation in a chirped-pulse amplifier due to generation of prepulses by postpulses," *Opt. Express* **16**, 3178–3190 (2008).
4. D. N. Schimpf, E. Seise, J. Limpert, A. Tünnermann, "Decrease of pulse-contrast in nonlinear chirped-pulse amplification systems due to high-frequency spectral phase ripples," *Opt. Express* **16**, 8876–8886 (2008).
5. S. Keppler, M. Hornung, R. Bodefeld, M. Kahle, J. Hein, M. C. Kaluza, "All-reflective, highly accurate polarization rotator for high-power short-pulse laser systems," *Opt. Express* **20**, 20742–20747 (2018).
6. V. A. Schanz, C. Brabetz, D. J. Posor, D. Reemts, M. Roth, V. Bagnoud, "High dynamic range, large temporal domain laser pulse measurement," *Appl. Phys. B* **125**, 61 (2019).
7. H. Kiriya, Y. Miyasaka, A. Sagisaka, K. Ogura, M. Nishiuchi, A. S. Pirozhkov, Y. Fukuda, M. Kando, K. Kondo, "Experimental investigation on the temporal contrast of pre-pulses by post-pulses in a petawatt laser facility," *Opt. Lett.* **45**, 1100–1103 (2020).
8. H. Kiriya, A. S. Pirozhkov, M. Nishiuchi, Y. Fukuda, K. Ogura, A. Sagisaka, Y. Miyasaka, M. Mori, H. Sakaki, N. P. Dover et al., "High-contrast high-intensity repetitive petawatt laser," *Opt. Lett.* **43**, 2595–2598 (2018).
9. H. Kiriya, A. S. Pirozhkov, M. Nishiuchi, Y. Fukuda, K. Ogura, A. Sagisaka, Y. Miyasaka, H. Sakaki, N. P. Dover, K. Kondo et al., "Status and progress of the J-KAREN-P high intensity laser system at QST," *High Energy Density Phys.* **36**, 100771 (2020).

Capturing roaming fragments in the dissociation of formaldehyde in real-time

Tomoyuki Endo

Ultrafast Dynamics Group, Department of Advanced Photon Research



In conventional chemical reactions, molecules follow the minimum energy paths from reactants to products. However, the molecules sometimes take a little extra “walk”.

Two possible pathways for the dissociation of formaldehyde molecules (H_2CO) are considered: the dissociation to $\text{H}_2 + \text{CO}$ (molecular dissociation channel), and the dissociation to $\text{H} + \text{HCO}$ (radical dissociation channel). In alternative “roaming” dissociation pathways, the roaming fragment (H atom) walks around the remaining parent molecule (HCO, see Fig. 1). Since the first observation of “roaming” in the dissociation reaction of H_2CO in 2004 [1], footprints of roaming reactions have been reported in a wide variety of molecular systems. The outcomes of roaming processes have been observed using high-resolution spectroscopy to determine the product state distributions in almost all experimental roaming studies. In the case of H_2CO , the roaming outcomes show a characteristic combination of hot H_2 vibrational- and cold CO rotational-level populations, which is distinct from the populations in conventional molecular and radical dissociation channels.

Previous time-resolved experiments have focused on the time-resolved measurement of roaming outcomes rather than a roaming fragment itself [2-5]. One reason is that both the onset and duration of roaming are strongly stochastic. For H_2CO , roaming occurs on the vibrationally hot electronic ground S_0 state. Even though the roaming process itself occurs at the femtosecond time scale, the overall time scales (excitation, relaxation, vibration and roaming on the hot S_0 state, and dissociation) span hundreds of femtoseconds to tens of nanoseconds.

Recently, a roaming fragment itself has been captured in real-time by a combination of Coulomb explosion imaging and quasi-classical trajectory analysis [6]. Here a comprehensive

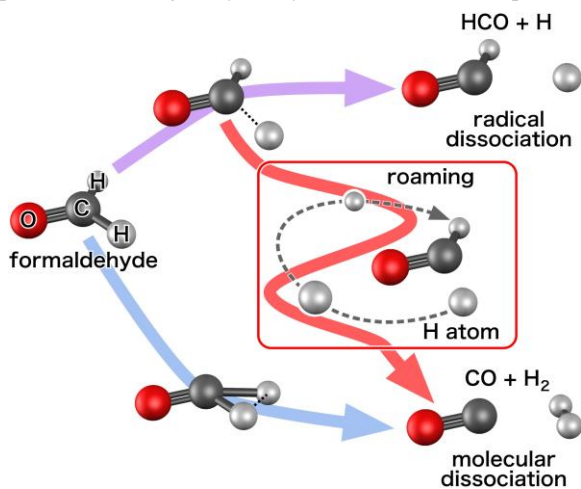


Fig. 1. Scheme representing the three dissociation pathways of a formaldehyde molecule (H_2CO): conventional molecular (blue arrow at the bottom) and radical (purple arrow at the top) dissociation, and roaming (red arrow in the middle).

picture is presented; the ultrafast dynamics triggered in neutral formaldehyde molecules upon femtosecond ultraviolet (UV) photoexcitation.

The Coulomb explosion imaging experiment was performed at the Advanced Laser Light Source (INRS-ÉMT, Canada) on the multi-kHz beamline. UV pump pulses were obtained by frequency quadrupling of the output of an optical parametric amplifier. Time-delayed probe pulses were obtained by pulse compression with a pressure-gradient hollow-core fiber and chirped mirrors. Both the pump and probe laser pulses were focused on an effusive molecular beam of deuterated formaldehyde (D_2CO). The ions generated by the probe pulses were collected with a uniform-electric-field ion imaging spectrometer. The three-dimensional momentum of each fragment ion was retrieved using a time- and position-sensitive delay-line detector. The total kinetic energy release (KER) E_{kin} and the angle θ between two deuteron momentum vectors can be expressed as

$$E_{\text{kin}} = \sum_i^n \frac{|\mathbf{p}_i|^2}{2m_i},$$

and

$$\theta = \cos^{-1} \left(\frac{\mathbf{p}_1 \cdot \mathbf{p}_2}{|\mathbf{p}_1| |\mathbf{p}_2|} \right),$$

where \mathbf{p}_i and m_i are the momentum and the mass of the i -th fragment, and $i = 1, 2$, corresponding to the two deuterons, respectively. The relationship between the molecular geometry before the Coulomb explosion and the distributions of the resulting E_{kin} and θ is as follows: a large E_{kin} and a θ of approximately 120 degrees is the equilibrium geometry (orange circle in Fig. 2), a small E_{kin} and broad θ distribution due to weak interactions between deuterons is the radical dissociation channel (purple), an intermediate E_{kin} and a θ of approximately 180 degrees due to strong Coulomb repulsion between deuterons is the molecular dissociation channel (light-blue), and an intermediate E_{kin} and limited θ distribution is the roaming pathway (red).

The obtained two-dimensional plots of E_{kin} with θ for the three-body breaking ($\text{D}^+, \text{D}^+, \text{CO}^+$) channel of D_2CO^{3+} at the pump-probe time delays Δt between 0 fs and 5 ps are shown in Fig. 2. In the KER region < 12 eV, the onset of molecular dynamics occurred already before 100 fs. Although the relaxation from the electronically excited S_1 state to the hot S_0 state was previously predicted to occur in tens of nanoseconds, the present result indicates that the dissociation occurs at the femtosecond timescale due to strong coupling between vibrational states during irradiation of femtosecond UV pump pulses. The existence of the fast relaxation process was verified by photoelectron experiments at Nagoya University and *ab initio* calculation. The angular distribution in the KER range < 5 eV is broader than in the 5-12 eV range. The broader angular distribution below 5 eV reflects that one deuteron moves freely around the parent molecule, showing the contribution of the radical dissociation channel in this range. Both the intermediate

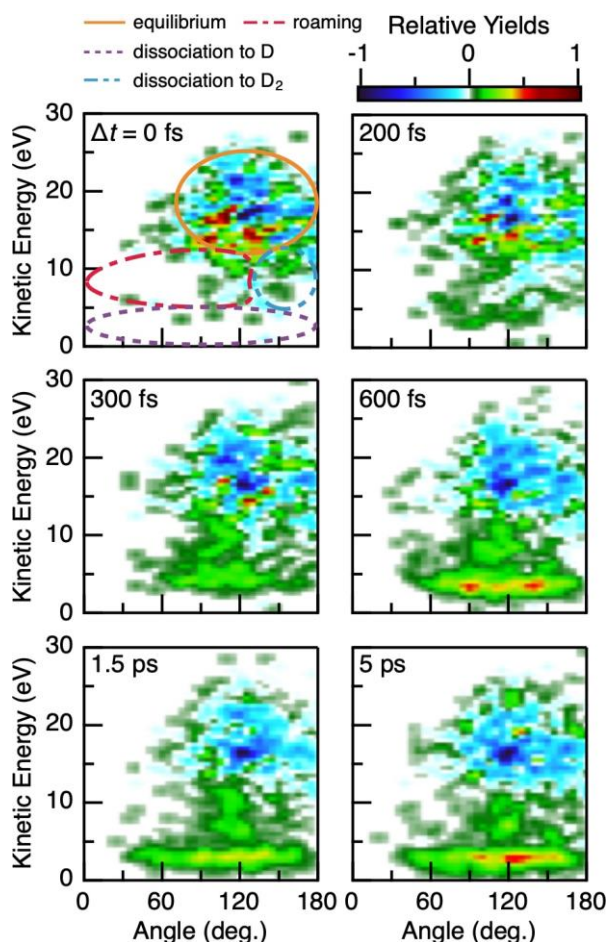


Fig. 2. Two-dimensional plots of kinetic energy versus deuteron momentum angle at the pump-probe time-delay Δt . The distribution at $\Delta t = -300$ fs was subtracted as background. Indicated in the upper left subplot are the areas corresponding to each reaction pathway identified by using *ab initio* calculations (Fig. 3).

energy distribution and limited angular distribution in the 5-12 eV range show the characteristics of the roaming pathway.

To identify the contribution of the roaming process, a simulation using *ab initio* calculations including all the critical steps (relaxation, dynamics on the S_0 state, and Coulomb explosion) was performed. The molecular geometry for each trajectory and the corresponding two-dimensional plots of the simulated KER versus deuteron momentum angle are shown in Fig. 3. The left column contains the real-space representation of two deuterons with respect to the CO fragment (fixed at the origin) before the Coulomb explosion step. One deuteron is plotted on the x -axis and the other is on the xy -plane. The right panels show the simulated results with an *ab initio* potential energy surface of the triply charged state. Here, our generalized definition of roaming, where one of the deuterons exceeds the threshold distance ($R_{D-DCO} = 2.8$ Å) and then returns to the parent DCO molecule, was used to extract the corresponding geometry for the roaming pathway (Fig. 3B). In the molecular dissociation channel, both deuterons are far from CO (Fig. 3C). In the radical dissociation channel, one of the deuterons is close to CO and the other is far away (Fig. 3D). The remaining case, where both deuterons are close to CO, is the equilibrium geometry (Fig. 3E). The roaming trajectory is distinguishable from other molecular and radical dissociation pathways because of the characteristic distribution of the KER ranging from 10 to 16 eV and the angle between 90 and 140 degrees.

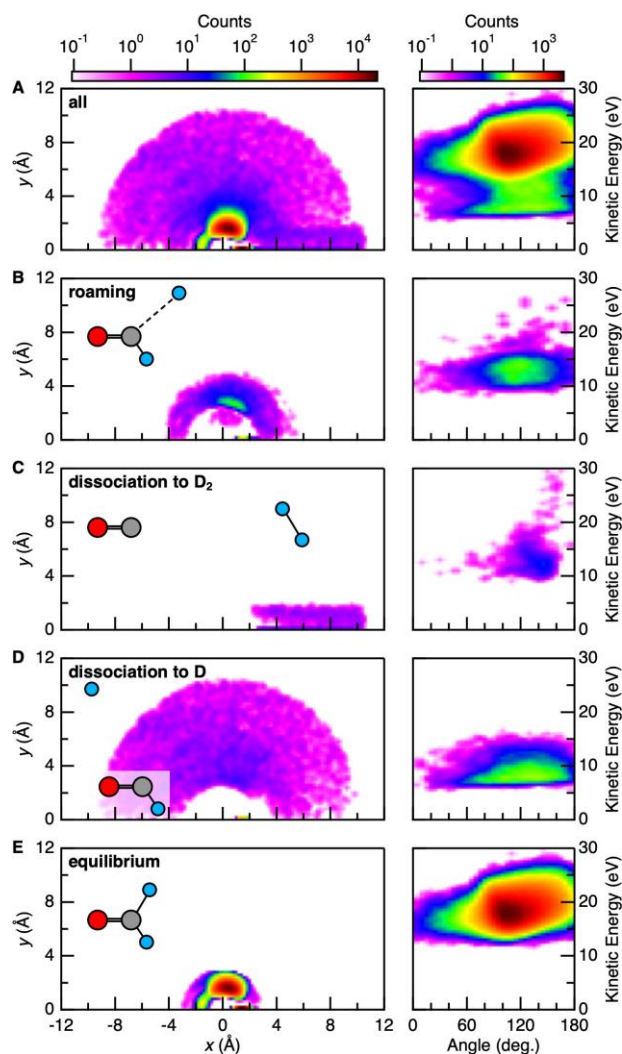


Fig. 3. (Left) The real-space representation of the molecular geometry for each reaction pathway before the Coulomb explosion. Typical geometries are represented on a relative scale. (Right) Two-dimensional plots of the simulated kinetic energy versus deuteron momentum angle.

The present results provide a new method for detecting weak statistical dynamics hidden in overwhelming background and could be extended to a vast variety of molecular systems.

Acknowledgments

The author thanks the collaborators in Japan, Canada, and the USA for their experimental and theoretical contributions, and especially Dr. H. Ibrahim for directing the project. This work was supported by the following funding sources: Canada Foundation for Innovation, NSERC, FRQNT, JSPS Program for Advancing Strategic International Networks to Accelerate the Circulation of Talented Researchers (grant no. S2601), World Research Unit (B-1) of Reaction Infography (R-ing) at Nagoya University, NSERC-Vanier fellowship program, and NASA (grant no. 80NSSC20K0360).

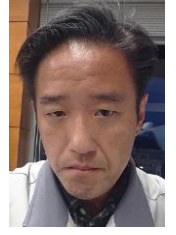
References

1. D. Townsend et al., *Science* **306**, 1158 (2004).
2. A. S. Mereshchenko et al., *Nat. Chem.* **7**, 562 (2015).
3. N. Ekanayake et al., *Sci. Rep.* **7**, 4703 (2017).
4. N. Ekanayake et al., *Nat. Chem.* **9**, 5186 (2018).
5. E. Livshits et al., *Commun. Chem.* **3**, 49 (2020).
6. T. Endo et al., *Science* **370**, 1072 (2020).

Relativistic Doppler reflection of terahertz light from a moving plasma front in an optically pumped Si wafer

Masaaki Tsubouchi

Ultrafast Dynamics Group, Department of Advanced Photon Research



Relativistic Doppler reflection is an interesting phenomena introduced by special relativity. When light is reflected by a counter-propagating mirror with a velocity close to the speed of light, a frequency up-shift of the light due to the relativistic Doppler reflection is induced as

$$v_r = v_i \Gamma = v_i (1 + \beta) / (1 - \beta), \quad (1)$$

where v_r and v_i are the frequencies of the reflected and incident light, respectively, Γ is the frequency up-shift factor, and $\beta = v_p / v_L$ is the ratio of the velocities of the moving mirror (v_p) and the incident light (v_L) in the medium. A moving plasma mirror has been previously proposed and used to demonstrate relativistic Doppler reflection at the Kansai Photon Science Institute (KPSI).¹ Overdense plasma with a high carrier density can act as a mirror for the light. When the near-infrared (NIR) ultra-intense laser is focused on the plasma, the free electrons in the plasma are accelerated to a velocity close to the speed of light by laser-plasma interaction. As a result, a relativistic moving plasma mirror is generated. Alternatively, Roskos and their colleagues have suggested the occurrence of Doppler reflection with a moving plasma front in a semiconductor excited by a femtosecond laser pulse.² A dense plasma layer consisting of free electrons in a conduction band is easily generated by optical pumping with NIR to visible light. In this case, the photo-excited electrons in the semiconductor do not receive a large momentum from the laser field. However, free electrons are successively generated while the optical pump pulse propagates into the semiconductor; subsequently, the ionization front copropagates with the optical pump pulse. Therefore, the moving ionization front can act as a relativistic moving plasma mirror.

The relativistic Doppler reflection of terahertz (THz) light in photo-excited silicon (Si) wafers has been investigated in our previous studies.³ The THz light oscillates at a low frequency (approximately 10^{12} Hz) as compared to an optical light and therefore, it can be reflected by a plasma with a relatively low carrier density (approximately 10^{17} cm⁻³). Furthermore, the THz light penetrates the Si wafer without significant absorption and dispersion. Thus, THz light is a suitable probe for relativistic Doppler reflection in Si. Time-resolved THz time-domain spectroscopy (THz-TDS) has been employed to reveal the Doppler reflection mechanism in Si. In THz-TDS, a waveform of the THz light pulse is measured in the time-domain and a complex THz spectrum is obtained by a Fourier transform of the waveform. This provides a significant advantage for understanding the interaction between a moving plasma front and THz light. The THz waveforms and spectra measured as a function of the delay time between the optical pump and THz probe light clearly demonstrated that the evolution of the moving plasma front with time induced the frequency up-shift of the reflected THz light. However, in our previous study, the measured frequency up-shift was considerably smaller than that predicted by Eq. (1). One possible reason for this is an insufficient bandwidth in the THz-TDS to measure a large frequency up-shift.

In the present study, the frequency up-shift in the relativistic Doppler reflection is re-examined by extending the spectral

bandwidth in the THz-TDS measurement. The broad bandwidth allows for accurate measurements of the large frequency up-shift to evaluate quantitatively the mechanism for the relativistic Doppler reflection. The high temporal resolution of the THz waveform is also provided by the broadband measurement. The improvement in the measurement allows a highly accurate analysis of the phase and the intensity spectra. The phase shift induced by the Doppler reflection includes detailed information on the moving plasma front. It is demonstrated that the Doppler reflection in the photo-excited Si realizes the spectral broadening and the pulse compression of the THz light, which provides a technique for the manipulation of the THz light.

Figure 1 shows a schematic diagram of the counter-propagation geometry of the moving plasma front and the THz pulse in Si.^{3,4} (1) First, the surface of a Si wafer is irradiated with a THz pulse that propagates through the Si. (2) When the THz pulse arrives at the rear surface, the pulse splits into two parts: the transmission to the air (Pulse A) and the internal reflection (Pulse B). (3) Prior to the arrival of the reflected THz Pulse B at the input surface, the optical pump light is shone on the Si wafer to generate a plasma layer. (4) The THz Pulse B is affected by the plasma near the input surface and is then subsequently reflected. The THz Pulse B then counter-propagates with respect to the pump light in the Si; subsequently, the plasma front approaches the THz light with a velocity close to that of the pump light. This induces relativistic Doppler reflection and causes a frequency up-shift for the THz light. In this scheme, the THz and optical light are input collinearly to the front surface of the Si, and the reflected THz pulse is taken from the rear surface. The two pulses (Pulse A and B) from the rear surface are separable by their arrival times at the detector. Thus, the THz pulse reflected by the moving plasma front is easily measured using this scheme.

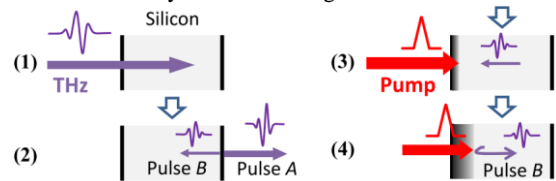


Fig. 1. (a) Diagram of the relativistic Doppler reflection. The time sequence of the THz probe and optical pump pulses and their propagation in the Si wafer are shown from (1) to (4).

The experimental apparatus is based on the optical pump-THz probe time-resolved measurement with THz-TDS as shown in [5]. Ti:Sapphire regenerative and multi-pass amplifiers were employed to generate pulses for THz light generation, THz pulse detection, and optical pumping of the Si wafer to generate the plasma layer. The THz pulse was generated by optical rectification in a LiNbO₃ prism with pulse front control. The optical pump and THz probe light collinearly propagated into a 1-mm thick high-resistivity (2 kΩcm) Si wafer. The waveform of the transmitted THz pulse from the Si was measured by electro-optic (EO) sampling. The bandwidth of the THz-TDS

measurement was limited by the pulse width of the EO sampling light and the absorption of the THz light in the birefringent EO crystal. The pulse width of the EO sampling light (50 fs) was sufficiently short to measure the frequency up-shift to 10 THz. In the previous study, a 1-mm thick ZnTe crystal was used for the EO sampling.³ However, due to the strong phonon absorption, the bandwidth was limited to under 2.5 THz. In the present study, to obtain the broadband measurements, including those in the higher frequency range, a 0.4-mm thick GaP crystal was employed whose edge of the phonon absorption band was approximately 5 THz.

Figure 2(a) shows the THz waveforms transmitted through the Si wafer as a function of the pump-probe delay time. Only Pulse B is displayed in the figure. ZnTe (thin black lines) and GaP (thick red lines) crystals were used for EO sampling. The energy density of the optical pump pulse penetrating into the Si wafer was $3.3 \mu\text{J}/\text{mm}^2$. When the THz pulse arrives at the front surface prior to the pump pulse ($\Delta t \ll 0$), the THz Pulse B has just completed a round trip between the back and front surfaces in the Si wafer after separating from Pulse A and reaching the detector. At $\Delta t = -2$ ps, the waveforms measured by the GaP crystal are identical to those from the ZnTe crystal. When the pump pulse excites the front surface no later than the THz reflection, the waveform of the reflected THz pulse changes. Around $\Delta t = 0$, when the THz light interacts with the moving plasma front near the input surface, Doppler reflection is expected. The results using the GaP crystal clearly reveal the pulse compression of the THz light pulse due to the Doppler reflection, indicating the frequency up-shift in the spectrum. By contrast, the ZnTe crystal cannot monitor the Doppler reflection accurately due to the lack in its time resolution. At a delay time of 2 ps, the reflected THz waveform phase changes by π , with a temporal advance of 0.67 ps as shown by the thick arrow in Figure 2(a). This is clear evidence of the reflection from the static plasma front in the Si close to the input surface.

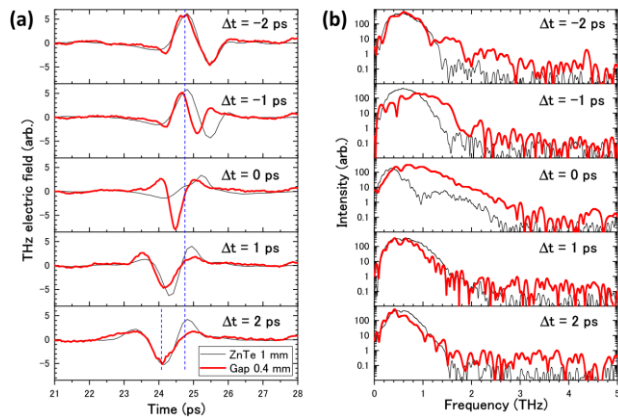


Fig. 2. (a) Waveforms and (b) Fourier transformed spectra of the reflected THz light as a function of the pump-probe delay Δt . The thin black and thick red lines show the results measured by the 1-mm thick ZnTe and 0.4-mm thick GaP EO crystals, respectively.

Figure 2(b) shows the time-dependent intensity spectra obtained by the Fourier transform of the THz waveforms shown in Figure 2(a). Before and after the pump light irradiation, the up-shift is not observed in the spectra since the reflection planes for the THz pulse are the static Si-air interface and the static plasma front, respectively. In contrast, the frequency up-shift induced by the relativistic Doppler reflection is clearly observed around $\Delta t = 0$ when the plasma front is moving. Due to the larger bandwidth, the larger frequency up-shift can be obtained (approximately 3 THz) by the GaP crystal rather than by the ZnTe crystal.

The THz-TDS provides not only the intensity, but also the

phase spectra. Therefore, the phase shift, which is the difference between the phases of the reflected THz light with and without the irradiation of the optical pump pulse, is easily obtained. The improvement in the time resolution in the THz-TDS measurement enables the accurate analysis of the spectral phase. Figure 3 shows the phase shift spectra of the reflected THz light as a function of the pump-probe delay time. At the negative delay time, the THz light is reflected at the air-Si boundary without influence from the optical pump light and no phase shift was observed. At $\Delta t = 0$, the THz light interacted with the moving plasma front close to the surface and a π phase jump of approximately 0.7 THz was found, which is one of the signatures of Doppler reflection. After the pump light is completely absorbed by the Si and the static plasma layer generated ($\Delta t > 0$), the phase shift monotonically decreases as the frequency increases. The observed phase shifts are compared to the one-dimensional finite-difference time-domain (1D-FDTD) simulation in Figure 3. The Fresnel reflection at the negative delays and the static plasma reflections at the positive delays are well reproduced by the 1D-FDTD simulation. However, the 1D-FDTD simulation poorly reproduces the observed result during the Doppler reflection around $\Delta t = 0$. One reason for this is that the simple Drude model adopted in the 1D-FDTD simulation is not suitable for describing the interaction of the instantaneously generated dense plasma with the THz light.

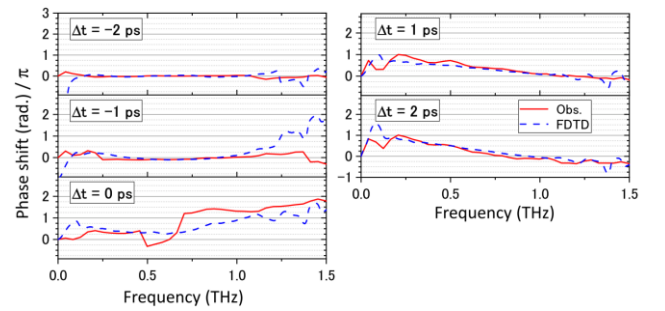


Fig. 3. Phase shift spectra of the reflected THz light as a function of the pump-probe delay time Δt . The solid red and blue dashed lines show the observed and calculated spectra, respectively.

Relativistic Doppler reflection has a potential application in pulse compression and spectral broadening of THz light for THz-TDS. Solid materials with optical functions (e.g., semiconductors and perovskite) have been investigated by optical-pump THz-probe time-resolved spectroscopy to reveal free-carrier and exciton dynamics in optically excited states. The frequency up-shift investigated in this study was realized by the conventional THz generation scheme and easily coupled with the optical-pump THz-probe experiment. The up-shift will be applied to reveal the phonon and exciton dynamics in optically excited materials.

Acknowledgments

I would like to thank Dr. Nanase Kohno who mainly performed the experimental work with a detailed analysis. I am grateful for the financial support from the Grants-in-Aid (No. 21850030 and 22750022) from the Ministry of Education, Science, Culture, and Sports (MEXT) of Japan.

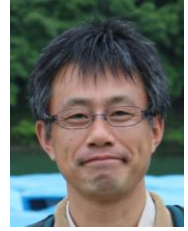
References

1. S. V. Bulanov et al., Phys. Rev. Lett. **91**, 085001 (2003).
2. M. D. Thomson et al., Phys. Rev. B **87**, 085203 (2013).
3. N. Kohno et al., Phys. Rev. B **94** (2016).
4. M. Tsubouchi et al., Opt. Lett. **37**, 3528-3530 (2012).
5. N. Kohno et al., Phys. Rev. B **102**, 235201 (2020).

Soft x-ray laser beamline for surface processing and damage studies

Masahiko Ishino

X-ray Laser Group, Department of Advanced Photon Research



Advances in physical studies and high-power laser technologies have enabled the realization of laboratory-size laser-driven plasma-based soft x-ray lasers (SXRLs). An SXRL system in the x-ray laser facility of the QST was developed [1], and gain saturations in the Ni-like Ag ($\lambda = 13.9$ nm) laser were demonstrated [2]. The SXRL system has been improved upon requests from experimental users. To increase the spatial coherence, the system adopted the oscillator-amplifier configuration [3]. To increase the repetition rate, a new driver laser system, which is a chirped-pulse amplification laser with a zigzag slab Nd:glass amplifier [4], and a new tape target system [5] were developed. This system enables the use of the SXRL with a 0.1 Hz scheme. An effort to increase the output energy of the SXRL was also performed [6]. The SXRL specifications are as follows [7]: an Ni-like Ag laser with a wavelength of $\lambda = 13.9$ nm (13.889 nm) [8], a spectral width of $\lambda/\Delta\lambda > 10^4$, a pulse duration τ of approximately 7 ps [9], a beam divergence of 0.3–0.35 mrad, and an average output energy of approximately 200 nJ/pulse.

In the wavelength region around 13 nm, the Mo/Si multilayers are available as high-efficiency soft x-ray optics, and thus the SXRL at 13.9 nm is suitable for physical experimentation as a coherent soft x-ray source. Using the picosecond SXRL, the ablation/damage phenomena of dielectric, insulator, and metal materials, and multilayer optics have been investigated. The threshold values and modification structures obtained by the picosecond SXRL were found to provide the same results as obtained by femtosecond SXRLs [10, 11]. This means that picosecond SXRL irradiation experiments can provide a good benchmark for femtosecond soft x-ray free-electron laser (XFEL) irradiation experiments and provide data for the discussion of theoretical ablation mechanisms.

However, a critical issue in self-amplified spontaneous emission (SASE) laser systems is the relatively large fluctuations in the shot-by-shot output energy. Since the SXRL is a SASE-type plasma-based x-ray laser source, the output energy fluctuates. In the SXRL at the QST, the variation in the output energy (pulse-to-pulse fluctuation) was evaluated to be 70%–80% from fifteen consecutive laser shots. The fluctuation might be large; however, the modulation of the output energy for two consecutive shots did not exceed approximately 10%, and the average of the nearest five shots was similar with a relatively small fluctuation (less than 22%). In order to use the SXRL for quantitative analyses, the SXRL beamline was developed and equipped with an intensity monitor [12].

The SXRL beamline is comprised of five parts: (1) an SXRL source, (2) an attenuator composed of zirconium (Zr) thin films, (3) an intensity monitor consisting of a Mo/Si multilayer beam splitter (BS) and x-ray charge-coupled device (CCD) camera, (4) a focusing spherical mirror with a Mo/Si multilayer coating, and (5) a sample stage. Figure 1 shows a schematic diagram of the beamline. The spatially coherent SXRL pulse is generated from silver (Ag) plasma media using an oscillator–amplifier configuration with double Ag tape targets. The intensity of each

SXRL pulse is reduced by Zr filters with various thicknesses. Zr filters also work for blocking the mostly scattered optical or unwanted x-ray radiation from the Ag plasma media.

The intensity monitor is composed of a Mo/Si multilayer BS, Zr filters, and an x-ray CCD camera. Each SXRL pulse is divided into two beams by the BS: a component transmitted through the BS, which is directed toward the Mo/Si multilayer coated spherical mirror, and a reflected component, which is directed toward the x-ray CCD camera. The x-ray CCD camera records the spatial intensity profile of the SXRL beam and serves as the intensity monitor. Zr filters installed between the BS and the x-ray CCD camera can adjust the beam intensity so that the detection capacity of the CCD camera is not saturated. The SXRL pulse towards the spherical mirror is reflected and focused onto the sample surface. The spherical mirror has a radius of curvature of 1000 mm and is set at a distance of approximately 2640 mm from the SXRL source. The mirror surface has been coated with a Mo/Si multilayer, which is optimized for soft x-rays with wavelengths of 13.9 nm, used at a near normal angle of incidence. The target material is placed in the sample holder, which is mounted on a two-axis stage. The incident angle of the SXRL beam to the sample surface can be freely set due to the rotation stage. The sample can move along the propagation direction of the SXRL to confirm the focal patterns and the optimum focal position. The sample can be moved perpendicular to the propagation direction to irradiate a fresh surface after a prescribed number of SXRL shots.

To derive the irradiation energy from the energy acquired by the intensity monitor, the relationship between the irradiation energy and the monitored energy has to be determined. Figure 2(a) shows typical measured efficiency curves of a Mo/Si multilayer BS. At an incident angle of 45°, the Mo/Si multilayer BS has a reflectivity around 45% and a transmittance around 10% for s-polarized x-rays around the 13.9 nm wavelength region. For the

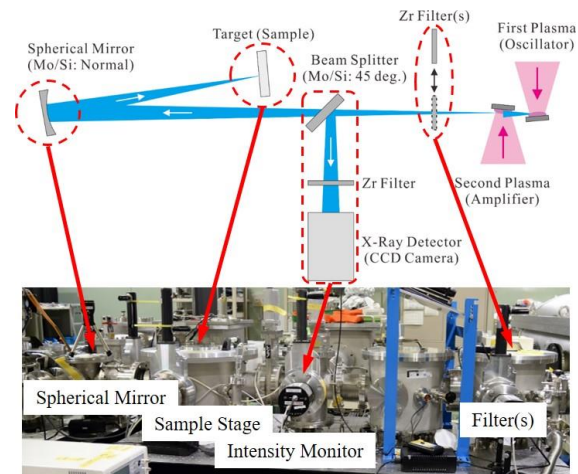


Fig. 1. Schematic diagram of the soft x-ray laser beamline.

incident p -polarized x-rays, nearly 40% of the incident x-rays are transmitted towards the spherical mirror. Due to the pseudo-Brewster's angle of the Mo/Si multilayer mirror occurring around the incident angle of 45° , the reflectivity of p -polarization x-rays is negligible. Thus, the transmittances of s - and p -polarized x-rays are different, and the SXRL signal captured by the intensity monitor is almost entirely the reflected s -polarization component. Figure 2(b) shows the calculated reflectivity and transmittance of the Mo/Si multilayer for soft x-rays as a function of the grazing incident angle. The reflectivity and transmittance for the s -polarization clearly change with the angle of incidence, whereas the transmittance for the p -polarization is almost kept constant. Therefore, one can select the grazing incident angle of the BS, such as by moving a few degrees from 45° , to increase the transmittance of s -polarized x-rays while at the same time decreasing the reflectivity, which results in an increase in the SXRL energy reaching the sample surface.

In the SXRL beamline, the Mo/Si multilayer BS is set to reflect along the horizontal direction, so that the s - and p -polarization x-rays are in accordance with the vertical and horizontal components, respectively. Thus, the intensity monitor can capture the intensity of only the reflected portion of the vertical component. The Mo/Si multilayer BS transmits both the vertical and horizontal components. The transmitted SXRL, focused by the spherical mirror, reaches the sample surface. The determination of the irradiation intensity must account for both components.

To derive the irradiation intensity that is directed onto the sample surface from the detected intensity by the intensity monitor, the relationship between the irradiation and the detection intensities must be estimated. Figure 3(a) and 3(b) show the relative intensity of the vertical and horizontal components of the SXRL pulses, respectively. The irradiation intensity directed onto the sample surface is derived from the intensity measurements as **(Irradiation Intensity) = (0.30 + 0.42) x (Monitor Intensity)**.

To confirm the focusing pattern of the SXRL, a LiF crystal was used as a detector. Producing stable color centers (CCs) in the LiF crystal with the SXRL irradiation is possible under quite low fluences of approximately 0.1 mJ/cm^2 [13]. The spatial

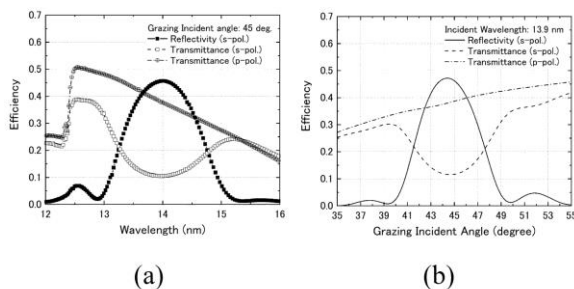


Fig. 2. (a) Measured and (b) calculated efficiencies of the Mo/Si multilayer beam splitter.

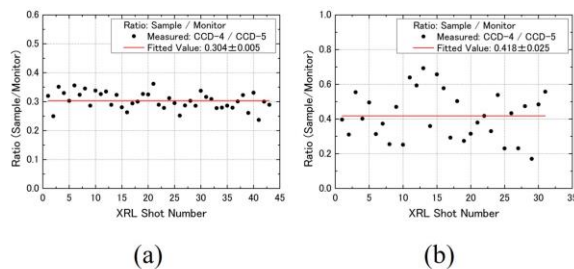


Fig. 3. Relative intensity of irradiation having (a) vertical and (b) horizontal components with respect to the intensity monitor.

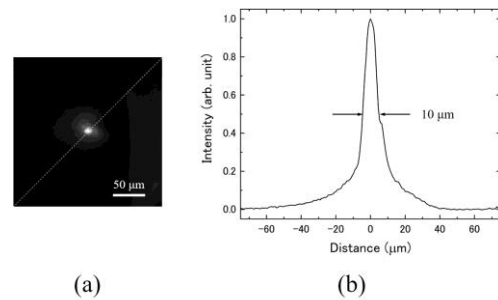


Fig. 4. (a) Fluorescence microscopy image of the photoluminescence signal emitted from color centers produced in a LiF crystal. (b) The cross-sectional profile of the photoluminescence intensity along the dotted diagonal line.

pattern of the focusing SXRL was recorded in the LiF crystal as CCs. Figure 4(a) shows the photoluminescence image of the CCs produced in the LiF crystal, which was placed at the optimum focal position. At this position, the photoluminescence signal is distributed over an area with a diameter of approximately $40 \mu\text{m}$. Figure 4(b) shows the cross-sectional profile of the signal intensity obtained from the image along the dotted diagonal line. The full width at half maximum is $10 \mu\text{m}$, and the average focal area was estimated to be approximately $100 \mu\text{m}^2$. The maximum fluence on the sample surface is approximately 30 mJ/cm^2 , which was calculated using the obtained irradiation intensity and spot area. This fluence is sufficient for ablation experiments. As an application, the sensitivity of the poly(methyl methacrylate) for picosecond SXRL irradiation was investigated using the SXRL beamline [14], with the evaluation completed successfully.

An SXRL beamline was developed for surface processing and damage studies. The beamline is equipped with an intensity monitor, which provides the laser intensity directed onto the sample. To derive the irradiation energy from the energy acquired by the intensity monitor, the characteristic features of the Mo/Si multilayer BS were evaluated and the relationship between the irradiation and detection intensities was estimated. The average focal area is estimated to be approximately $100 \mu\text{m}^2$, and the maximum fluence is approximately 30 mJ/cm^2 . This fluence is sufficient to create ablation (damage) structures on a material. The SXRL beamline will be able to contribute to the acceleration of research on SXRL-irradiation-induced phenomena.

Acknowledgments

This work was supported by JSPS KAKENHI Grant Number JP19K15402. Part of this work was supported by the Quantum Leap Flagship Program of the Ministry of Education, Culture, Sports, Science, and Technology of Japan (MEXT Q-LEAP, Grant No. JPMXS0118067246 and JPMXS0118070187).

References

1. T. Kawachi *et al.*, Appl. Opt. **42**, 2198 (2003).
2. T. Kawachi *et al.*, Phys. Rev. A **66**, 033815 (2002).
3. M. Nishikino *et al.*, Phys. Rev. A **68**, 061802(R) (2003).
4. Y. Ochi *et al.*, Appl. Opt. **46**, 1500 (2007).
5. M. Nishikino *et al.*, Rev. Sci. Instrum. **80**, 116102 (2009).
6. M. Nishikino *et al.*, Appl. Opt. **47**, 1129 (2008).
7. Y. Ochi *et al.*, Jpn. J. Appl. Phys. **48**, 120212 (2009).
8. N. Hasegawa *et al.*, Jpn. J. Appl. Phys. **43**, 2519 (2004).
9. Y. Ochi *et al.*, Appl. Phys. B **78**, 961 (2004).
10. N. A. Inogamov *et al.*, J. Opt. Technol. **78**, 473 (2011).
11. K. Mikami *et al.*, Opt. Lett. **45**, 2435 (2020).
12. M. Ishino *et al.*, Appl. Opt. **59**, 3692 (2020).
13. A. Ya Faenov *et al.*, Opt. Lett. **34**, 941 (2009).
14. Y. Hosaka *et al.*, Appl. Phys. Lett. **115**, 073109 (2019).

Compact Thomson parabola spectrometer with varying energy range and measurability of the angular distribution of low-energy laser-driven accelerated ions



Sadaoki Kojima

X-ray Laser Group, Department of Advanced Photon Research

Multi-megaelectronvolt (MeV) ion beams generated by ultra-intense laser pulses have been studied as the first stage of a compact heavy ion accelerator for cancer therapy.¹ However, at the current research stage, the quality and stability of the laser-driven ion beam is insufficient for practical medical applications.²

Thomson parabola spectrometers (TPSs) are useful instruments for studying laser-plasma interactions in which ions of multiple species are emitted simultaneously.³⁻⁶ In this study, a compact TPS with two functions is described. The first function is the measurement of the angular distribution of emitted ions, which is realized by a multi-pinhole array. The second function is the measurement of variable ion energy ranges. A variable magnetic field was generated using a permanent magnetic circuit.

TPSs obtain the energy resolution for charged particles with an ion species resolution from charge-to-mass ratios by using a combination of electrostatic and static magnetic fields.

Figure 1 shows a schematic of the TPS with a multi-pinhole configuration. The TPS is composed of a pair of multi-pinhole arrays, an electric field section, a magnetic field section, a free-flight section, and a phosphor screen detector. The pinhole array pair consists of two pinhole arrays with different pinhole arrangements and thicknesses.

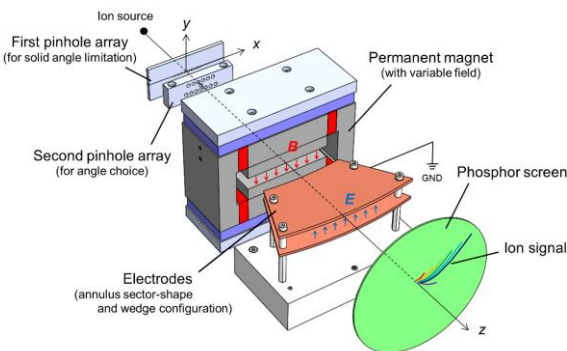


Fig. 1. Schematic of the TPS. The TPS consists of a multi-pinhole array pair, sections for electric and magnetic deflection fields, and a phosphor screen detector.

The first multi-pinhole array is for ion sampling and has 13 0.5-diameter holes to sample ions at different angles in 1° increments from -6° to 6° . The second multi-pinhole array is for angle selection. The holes along the x -direction are arranged in two rows on the y -axis. Between the two arrays, there is a single pinhole that samples ions with an incident angle of 0° from the ion source, and the upper and lower rows are pinholes that sample ions from even and odd incident angles from the target normal, respectively. The ions collimated by the pinhole array pair travel

through the magnetic field section.

Figure 2 shows a schematic of the compact permanent magnet circuit with a variable field installed in the proposed TPS. The red parts represent permanent magnets and the gray parts represent fixed yokes. The region enclosed by the fixed yokes represents the vacuum region where the ion beam passes. The shaded parts represent the movable yokes. Generally, a magnet circuit is designed so that the maximum magnetic flux passes through where the ion beam passes. In the proposed design, the flux is intentionally leaked to the movable yokes so that the magnetic field that the beam experiences can be adjusted by moving the movable yokes.⁷

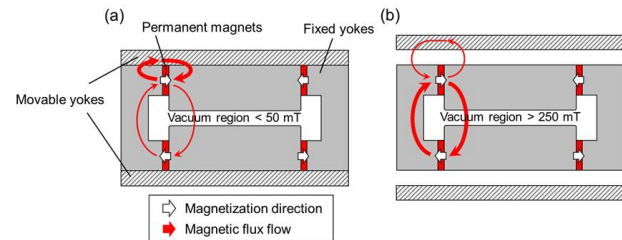


Fig. 2. Cross-sectional view of the compact permanent magnet circuit with variable magnetic flux with (a) a strong leakage to the movable yoke and (b) a weak leakage to the movable yoke.

Figure 3 presents the maximum magnetic flux density as a function of movable yoke position (red dots and line) along with the numerical result calculated by the three-dimensional finite element analysis code Femtet⁸ (black dashed line). When the movable yokes are placed close to the magnet, most of the total magnetic flux is extracted by the movable yokes; thus, the

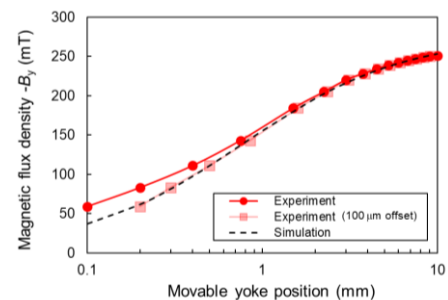


Fig. 3. Magnetic field on the ion beam with movable yoke position. Numerical results calculated by the Femtet code (black dashed line), experimental results (red dots with line), and experimental results with an offset of 100 μm (red squares with line) are shown.

magnetic field on the ion beam can be tuned by more than 80%.

The ions deflected by the magnetic field then travel through the electric field section. The first design feature is the annular sector-shaped electrodes. The annular sector shape allows the ions to receive an equivalent Lorentz force in the flight path between all pinholes and detectors. The second design feature is the wedge configuration of the electrodes in which the separation increases along the ion path. The wedge configuration provides a sufficient electric field due to the smaller gap at the front edge, and the larger gap at the last edge of the upper electrode that prevents deflected ions from hitting the electrodes.

The TPS was tested using an experiment with a compact 10-TW Ti-sapphire laser system at the Kansai Photon Science Institute of the National Institutes for Quantum and Radiological Science and Technology. The central wavelength of the laser is 795 nm and the pulse width is 80 fs. A typical laser pulse carries approximately 1 J of pulse energy to the target. The laser pulse was focused on a 5- μm thick titanium foil and a 5- μm thick polyimide film at incidence angles of 45° using an $f/2.7$ off-axis parabolic mirror. Considering the energy losses in the compressor

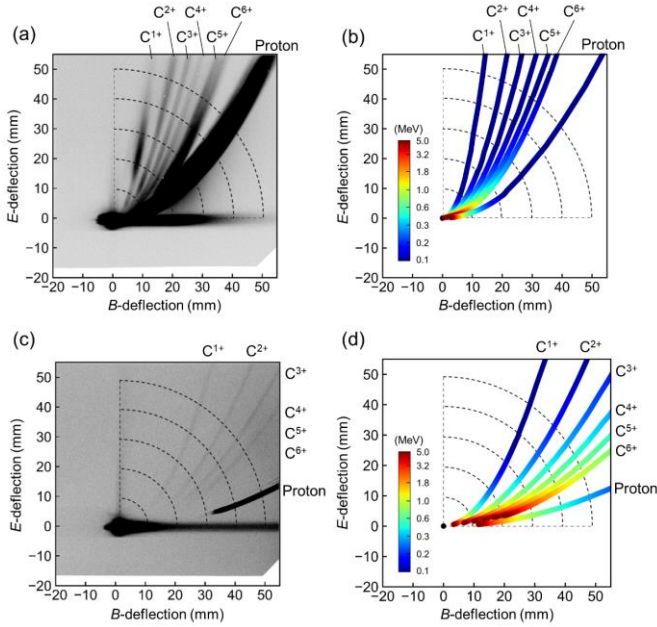


Fig. 4. (a) and (c) Parabolic traces for 100 laser shots recorded on the BAS-TR IP. (b) and (d) The corresponding calculated parabolic traces. A voltage of 1.0 kV and magnetic field of 52 mT are applied in (a) and (b) and a voltage of 5.0 kV and magnetic field of 253 mT are applied in (c) and (d). The enhanced electric and magnetic fields improve merging in the high-energy region.

gratings, the peak laser intensity on the target was typically on the order of 1019 W/cm². The detector was a BAS-TR image plate (IP), which was selected due to its sensitivity to carbon ions resulting from the absence of a plastic protective layer above the phosphor layer. Figure 4 (a) and (b) show the parabolic traces recorded on the BAS-TR IP after 100 laser shots and the calculated parabolic traces, respectively. A voltage of 1.0 kV and a magnetic field of 52 mT were applied. Figure 4 (a) shows seven parabolic traces of proton and carbon ions with charges up to C⁶⁺. The observed parabolic traces agreed well with the calculated parabolic traces. Most of the signal was recorded by proton and carbon ions in an energy region of less than 0.1 MeV, showing that the annular sector-shaped electrodes with a wedge configuration retained the lower-energy portion of the ion signal. The parabolic traces were clearly separated in the low-energy region. However, the signals merged in the high-energy region. Figure 10 (c) and (d) show the recorded and calculated parabolic traces, respectively, for an applied voltage of 5.0 kV and a magnetic field of 253 mT. Five parabolic traces of protons and carbon ions with charges up to C⁴⁺ are visible in Figure 10 (c). An ion with a larger charge state has a longer change distance for the same energy and ion species. Therefore, C⁵⁺ and C⁶⁺ carbon ions were past the observation range. The enhanced electric and magnetic fields improve merging in the high-energy region. The maximum energies of protons and carbons were found to be 1.2 MeV and 0.3 MeV (C¹⁺), 0.8 MeV (C²⁺), 1.1 MeV (C³⁺), and 1.2 MeV (C⁴⁺).

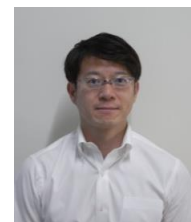
Acknowledgments

This work was supported by the International Collaborative Research Program of Institute for Chemical Research, Kyoto University (Grant 2019-7 and 2019-13), and by the Japanese Ministry of Education, Culture, Sports, Science, and Technology (MEXT) through the Japan Society for the Promotion of Science (JSPS) Grants-in-Aid for Scientific Research (KAKENHI, No. 18K13522) and JST-Mirai Program (No. JPMJ17A1).

References

1. T. Tajima et al., *Rev. of Accel. Sci. Technol.* 2, 201 (2009).
2. M. Noaman-ul-Haq et al, *Phys. Rev. Accel. Beams* 20, 041301 (2017)
3. J. N. Olsen et al., *J Appl. Phys.*, 44, 2275 (1973)
4. S. Sakabe et al., *Rev. Sci. Instrum.* 51, 1314 (1980).
A. K. Harres et al., *Rev. Sci. Instrum.* 79, 093306 (2008).
5. Yihang Zhang et al., *Rev. Sci. Instrum.* 89, 093302 (2018).
6. S. Chaurasia et al., *J. Instrum.* 11, P08004 (2016).
7. T. Watanabe et al., *Proceedings, 5th International Particle Accelerator TUPRO092*, (2014).
8. FEMTET, Murata Software Co., Ltd., 2018, <https://www.muratasoftware.com/en/>.

Microscopic imaging with a mid-infrared laser: application to histopathological analysis



M. Aoyama¹⁾, T. Morioka^{2,3)}, K. Yamakawa¹⁾

¹⁾ Medical Laser Applications Group, Department of Advanced Photon Research

²⁾ Department of Radiation Effects Research, NIRS, ³⁾ Institute for Quantum Life Science

QST has developed various “quantum beams” for material science, some of which are beginning to be applied in life science. Spectroscopy has contributed greatly to scientific understanding in the physical sciences, as it is able to provide information on the structure of the elements and molecules that comprise every subject of both the physical and biological sciences. Infrared (IR) spectroscopy has been widely applied to detect the vibrational characteristics of chemical functional groups in a diverse number of materials [1-3]. Vibrational microscopic imaging techniques using mid-infrared (MIR) spectroscopy allow for the detection and characterization of the molecular components of biological specimens. As many molecular functional groups have resonant wavelengths in this spectral range (Fig. 1), MIR absorption spectra provide image contrasts that identify the molecular components. The advantage of this technique is the production of unique images that show the spatial distribution of proteins, lipids, carbohydrates, cholesterol, nucleic acids, and phospholipids. In addition, MIR has is advantageous due to its efficiency and adaptability in noninvasive investigations of the chemical compositions of cells and tissue using a procedure that is reagentless and does not require staining. Therefore, MIR has been a fruitful tool in medical research.

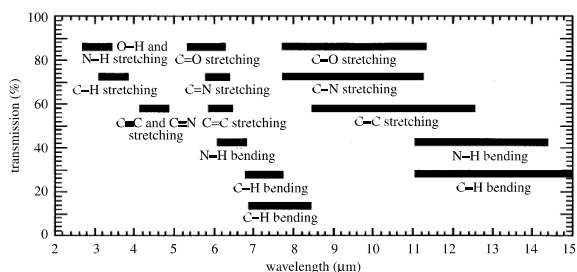


Fig.1. Correlation of various group molecular vibrations.

R. W. Waynant et al., Philos T Roy Soc A 359, 635,2001

Pathology is the study and diagnosis of diseases through the examination of organs, tissue, and cells. Disease diagnosis by pathology generally involves the gross and microscopic visual examination of tissue and cells with specialized stains employed to visualize specific proteins. Certain visualization techniques, such as special staining, immunohistochemistry, and electron microscopy, have expanded the means by which pathologists can diagnose diseases. However, it is difficult to detect visually biochemical changes using these techniques, and they require complicated processes and considerable amounts of time. Therefore, the development of a simple analytical technique is desired. MIR spectroscopy has the potential for application to visualization tools to aid pathologists in assessing tissue specimens.

The purpose of this study is to investigate the discrimination between normal tissue and malignant tumors of various organs using a MIR laser. For the analysis of tissue specimens, a MIR

microscopic system was constructed. A schematic diagram of this system is shown in Figure 2. The beam from the MIR laser is focused on a spot on the specimens. The transmitted beam intensity is measured with a detector. In order to obtain a MIR microscopic mapping image, the focused spot scans across the specimens in one direction while scanning one pixel in the orthogonal direction using an X-Y stage. The results of the two different tissue specimens measured with the MIR microscopic system are described here. The first measurements are a mapping image and the spectra of a specimen with a simple structure consisting of normal tissue and its malignant tumor. Furthermore, the measured results of a specimen with a relatively complex structure containing multiple types of normal tissue and malignant tumors are presented.

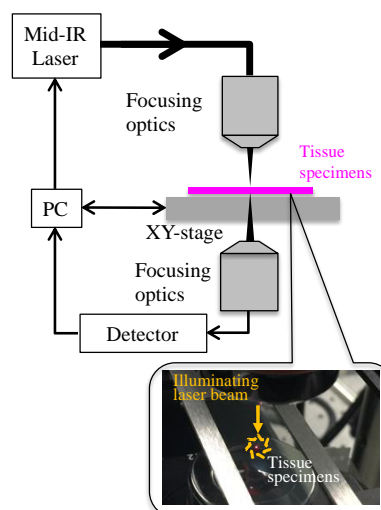


Fig.2. Mid-IR microscopic imaging system.

For the tissue specimen with a simple structure, a hematopoietic tumor invading the liver and the normal liver tissue of a mouse was analyzed and compared with the absorbance obtained from an unstained tissue specimen (Fig. 3). Figure 3a shows an optical micrograph of the H&E-stained tissue specimen containing the hematopoietic tumor and normal liver tissue. Figure 3b illustrates the MIR spectra of the normal liver tissue and hematopoietic tumor from three different sites in normal and tumor areas, and shows that the spectral patterns in the tumor (red lines) differed from those in the normal tissue (blue lines). The majority of changes in absorbance were observed in the two different regions (green double-headed arrows, Fig. 3b). Microscopic mapping of the hematopoietic tumor was then conducted to investigate the absorbance of the tumor cells. The infiltrated hematopoietic tumor area for the mapping was determined by examining the MIR microscopic field as compared with the corresponding histopathological view (Fig. 3a). Figure

3c displays the MIR absorbance map of the hematopoietic tumor infiltrating into the liver. The color classification based on the MIR absorbance changes segments the three main components: hematopoietic tumor (orange) and normal liver tissue (green), and the mixed regions of the tumor cell and normal liver tissue, indicated in yellow.

The results for the specimen with a complex structure are shown in Figure 4. The specimen includes a malignant tumor (rhabdomyosarcoma tumor) and several types of normal tissue (muscle, bone, and bone marrow). It was analyzed by a comparison with the absorbance obtained from an unstained

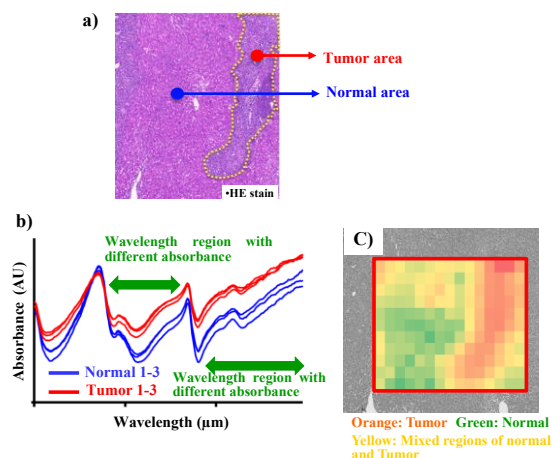


Fig.3. The spectra and visible image from tissue specimen by MIR microscopy in hematopoietic tumor sample.

- a) Optical micrograph of H&E-stained tissue specimen of normal liver and hematopoietic tumor invading the liver.
- b) The corresponding absorbance MIR spectra of the unstained same tissue at three different sites in normal and tumor areas.
- c) The MIR imaging of tumor and normal tissue.

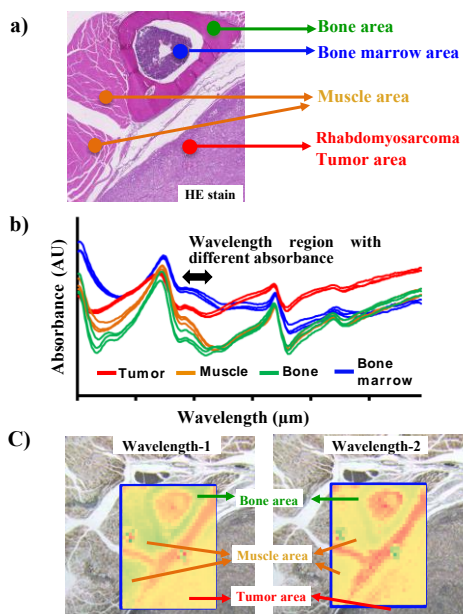


Fig.4. The spectra and visible image from tissue specimen by MIR microscopy in rhabdomyosarcoma sample containing different tissues.

- a) Optical micrograph of a H&E-stained tissue specimen of rhabdomyosarcoma and different tissues.
- b) The corresponding absorbance MIR spectra of the unstained same tissue at three different sites in each tissue areas.
- c) The microscopic images with MIR laser at different wavelengths .

tissue specimen. Figure 4a shows an optical micrograph of the H&E-stained tissue specimen. The MIR spectra in Figure 4b demonstrate that the spectral patterns differ between the rhabdomyosarcoma tumor area (red lines), muscle (brown lines), bone (green lines), and bone marrow (blue lines). The greatest change in absorbance was observed in the region marked by black double-headed arrows (Fig. 4b). Next, microscopic mapping was conducted for these tissues to obtain information on the absorbance of each cell using wavelengths demonstrating a differing absorbance. The area including these tissues was determined by examining the MIR microscopic field as compared with the corresponding histopathological view (Fig. 4a). Figure 4c illustrates the MIR absorbance maps of this area as measured with two different wavelengths. The color classification result based on the MIR absorbance at Wavelength 1 colors the rhabdomyosarcoma tumor in yellow, and both the muscle and bone in green. Furthermore, the muscle and bone, which have the same color classification at Wavelength 1, are discriminated as yellow and green by using Wavelength 2. The analysis using multiple wavelengths permits the detailed classification of more types of tissue.

This study indicates that the MIR spectroscopic technique is useful for diagnosing and discriminating the differences between not only normal tissue and malignant tumors, but also tissue with complex structures, such as those containing multiple types of normal tissue and malignant tumors. Although MIR spectroscopy has several advantages, it is not yet known whether the spectral information from the proposed device can satisfy pathological diagnostic requirements and assist pathologists in diagnoses. Thus, further investigation and improvements of the proposed MIR spectroscopy are necessary for these approaches to become applicable to routine histopathological analysis. In addition, *in vivo* diagnostic tools using the MIR laser are required in many fields of medicine. These include endoscopy for guidance in surgical interventions to delineate lesion margins, replacing random biopsies of suspicious tissue by targeted biopsies, which would reduce unnecessary tissue excisions and risks with biopsy, and a detection device at a significantly earlier stage of carcinogenesis. Future improvements in the MIR laser technology and data analysis will further extend the biomedical applicability and finally result in the implementation of these innovative techniques in the medical field.

Collaborators

K. Ogawa⁴⁾, T. Imaoka^{2,6)}, A. Yokoya^{5,6)}, and S. Kakinuma²⁾

2) Department of Radiation Effects Research, 4) Light Touch Technology Inc., 5) Tokai Quantum Beam Science Center, 6) Group of Quantum and Cellular Systems Biology, QST Advanced Study Laboratory

Acknowledgments

Ms. M. Kaminishi, Y. Nishimura, and M. Shinagawa from the Department of Radiation Effects Research are thanked for the preparation of the histological samples.

This research was supported by QST President's Strategic Grant (Creative Research).

References

1. Meier RJ. 2005. *Chem Soc Rev* 34:743-52
2. Grasselli JG, Mehicic M, Mooney JR. 1986. *Fresen Z Anal Chem* 324:537-43
3. Waynant RW, Ilev IK, Gannot I. 2001. *Philos T Roy Soc A* 359:635-44.

Research Activities at the Synchrotron Radiation Research Center

Yoshinori Katayama
Synchrotron Radiation Research Center



At the Synchrotron Radiation Research Center (SRRC), we are continuing to develop a wide range of x-ray techniques for investigating the structural and electronic properties of matter, primarily using the two QST beamlines at SPring-8, a large synchrotron radiation facility. As well as precise measurements of high-quality crystalline samples, we have been concentrating on developing techniques that are applicable to inhomogeneous materials, which play an important role in determining the functions of many practical materials. The equipment that we develop is open for public use, and in FY2020, we accepted twenty-four research proposals as a member institute of the Nanotechnology Platform Japan [1].

The SRRC consists of three experimental groups, one theory group, and a beamline operation office (Table 1). This year, we continued our research while taking measures to prevent the spread of COVID-19. Although the suspension of user operation at SPring-8 from April to May delayed our research, notable achievements have been made. The research activities of each research group are summarized below.

Highly brilliant synchrotron/FEL x-ray/VUV facilities are being constructed throughout the world at a rapid pace. In the **Coherent X-ray Research Group**, to stay at the forefront of synchrotron/FEL research, we are continuing to develop advanced measurement/analysis techniques for the effective use of these new advanced light sources. The use of spatially coherent x-rays from highly brilliant synchrotron/FEL light sources has made it possible to visualize the inhomogeneity inside matter. We are now building an apparatus for Bragg coherent x-ray diffraction imaging (Bragg-CDI) and applying it to the study of inhomogeneous structures of sub-micrometer sized ferroelectric crystals. We have also developed a microscope for imaging topological defects [2].

To exploit the temporal coherence and intensity offered by next-generation light sources at short wavelengths, we are developing new nonlinear and quantum optical techniques using simple atomic systems. We used SACLA's soft x-ray beamline to observe the 'superfluorescence' phenomenon at extreme ultraviolet wavelengths for the first time. To extend the technique to even shorter wavelengths and for improved pulse control, we are developing a source of superfluid liquid helium droplets for use at SACLA. The new source can also provide an 'ultracold nano laboratory' for studying isolated molecules with synchrotron radiation. Recently, synchrotron radiation at two different energies was used to study the inner-shell decay processes in krypton, using the $2p-1s$ fluorescence lifetime (167 as) as a natural stopwatch to access timescales even shorter than those accessible with SACLA [3].

Using a surface x-ray diffractometer coupled with a molecular beam epitaxy chamber, in situ measurements of crystal truncation rod (CTR) scattering were taken to investigate the atomic structure of gallium nitride surfaces under growth conditions. From the CTR profile analysis, we experimentally confirmed the existence of a pseudo 1×1 structure, and determined the structural parameters (interlayer distance, coverage, and temperature factor).

The research objectives of the **High Pressure Science and Stress Research Group** are (i) the development of experimental techniques for in-situ measurements under extreme conditions, including high-pressure conditions, compressed hydrogen gas environments, and elasto-plastic stress fields, and (ii) fundamental and applied studies of advanced functional materials using the above-mentioned techniques. The research group members focus on the study of the nano- to meso-scale structures of functional materials, and the high-pressure synthesis of novel hydrogen-rich compounds. In order to advance the investigation of the nano- to meso-scaled structures, the group has closely collaborated with the Coherent X-ray Research Group.

Metal-hydrogen systems are a primary research target of this group. The high-pressure synthesis and crystal structure of novel hydrogen-containing compounds, for example transition metal and aluminum-based materials, has been investigated, and some novel compounds have been synthesized. We have successfully synthesized a novel hydride $\text{Co}_3\text{TiH}_{-4}$ at 9 GPa and 900 °C, finding that $\text{Co}_3\text{TiH}_{-4}$ is thermodynamically stable above 1 GPa from in-situ synchrotron radiation x-ray diffraction [4]. In-situ x-ray and neutron diffraction experiments on the Fe-D system at high-pressure and high-temperature conditions revealed the pressure and temperature variations in the crystal and magnetic structures of dhcp- FeD_x [5]. An atomic pair-distribution function (PDF) analysis, which is a powerful tool for studying the local structures of functional materials, was applied to investigate the hydrogenation process of an $\text{Mg}_{0.7}\text{Ti}_{0.3}$ thin film. While it is difficult to obtain the PDFs of thin films, we successfully obtained the PDFs for an $\text{Mg}_{0.7}\text{Ti}_{0.3}$ thin film in a hydrogen gas environment and found the formation of TiH_2 clusters with a size of approximately 3 nm in the Mg matrix [6]. The PDF analysis has also been applied to other advanced functional materials, such as the negative thermal expansion oxide $\text{BiInO}_3\text{-BiZn}_{1/2}\text{Ti}_{1/2}\text{O}_3$ solid solution [7].

We have been investigating irradiation effects on tumors with nanoparticles containing high-Z elements [8]. Auger electrons emitted from high-Z elements from synchrotron x-ray irradiation are expected to destroy tumors effectively. Tumor spheroids containing Gd-loaded nanoparticles were irradiated by synchrotron radiation monochromatic x-rays. Complete

destruction of the tumor spheroid was observed using x-rays with $E = 50.25$ keV, which is just above the Gd K-absorption edge. The destruction mechanism is being investigated.

In many functional materials and devices, ranging from high- T_c superconducting oxides to spintronic devices, the electron's spin degrees of freedom play important roles. In the **Magnetism Research Group**, in order to unveil the functionality of such materials and devices, advanced x-ray spectroscopic techniques such as nuclear resonant scattering (NRS), resonant inelastic x-ray scattering (RIXS), and x-ray magnetic circularly polarized emission (XMCPPE), are being developed. For NRS, synchrotron-based Mössbauer spectroscopy using a frequency-domain technique has been conducted by incorporating a nuclear Bragg monochromator. By utilizing an iron-57 probe layer method and a newly installed ultra-high vacuum chamber, we observed the spatial modulation of magnetic moments from the surface to the bulk in an iron thin film for the first time [9]. RIXS has been applied to study electronic states of $5d$ transition metal compounds in which strong spin-orbit coupling opens up a new frontier of correlated electron systems. New optical elements for W L_3 -edge were installed and excitations of $5d$ electrons in some W compounds were measured. XMCPPE is a novel magnetic spectroscopy in the hard x-ray regime. A distinctive feature of a large flipping ratio ($> 10\%$) for the $K\alpha$ emission of $3d$ transition metal elements. Recently, we developed a theoretical framework for calculating the XMCPPE spectra of itinerant ferromagnets and successfully reproduced the observed $K\alpha$ XMCPPE spectra of metallic iron by including electron excitations in the d bands [102]. Test measurements of a scanning magnetic microscope utilizing XMCPPE spectroscopy are being performed.








The **Condensed Matter Theory Group** develops advanced simulation methods based on quantum mechanics to investigate the theory of condensed matter using supercomputers. The

methods are also applied to perform numerical simulations aimed at understanding various properties of materials such as magnetism, high- T_c superconductivity, and catalytic activity, with the support of x-ray experiments such as from SPring-8. Current activities include (i) the development of advanced simulation techniques based on first principles path integral molecular dynamics for investigating the nuclear quantum effects of hydrogen-containing materials such as clathrate hydrates [11]; (ii) the development of a numerically exact diagonalization method to investigate time-resolved spectroscopies of antiferromagnetic Mott insulators, which can provide new insights into their electronic dynamics; (iii) the development of a theoretical framework and computational codes to analyze material properties probed by x-ray spectroscopies, such as x-ray magnetic circular dichroism (XMCD), RIXS, and XMCPPE [10]; and (iv) theoretical investigations using large-scale numerical exact diagonalization of quantum spin systems found in hypermaterials, which exhibit some novel quantum phases such as spin nematic liquid.

References

1. <http://www.kansai.qst.go.jp/nano/>
2. Y. Kohmura *et al.*, Opt. Express **28**, 24115 (2020).
3. S. Kosugi *et al.*, Phys. Rev. Lett. **124**, 183001 (2020).
4. H. Saitoh, *et al.*, Int. J. Hydrogen Energy **45**, 33675 (2020).
5. H. Saitoh, *et al.*, Sci. Rep. **10**, 9934 (2020).
6. H. Kim, *et al.*, Inorg. Chem. **59**, 6800 (2020).
7. T. Nishikubo, *et al.*, Chem. Mater. accepted.
8. F. Tamanoi, *et al.*, Nanomaterials **10**, 1341 (2020).
9. T. Mitsui *et al.*, Phys. Rev. Lett. **125**, 236806 (2020).
10. A. Koide *et al.*, Phys. Rev. B **102**, 224425 (2020).
11. T. Ikeda, Chem. Phys. Lett. **763**, 138222 (2021).

Table 1. Groups at the Synchrotron Radiation Research Center.

Group	Coherent X-ray Research Group	High Pressure Science and Stress Research Group	Magnetism Research Group	Condensed Matter Theory Group
Members	K. Ohwada(GL), J. Harries, T. Sasaki, (M. Takahasi)	T. Watanuki (GL), A. Machida, H. Saitoh, A. Shiro, (R. Yasuda)	T. Inami (GL), T. Mitsui, K. Ishii, T. Ueno, A. Koide, (A. Agui)	(T. Sakai (GL)), T. Ikeda, K. Tsutsui, T. Nomura
Typical techniques & apparatuses	Coherent x-ray scattering  Surface x-ray diffraction  Quantum optics in EUV region	High-pressure and high-temperature x-ray diffraction  Pair distribution function analysis 	Mössbauer spectroscopy  Resonant inelastic x-ray scattering  X-ray magnetic circularly polarized emission	First principles molecular dynamics simulations, numerical calculations 
Research objective	nitride semiconductors, ferroelectrics	hydrogen containing materials, negative thermal expansion materials	magnetism, spintronics, high- T_c superconductivity, adaptive design of experiment	hydrogen containing materials, high- T_c superconductivity, catalysis, magnets
Beamline Operation Office/ Y. Katayama(Section Manager), Y. Teraoka, Y. Kai, K. Sugawara				

Hydrogenation reaction of Co₃Ti alloy under high pressure

Hiroyuki Saitoh



High Pressure Science and Stress Research Group, Synchrotron Radiation Research Center

Titanium and its alloys have high hydrogen affinities, and thus, have been widely investigated for hydrogen storage applications. Since the pure Ti hydride TiH₂ is too stable to use in hydrogen storage, metals with low hydrogen affinity are alloyed with Ti to decrease the thermodynamic stability of their hydrides. TiFe is a typical Ti-containing hydrogen storage alloy [1]. Attempts have been made to hydrogenate known Ti-containing hydrogen storage alloys under high-pressure and temperature conditions to obtain a hydrogen rich phase. The chemical potential of hydrogen increases significantly above 1 GPa [2], and thus, novel hydrides are expected to be synthesized above 1 GPa. For example, the hydrogenation reaction of TiFe alloy at 10 GPa yielded a novel TiFe hydride [3].

In the present study, the hydrogenation reaction under high pressure of Co₃Ti alloy with a Cu₃Au-type structure was investigated. Hydrogenation reactions of Co₃Ti alloy have been investigated considering the hydrogen embrittlement of the alloy. Formation of Co-23at%TiH_x for $x < 1.0$ has been reported, in which the cathodic charging method was used to hydrogenate the alloy [4]. In this study, a novel hydrogenation reaction of Co₃Ti alloy under high pressure is explored to obtain a novel hydride with a higher hydrogen content than Co₃TiH₋₁, the previously reported hydride. The reaction process under high pressure was monitored by in situ synchrotron radiation x-ray powder diffraction. A novel hydrogen-rich hydride Co₃TiH₋₄ was formed at 9 GPa and 900 °C [5]. The hydride decomposed into the previously reported Co₃TiH₋₁ and hydrogen during a decomposition process; Co₃TiH₋₄ cannot be recovered at ambient conditions.

The starting material was small pieces (less than 100 μm in length) of Co₃Ti alloy with the Cu₃Au-type structure prepared by melting a powder mixture of pure titanium and cobalt at 1400 °C under ambient pressure. A boron nitride capsule was filled with the sample, pressurized to 9 GPa at room temperature, and heated to 900 °C. The sample was kept in fluid hydrogen for 60 min, cooled to room temperature, and depressurized to ambient pressure.

A cubic-type multi-anvil high-pressure apparatus was used to generate the high-pressure and high-temperature conditions. AlH₃ was used as an internal hydrogen source that evolves hydrogen under high-pressure and high-temperature conditions. The evolved hydrogen was confined in a hydrogen-sealing capsule made of NaCl along with the sample. The structural changes of the sample under high pressure were monitored by an in situ synchrotron radiation x-ray diffraction system installed at the beamline BL14B1 at SPring-8 [6]. The recovered sample was characterized via a conventional x-ray micro-diffractometer.

Figure 1 shows the in situ synchrotron radiation powder x-ray diffraction profiles of the sample under high pressure. The sample maintained the Cu₃Au-type structure under compression up to 9 GPa at room temperature. When the sample was heated to 900 °C at 9 GPa, a discontinuous lattice expansion was observed at 900 °C after continuous lattice expansion due to thermal expansion. The discontinuous lattice expansion was caused by the formation of Co₃Ti hydride with the Cu₃Au-type structure. The metal lattice remained unchanged during the hydrogenation reaction, indicating that the formed hydride is an interstitial hydride. The hydrogen composition was approximately estimated as Co₃TiH₋₄ based on the relationship between the magnitude of the unit cell volumetric expansion and the hydrogen composition [1]. It may be observed that the diffraction peaks of Co₃TiH₋₄ are sharp, although hydrogen atoms were inserted into the interstices of the metal lattice of Co₃Ti. This is because lattice relaxation and the hydrogenation reaction occurred simultaneously at 900 °C and 9 GPa; the lattice relaxation resulted in the sharp diffraction peaks of Co₃TiH₋₄. After a one-hour heat treatment, the sample was cooled to room temperature and depressurized to ambient pressure at room temperature.

The formed Co₃TiH₋₄ evolved hydrogen at a pressure of 1 GPa during the depressurization. As shown in Figure 1, a lattice contraction was observed below 1 GPa, indicating a hydrogen evolution from the formed hydride. The unit cell volume of the recovered sample was calculated to be 50.8 Å³, which is 3.5 Å³ larger than that of the Co₃Ti alloy without hydrogen (comparing the peak positions of the upper and lower profiles of Figure 1). The calculated unit cell volume indicated that the recovered sample was Co₃TiH₋₁.

The recovered sample (Co₃TiH₋₁) gradually evolved hydrogen at ambient pressure, whereas the sample was a single-phase Co₃TiH₋₁ immediately after the sample was recovered at ambient conditions. One hour after the sample was recovered at ambient conditions, the sample contained two phases having the same Cu₃Au-type structure with lattice constants of $a = 3.704 \pm 0.005$ Å and 3.618 ± 0.004 Å, respectively. The former was Co₃TiH₋₁ and the latter was Co₃Ti without hydrogen. Co₃TiH₋₁ is thermodynamically unstable at ambient conditions.

The possible hydrogen sites in Co₃TiH₋₄ and Co₃TiH₋₁ were considered. It is likely that hydrogen atoms are located at the octahedral sites in Co₃TiH₋₄ since the number of the octahedral sites corresponds to the hydrogen composition. There are four octahedral sites in Co₃Ti, and all the octahedral sites are expected to be occupied by hydrogen atoms to form Co₃TiH₋₄.

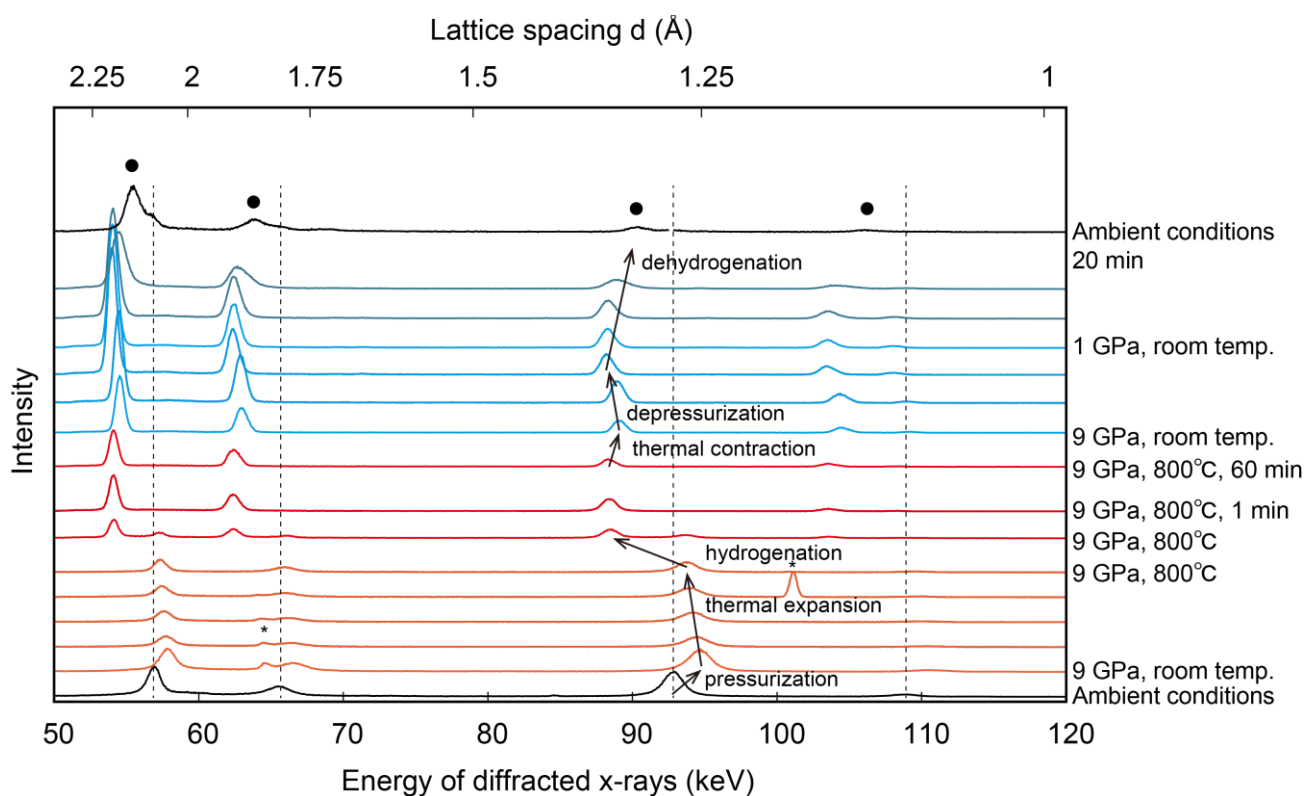


Figure 1. In situ synchrotron radiation powder x-ray diffraction profiles of Co_3Ti alloy under high hydrogen pressure. Bragg peaks from the Cu_3Au -type structure are indicated by filled circles. Bragg peaks with asterisks are from a sample capsule. Dashed lines denote the location of peaks of pristine Co_3Ti alloy at ambient conditions.

There are two types of octahedral sites in Co_3Ti alloy: sites consisting of six Co atoms (Co_6 octahedral site), and sites with four Co and two Ti atoms (Co_4Ti_2 octahedral site). Co_3Ti contains one Co_6 octahedral site and three Co_4Ti_2 octahedral sites. As described above, $\text{Co}_3\text{TiH}_{-4}$ decomposed into $\text{Co}_3\text{TiH}_{-1}$ during depressurization and three hydrogen atoms evolved from the dehydrogenation reaction. Presumably, hydrogen atoms in Co_4Ti_2 octahedral sites are evolved during depressurization since the amount of hydrogen evolved during depressurization corresponds to the number of Co_4Ti_2 octahedral sites. Hydrogen atoms in Co_4Ti_2 octahedral sites seem to be less stable than those in the Co_6 octahedral site, despite the presence of Ti with high hydrogen affinity. This result seems consistent with the previously reported result for the Mg-containing hydride MgPdD_x , which is an interstitial hydride with the same Cu_3Au -type structure. Deuterium occupied the octahedral interstices surrounded exclusively by Pd atoms (Pd_6 site), although there is an octahedral site composed of Mg (Pd_4Mg_2 site) with high hydrogen affinity [7].

The recovered $\text{Co}_3\text{TiH}_{-1}$ decomposed gradually under ambient conditions and evolved hydrogen at 115 °C at ambient pressure. The thermal stability of $\text{Co}_3\text{TiH}_{-1}$ is comparable to that of fcc CoH_x . This is probably due to the similar local structure surrounding the hydrogen atoms. The local structure around the hydrogen atoms in the Co_6 octahedral site of $\text{Co}_3\text{TiH}_{-4}$ is identical to the structure in fcc CoH_x .

Acknowledgments

The author thanks M. Morimoto, T. Watanuki, T. Sato, S. Takagi, and S. Orimo for their contributions. This work was supported by Grants-in-Aid for Scientific Research (KAKENHI), “Hydrogenomics” (Grant No. JP18H05513) from the Japan Society for the Promotion of Science as well as grants from the Inter-University Cooperative Research Program of the Institute for Materials Research, Tohoku University (Proposal No. 17K0026, 18K0032, and 19K0049).

References

1. J. J. Reilly and R. H. Wiswall, *Inorg. Chem.* **13**, 218 (1974).
2. Y. Fukai, *The Metal-Hydrogen System*. Second. Berlin: Springer; (2005).
3. N. Endo, H. Saitoh, A. Machida, and Y. Katayama, *Int. J. Hydrogen Energy* **38**, 6726 (2013).
4. H. Saitoh, M. Endoh, T. Aoyama, T. Sugimoto, T. Misawa, and T. Ohnishi, *J. Mater. Sci. Lett.* **15**, 23 (1996).
5. H. Saitoh, M. Morimoto, T. Watanuki, T. Sato, S. Takagi, and S. Orimo, *Int. J. Hydrogen Energy* **45**, 33675 (2020).
6. H. Saitoh, A. Machida, and K. Aoki, *Chinese Sci. Bull.* **59**, 5290 (2014).
7. H. Kohlmann, G. Renaudin, K. Yvon, C. Wannek, B. Harbrecht, *J. Solid State Chem.* **178**, 1292 (2005).

Inner-shell atomic lifetimes as a ‘stopwatch’ for studying Auger decay

James R Harries



Coherent X-ray Research Group, Synchrotron Radiation Research Centre

To study the dynamics of electrons in matter on its natural timescale requires techniques which can access femto- and attosecond timescales. At visible wavelengths attosecond pulses of light are available using high-harmonic generation (HHG) technology. To study tightly bound electrons however requires X-ray pulses. The HHG technology can be extended to short wavelengths, but at a loss of intensity. X-ray free-electron lasers offer pulse widths of tens to hundreds of femtoseconds, but with only partial coherence and an inherent time jitter. Here we show that it is possible to access the attosecond timescale even with synchrotron radiation, which has a pulse length of tens of picoseconds or longer.

Experiments were performed at two different beamlines to study an effect called post-collision interaction in Kr gas. Radiation incident on an atom can lead to the emission of an electron if the photon energy is sufficient (photoelectric effect). At X-ray energies, electrons can be emitted from energy levels deep within the atom, leaving a ‘hole’ in an inner shell. These ‘inner-shell excited states’ are highly unstable, and decay rapidly by an electron in a higher energy level filling the hole, releasing energy. This energy is either emitted as radiation (fluorescence decay), or by the emission of another electron (Auger decay). Which process occurs depends on the properties of the states involved. For Kr, a 1s hole decays predominantly by fluorescence, whereas a 2p hole decays predominantly by Auger decay. When

the incident radiation is close to the threshold for ejecting the initial electron, the emitted photoelectron has a low kinetic energy. Auger electrons usually have high kinetic energies, and can ‘overtake’ the photoelectron. This process leads to a change in the kinetic energies of both electrons, which can be observed using a high-resolution electron energy analyser.

In this experiment we studied the post-collision interaction between Auger electrons and photoelectrons emitted following the decay of a 2p ‘hole’, created in two different ways. Using a photon energy of 1.7 keV the state was created directly by direct photoionization (figure 1a). Using a photon energy of 14 keV, the 2p hole state was created by first ionizing a 1s electron (figure 1b). This excited 1s hole state decays by emitting fluorescence as a 2p electron fills the hole, with a natural radiative lifetime of 167 as. Comparing these two processes, the photoelectron for process b) has moved further away from the atom than that of process a) at the instant the 2p hole state is created.

The 2p hole state decays by ‘LMM’ Auger decay, with an electron from the $n = 3$ shell filling the 2p hole and ejecting a further $n = 3$ electron (figure 2). Here ‘LMM’ refers to the three electrons involved: a hole in the ‘L’ shell is filled by an electron from the ‘M’ shell, and the excess energy is taken away by a further electron from the ‘M’ shell. This creates a fast Auger electron. Since the Auger electron has a higher kinetic energy than the photoelectron, the Coulomb interaction between the two

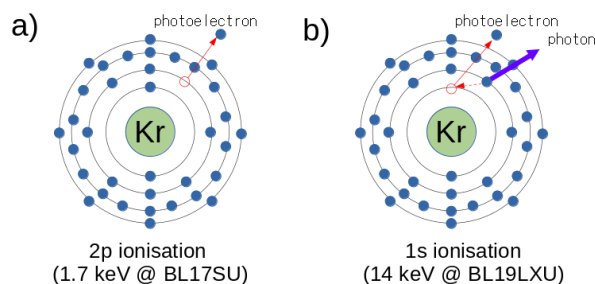


Figure 1. Inner-shell photoionisation

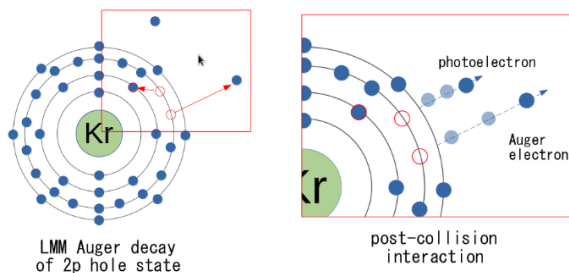


Figure 2. Auger decay and PCI

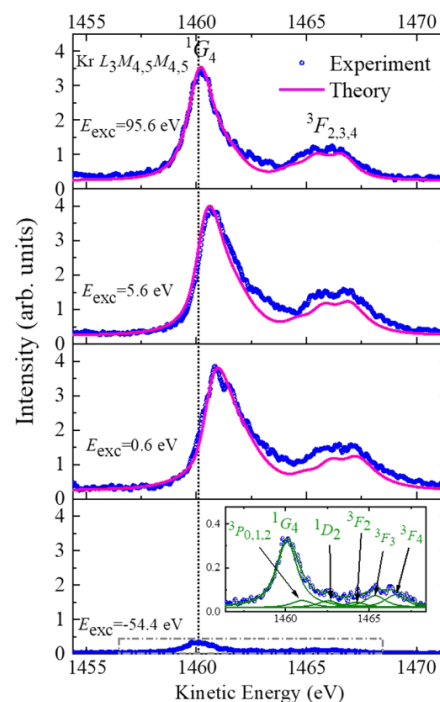


Figure 3. electron spectra following K-shell photoionization.

affects both of their energies, leading to a ‘speeding up’ of the Auger electron and a ‘slowing down’ of the photoelectron as it experiences a stronger Coulomb potential from the remaining now doubly-charged ion.

Figure 3 shows electron spectra recorded at photon energies ranging from below threshold (bottom) to far above threshold (top). The main peak near 1460 eV corresponds to emitted Auger electrons, and it is clear that this peak shifts to higher energies closer to threshold – this is the PCI effect described above.

The key point to this work is the comparison between Auger electron spectra recorded following K-shell photoionization (14 keV) and L-shell photoionization (1.7 keV). As described above, both of these processes lead to LMM Auger emission following the creation of a 2p hole, but the difference is that there is a time delay between photoionization and the creation of this hole for the former case, due to the fluorescence decay $2p - 1s$.

Figure 4 compares the results from the two situations. Both experimental spectra (blue dots, cyan triangles) show the same LMM Auger line, at a kinetic energy near 1460 eV. The spectra were recorded with photon energies 0.6 eV above either the K-shell threshold (blue) or the L-shell threshold (cyan). It is clear that despite the photoelectron in each case having the same kinetic energy (0.6 eV) and the Auger electron having the same initial kinetic energy (this is determined purely by the electronic state energies) there is a shift of around 0.2 eV between the two cases, with the electron detected at a lower energy for 1s ionization. This can be understood by considering the time delay due to the $2p - 1s$ fluorescence. During this time the photoelectron has moved further away from the remaining ion, so the PCI effect also occurs at a later time (larger wavefront radius). This reduces the PCI effect due to the smaller change in Coulomb field as the Auger electron ‘overtakes’ the photoelectron. Figure 3 shows that the PCI effect increases the Auger electron’s kinetic energy – and figure 4 thus shows that the PCI effect is stronger for 2p ionization (no time delay) than for 1s ionization (time delay due to fluorescence).

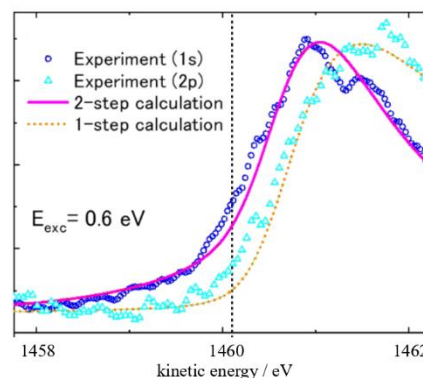


Figure 4. Comparison between K- and L-shell ionisation

The energy difference between the two peaks in figure 4 is thus a direct effect of the fluorescence lifetime of the $1s$ hole state, showing that electron spectroscopy even using synchrotron radiation can allow us to access the attosecond timescale. For more details, and a description of theoretical calculations which explain the results quantitatively please refer to reference [1].

Acknowledgments

This work was performed as part of a collaboration led by S Kosugi, F Koike, and Y Azuma (Sophia University).

References

1. Kosugi S, Koike F, Iizawa M, Oura M, Gejo T, Tamasaku K, Harries J R, Guillemin R, Piancastelli M N, Simon M and Azuma Y 2020 *Phys. Rev. Lett.* **124** 183001.

Magnetic Friedel Oscillation at Fe(001) Surfaces: Direct Observation by Atomic-Layer-Resolved Synchrotron Radiation ^{57}Fe Mössbauer Spectroscopy

Takaya Mitsui

Magnetism Research Group, Synchrotron Radiation Research Center



The study of the surface and interface magnetism of 3^d transition metals is of interest due to the essential role that magnetism plays in determining magnetic interactions and spin-transport properties of nanomagnets and magnetic hetero junctions. Over the past few decades, various techniques have advanced the research on surface and interface magnetism. However, few experimental studies have investigated the depth-dependent local magnetic structures of surfaces and interfaces at the atomic layer level. This is due to the difficulties encountered when performing depth-resolved studies at the uppermost surface of a metal, such as with scanning tunneling microscopy, or due to the signal arising from a relatively broad depth range, e.g., with x-ray magnetic circular dichroism spectroscopy.

The surface magnetism of Fe(001) is a fascinating research subject for atomic-layer-resolved magnetic analysis. Theoretical studies predict a 30% enhancement of the magnetic moment M_{Fe} at the surface and an oscillatory behavior with increasing depth in the individual layers, i.e., a magnetic Friedel oscillation [1]. As a related phenomenon, Ohnishi et al. theoretically predicted that the hyperfine magnetic field H_{int} is reduced by 30% relative to the bulk value despite a significant increase in the surface M_{Fe} [2].

Recently, we determined the layer-by-layer H_{int} of the Fe(001) surface by the in situ ^{57}Fe probe layer method with a high brilliance synchrotron Mössbauer source [3]. In this method, a resonant isotope probe layer is embedded in a thin film prepared with a non-resonant isotope. The observed H_{int} at the nucleus provides details on the local surface magnetism.

Fe(001) films were fabricated by alternatively evaporating ^{56}Fe and ^{57}Fe from 99.94% iron-56 and 95.93% ^{57}Fe isotopic sources onto pre-cleaned $10 \times 10 \times 0.5 \text{ mm}^3$ MgO(001) substrates under a vacuum pressure of approximately 10^{-8} Pa . A 0.8-ML thick ^{57}Fe probe layer ($t = 0.1 \text{ nm}$) was embedded to the depth of the N th atomic layer below the surface where $N = 1$ to 4 and 7. These samples are hereafter referred to as “ N th probe layer samples”.

The experiments were performed at the BL11XU beamline of SPring-8 using linearly π -polarized 14.4 keV Mössbauer γ -rays with a 15.4 neV bandwidth produced by a synchrotron Mössbauer source. The γ -ray beam was vertically focused by an elliptical mirror. The beam size was $15 \mu\text{m}$ (V) \times 1.6 mm (H) and the beam flux was approximately 2.9×10^4 photons/s. This beam was introduced into the measurement chamber to perform grazing incidence measurements (Fig. 1a). An external field of 300 Oe was applied antiparallel to the beam direction to magnetize the Fe(001) film. In this arrangement, the π -polarized incident beam interacted with the four nuclear transitions of $\Delta m = \pm 1$. The Mössbauer absorption spectra were measured by collecting the totally reflected γ -rays from the sample surface at an incident angle of 0.1° with a reflectivity of approximately 80%. Each spectrum was obtained within a few hours of sample preparation. Such rapid measurements significantly reduced the residual gas absorption and oxidation on the Fe(001) surfaces.

Figure 1b presents the Mössbauer spectra of the N th probe layer samples ($N = 1$ to 4 and 7) recorded at 300 K. All samples showed magnetically split Mössbauer patterns. The spectra of the first, second, and third probe layer samples exhibited complex profiles composed of different magnetic components, i.e., small H_{int} (red lines, around 28 T), large H_{int} (blue lines, around 36 T), and bulk-like H_{int} (green lines, around 32 T).

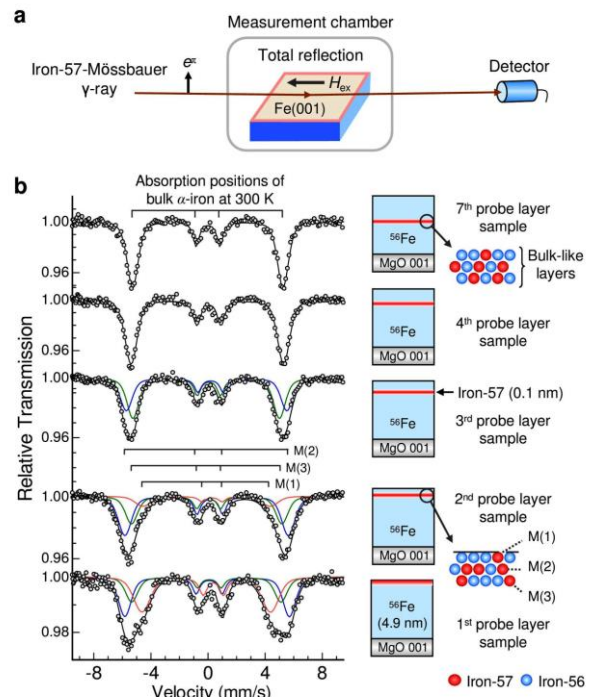


Figure 1. (a) Experimental setup. (b) Mössbauer spectra of the N th probe layer samples measured at 300 K. Black solid lines represent the fitted curves. Red, blue, and green lines represent the three different magnetic components. $M(i)$ represents the magnetic component assigned to the ^{57}Fe atoms located in the i th layer below the surface. H_{ex} is the magnetic field (300 Oe).

The ideal probe layer in the sample was surrounded by finely distributed ^{57}Fe atoms, which stemmed from the random deposition and surface diffusion of iron atoms during the growth process. Figure 1b (right) shows a conceptual diagram of the process. In this case, if the first, second, and third layers of the iron surface have a different H_{int} the spectra should exhibit a complex profile with multiple components. Based on the systematic behavior of the three components, the small H_{int} , large

H_{int} , and bulk-like H_{int} represent the intrinsic hyperfine fields for the first, second, and third layers from the surface, respectively. In contrast, the spectra of the fourth and seventh probe layer samples exhibited a single magnetic component with four absorption lines, even in the presence of finely distributed ^{57}Fe atoms. This is because the hyperfine fields of the neighboring layers at these depths are bulk-like, and the overlapping subspectra result in a simple absorption profile. The prominent subspectrum with the largest percent area in the N th probe layer sample was assigned to the spectrum characterizing the ^{57}Fe atoms located in the N th atomic layer from the surface.

The experimentally determined layer-by-layer H_{int} exhibited a marked decrease at the surface and an oscillatory decay toward the bulk value. Such a behavior was successfully reproduced by theoretical calculations (Fig. 2). This result

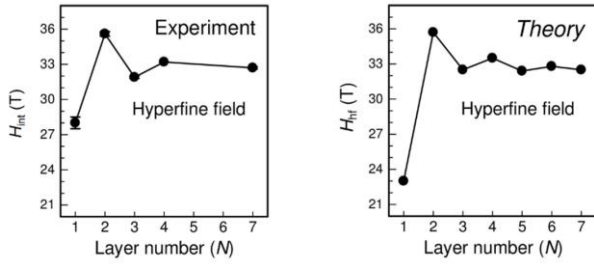


Figure 2. The experimental and theoretical layer-by-layer hyperfine magnetic fields.

provides the first experimental evidence for the magnetic Friedel oscillations, which penetrate several layers below the Fe(001) surface. Theoretically, the oscillatory decay of H_{int} should be strongly coupled with the Friedel oscillation of M_{Fe} , which is caused by the surface electronic structure with a large spin imbalance and d -band narrowing [1, 2, 3].

In summary, the surface magnetism of Fe(001) was studied in an atomic layer-by-layer manner by using the in situ ^{57}Fe probe layer method with a synchrotron Mössbauer source. The observed H_{int} exhibited a marked decrease at the surface and an oscillatory behavior with increasing depth in the individual upper four layers below the surface. In the future, the in situ ^{57}Fe probe layer method with a synchrotron Mössbauer source should facilitate additional studies on the surface and interface magnetism in advanced magnetic and spintronic materials and devices.

Acknowledgments

The authors thank Prof. K. Mibu, Prof. Y. Yamada, Dr. H. Naramoto, Dr. S. Entani, Dr. T. Inami, and Dr. Y. Katayama for their helpful discussions.

References

1. C. S. Wang and A. J. Freeman, PRB **24** (1981)4364.
2. S. Ohnishi et al: PRB **28** (1983) 6741.
3. T. Mitsui et al: PRL 125 (2020) 236806.

Theoretical Study of X-ray Magnetic Circularly Polarized Emission

Takuji Nomura¹ and Akihiro Koide²



¹ Condensed Matter Theory Group, ² Magnetism Research Group,
Synchrotron Radiation Research Center

Spectroscopic methods utilizing synchrotron radiation to analyze magnetic properties in materials have attracted much interest. One of the most widely used methods is x-ray magnetic circular dichroism (XMCD). XMCD is a kind of x-ray absorption spectroscopy. In XMCD, the incident absorbed x-ray is circularly polarized, carrying a finite angular momentum. When a circularly polarized x-ray is absorbed by an electron in a material, the electron is excited to an unoccupied state above the Fermi level (E_F) with changing its angular momentum, where the sum of the angular momenta of the electrons and absorbed x-ray is conserved. In ferromagnets, electrons are polarized in spin angular momentum. In other words, electron unoccupancy as well as electron occupancy differs between spin up and down states. This difference leads to the difference in the electron transition probability or equivalently absorption intensity, for right- or left-handed circularly polarized x-rays.

Recently, Inami succeeded in observing magnetic circularly polarized emissions (XMCPE) at the K edge in magnetized iron [1]. This provides a new magnetically-sensitive spectroscopic method utilizing synchrotron radiation. In Fig. 1, a typical process of XMCPE at the transition-metal K edge is illustrated. In XMCPE, an incident linearly polarized x-ray (i.e., carrying no angular momentum) is absorbed, promoting a $1s$ electron to a free conduction state and leaving a hole on the inner K -shell (as shown on the left side of Fig.1). At this stage, since the incident photon brings no angular momentum, the free electron takes the same spin angular momentum as in the $1s$ state before promoted. This means that the electron system still maintains the same total angular momentum. Subsequently one of the $2p$ electrons goes down to the unfilled $1s$ state, emitting a circularly polarized x-ray. Since the total angular momentum of the electron system and outgoing x-ray is conserved, the electron system must have a different angular momentum from that in the initial state. In other words, the electronic system loses an equal amount of angular momentum to that carried away by the circularly polarized outgoing photon. Thus, in the final state of XMCPE, the electron system will be in an excited state with a different angular momentum from that of the initial ground state, as in the final state of XMCD. In ferromagnets, such an excitation will occur with a different probability, depending on right- or left-handed x-ray emission. In fact, for magnetized iron, Inami observed a clear difference in emission spectra for the two helicity states of emitted x-rays [1]. Here we should note that in contrast to the XMCD technique that utilizes the difference in intensity between the two helicity states of *absorbed* x-rays, the XMCPE technique utilizes the difference between the two helicity states of *emitted* x-rays. Compared with XMCD, XMCPE has the following advantages: (i) the flipping ratio (i.e., the relative difference in intensity between the two helicity states of [absorbed or emitted] x-rays) is large. (ii) High bulk sensitivity can be achieved, by setting the incident

and emitted x-rays in the hard x-ray regime. Thus, XMCPE can be a powerful new tool to investigate magnetization distributions deep inside bulk ferromagnets.

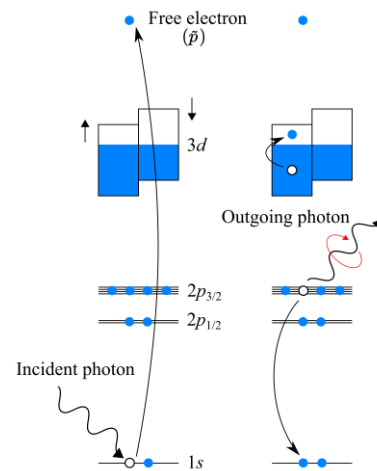


Fig. 1: Illustration of a typical XMCPE process. Initially, an incident photon of an incoming x-ray promotes a $1s$ electron to a free-electron state, leaving a core hole in the $1s$ level (on the left side). Subsequently, one of the $2p$ electrons fills the $1s$ hole and a circularly polarized x-ray photon is emitted (on the right side). Electron excitations in the $3d$ bands can also be induced by the $2p$ - $3d$ Coulomb interaction. The six $2p$ levels are split into $2p_{1/2}$ doublets (L_2) and $2p_{3/2}$ quartets (L_3) due to the spin-orbit coupling.

To our knowledge, any theoretical descriptions of XMCPE have been restricted so far to those based on atomic multiplet calculations. One of such analyses is given in [1]. However, it is widely known that such atomic calculations are insufficient for describing electron excitations in itinerant electron systems such as bulk iron, while it is appropriate for describing only electron transitions between strongly localized states. In this report, our new theoretical framework applicable to itinerant ferromagnets is explained, following [2].

In transition-metal ferromagnets, the d electrons near E_F dominantly contribute to the total magnetization. Therefore, first we performed a first-principles band structure calculation. To extract the electronic structure near E_F from the result, we constructed the so-called maximally localized Wannier functions, assuming the Fe- s , Fe- p and Fe- d characters (Here we should not confuse these Fe- s and Fe- p states with the inner-shell $1s$ and $2p$ states). This produces a 9-orbital tight-binding model. Here we should note that the Fe- $3d$ states form dispersive broad bands (with about 10 eV bandwidth), for which isolated-atom descriptions are invalid. Including the onsite Coulomb

interaction (U , U' , and J) among the five Fe-3d orbitals, we have a Hubbard-type model with a realistic electronic band structure. To determine the ferromagnetic ground state, the Hartree-Fock (mean-field) approximation is applied to this model. The calculated magnetic moment is $2.0 \mu_B$ per Fe site for $U = 2.2$ eV, $U' = 1.32$ eV and $J = 0.44$ eV. For the inner-shell 1s and 2p states, we can take completely flat bands, since they still take the isolated atomic nature even in the solid state. In the $K\alpha$ XMCPPE, the Coulomb interaction V_{2p-3d} between the 2p and 3d states plays an essential role, because the 2p states are affected by the 3d spin polarization through V_{2p-3d} . If we take no account of the 2p-state polarization through V_{2p-3d} , we have no difference in the 2p-1s emission intensity between right- and left-handed circularly polarized x-rays. We control V_{2p-3d} , setting the so-called Slater-Condon parameters F^n ($n = 0, 2$) and G^n ($n = 1, 3$). To calculate x-ray emission intensities, we used a quantum-field-theoretical method based on the Keldysh Green's functions for non-equilibrium processes. As a consequence, we derived an analytic formula for XMCPPE intensity (See [2] for mathematical details). According to the result, the XMCPPE intensity is expressed by a sum of two contributions: $W_{R/L} = \bar{W}_{R/L} + \delta W_{R/L}$. $\bar{W}_{R/L}$ originates from the $2p \rightarrow 1s$ relaxation processes leaving no excitations on the 3d bands in the final state, where R/L denotes the emission of right-handed (R) or left-handed (L) circularly polarized x-rays. $\delta W_{R/L}$ is a many-body correction due to excitations where an electron-hole pair remains on the broad 3d bands in the final state. $\bar{W}_{R/L}$ can be effectively calculated even within the atomic descriptions, because excitations on the 3d states are not included in any case. On the other hand, as we shall see below, $\delta W_{R/L}$ substantially yields a broad weight as a function of emitted x-ray energy, reflecting the broadness of the Fe-3d bands. Such a broad $\delta W_{R/L}$ weight should be treated by itinerant electron bands, not by discrete atomic energy levels. Finally, we should note that the subtraction spectrum $W_R - W_L$ vanishes completely for paramagnets but remains finite for magnetized ferromagnets.

Calculated XMCPPE spectra for metallic iron are displayed in Figs. 2 and 3. In Fig. 2, the emission spectra $\bar{W}_{R/L}$ and their subtraction $\bar{W}_R - \bar{W}_L$ *neglecting* the excitations on the Fe-3d bands are compared with experimental data. We can see a significant deviation on the lower-energy side of each of the L_2 and L_3 emission peaks. In contrast, in Fig. 3, the emission spectra $W_{R/L}$ and their subtraction $W_R - W_L$ *including* the excitations on the Fe-3d bands are compared with experimental data. The tail-like spectral weight on the low-energy side can be well reproduced by the theoretical calculation. This comparison clearly indicates that the electron excitations on the Fe-3d bands snatch a significant amount of energy from the emitted x-ray. Thus, we can interpret that the tail-like weight on the low-energy side captures the broad excitations of itinerant Fe-3d electrons, whose broadness is of the order of the Fe-3d bandwidth.

In conclusion, we give possible perspectives to advance: (i) our framework can be applied further to a wide variety of ferromagnets. (ii) In our framework, we adopted a perturbative approach taking only the lowest-order contributions in V_{2p-3d} (Born approximation). One possible future research direction is to investigate the effects of higher-order terms including multiple electron-hole excitations and spin-wave (magnon) collective modes, although this will require more complicated analytical and much heavier numerical computations.

Acknowledgments

The authors are grateful to Dr. Toshiya Inami for close collaborations and discussions.

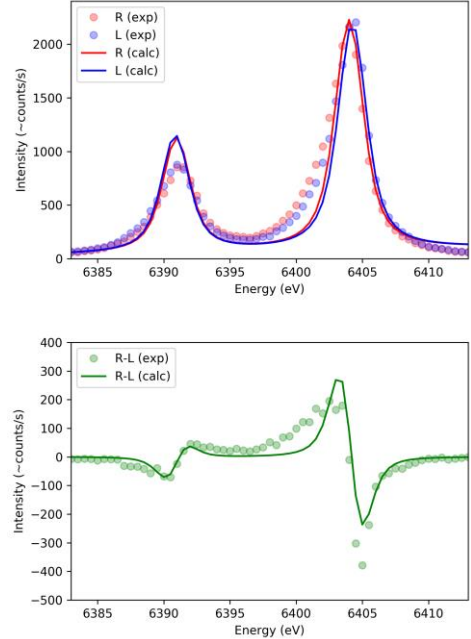


Fig. 2: Calculated curves of XMCPPE spectra $\bar{W}_{R/L}$ and the subtraction $\bar{W}_R - \bar{W}_L$ as a function of emitted x-ray energy for right- (R) and left-handed (L) circularly polarizations are compared with experimental plots. Here, the excitations on the Fe-3d bands are *neglected*.

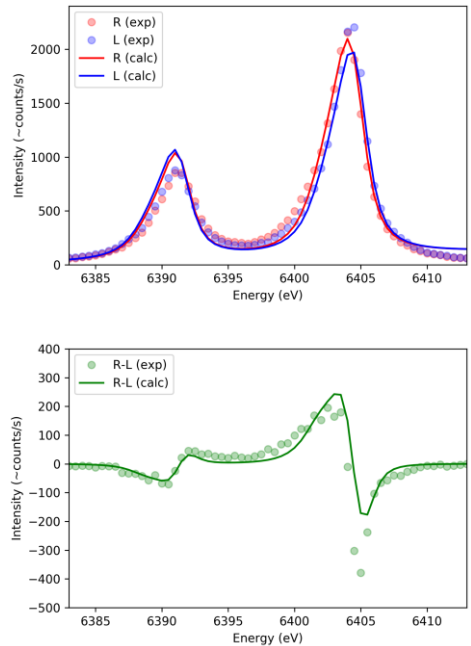
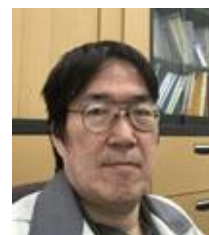


Fig. 3: Calculated curves of XMCPPE spectra $W_{R/L}$ and the subtraction $W_R - W_L$ as a function of emitted x-ray energy for right- (R) and left-handed (L) circularly polarizations are compared with experimental plots. Here, the excitations on the Fe-3d bands are *included*.

References

- [1] T. Inami, Phys. Rev. Lett. **119**, 1337203 (2017).
- [2] A. Koide, T. Nomura, and T. Inami, Phys. Rev. B **102**, 224425 (2020).

Research Activities of the Institute of Quantum Life Science at KPSI



N. Shikazono

Institute of Quantum Life Sciences

The field of quantum life science has emerged to explore the new frontiers in biology from the perspective of the quantum domain to describe dynamics and functions of cells and organisms. The Institute of Quantum Life Science at the National Institutes for Quantum Science and Technology (QST) was established in April 2019 to pioneer a new field in life sciences. Investigations at the Institute of Quantum Life Science are expected to follow two approaches: determining whether quantum mechanics plays an essential role in biological systems, and applying quantum science and its technologies to measure physical and chemical parameters, such as temperature, pressure, and pH, at nanoscales inside cells, or for measurements of the structure and dynamics of biomolecules at an unprecedented minute level. Using the above two approaches, the goal of the Institute of Quantum Life Science is to discover the essential principles of life and to apply the knowledge that is developed during the course of investigation to medical sciences and social activities (Fig. 1). The field of quantum life science is envisaged to produce unanticipated discoveries that will expose the existence of quantum phenomena in nature, ultimately leading to their exploitation in novel knowledge and technologies that benefit society. At the Kansai Photon Science Institute (KPSI), three research groups in the Institute of Quantum Life Science are carrying out their research by conducting experiments and computer simulations (Fig. 1).

The Molecular Modeling and Simulation Group is aiming to understand the *in vivo* function of biomolecules at the atomic level. The group uses computer simulations and bioinformatics together with results obtained by experiments, such as crystallographic and scattering data obtained by various types of radiation (x-rays, neutrons, and electrons) and cryo-electron microscopy. The main research target is to determine how the dynamics of protein/DNA/RNA complexes relate to essential cellular functions, such as transcription, translation, replication, and repair. One of the focuses of the group is to determine whether current simulations quantitatively predict the stability of ribonucleic acids (RNAs). This research group carried out a free-energy perturbation simulation of RNAs containing inosine, a modified ribonucleic base, to derive RNA nearest-neighbor parameters. Surprisingly, a parameter set obtained from only thirty simulations was able to predict the difference in free energies of the various RNA duplexes with a low mean unbiased error, which is a level of accuracy comparable to that obtained from twenty-five experiments. They found that the error could be further lowered by combining the simulation-derived and experimentally measured free-energy differences. The research group demonstrated that their simulation is very useful for deriving nearest neighbor parameters of RNAs with various types of modified base [1]. The results are described in the associated report. The group has also been working on the dynamic structure of nucleosomes. A nucleosome is the fundamental structural unit of chromatin and is composed of histone proteins wrapped in DNA. Generally, torsional stress has a significant impact on the

structure and stability of the nucleosome. For instance, RNA polymerase imposes torsional stress on the DNA in chromatin and unwraps the DNA from the nucleosome to facilitate the access to the genetic information encoded in the DNA. To understand how such torsional stress affects the stability of the nucleosome, the research group has simulated the unwrapping of the nucleosomal DNA under a positive or negative torsional stress. The free energies for unwrapping the DNA indicated that a positive stress, which overtwists the DNA, promotes asymmetric unwrapping of the DNA, while a negative stress, which undertwists the DNA, does not accelerate unwrapping. Under a positive stress, the DNA becomes straightened and rigid, which facilitates a large-scale asymmetric unwrapping of the DNA. One end of the DNA is disconnected from the histones while the other end remains stable wrapped around the histones. Under a negative stress, the DNA is more easily bent and becomes more flexible, which facilitates the binding of the histones to the DNA. The results indicate that the stability of individual nucleosomes in the chromatin is changed by a torsional stress, thereby enabling access of regulatory proteins to the DNA to maintain gene expression without large conformational changes of chromatin [2]. The results are described in the associated report.

The main goal of the DNA Damage Chemistry Group is to clarify the nature of DNA damage induced by various agents, especially damage from ionizing radiation. The group aims to utilize new experimental techniques that can unveil the structure of DNA damage as well as the recognition of DNA damage by repair enzymes at nanometer scales. The focus of the group is currently on “clustered DNA damage”, in which two or more DNA lesions are located within one to two helical turns of DNA (within several nanometers along the DNA). Clustered DNA damage is considered to be challenging to repair, and thus, a critical type of damage induced by ionizing radiation. However, its presence and microstructure has remained elusive, as few experimental methods were able to obtain data on the spatial distribution of DNA lesions. This research group has established an approach for measuring the level of localization of DNA damage by directly visualizing the damage. Atomic force microscopy (AFM) has a resolution at the nanometer/subnanometer scale, and thus DNA can be directly visualized. The research group has labeled DNA damage (abasic sites) by attaching aldehyde reactive probes with biotin, and then attaching streptavidin to the biotin. The large molecular size enables the detection of streptavidin by AFM. Abasic sites were directly induced, or further revealed by removing the damaged base by DNA glycosylases, after irradiation. The complex nature of the clustered DNA damage was visualized for the first time by this method. The research group has further developed a promising method to detect clustered DNA damage, using fluorescence anisotropy measurements based on Förster resonance energy transfer (FRET). In this method, aldehyde/ketone moieties such as at abasic sites in irradiated DNA are labeled by aminooxyl fluorophores. Fluorescence

Institute of Quantum Life Science

Using cutting-edge quantum technologies and advanced computer simulations, the Institute aims to contribute (1) to the elucidation of the basic principles of life, and in longer term, (2) to the benefit for the everyday life of the society.

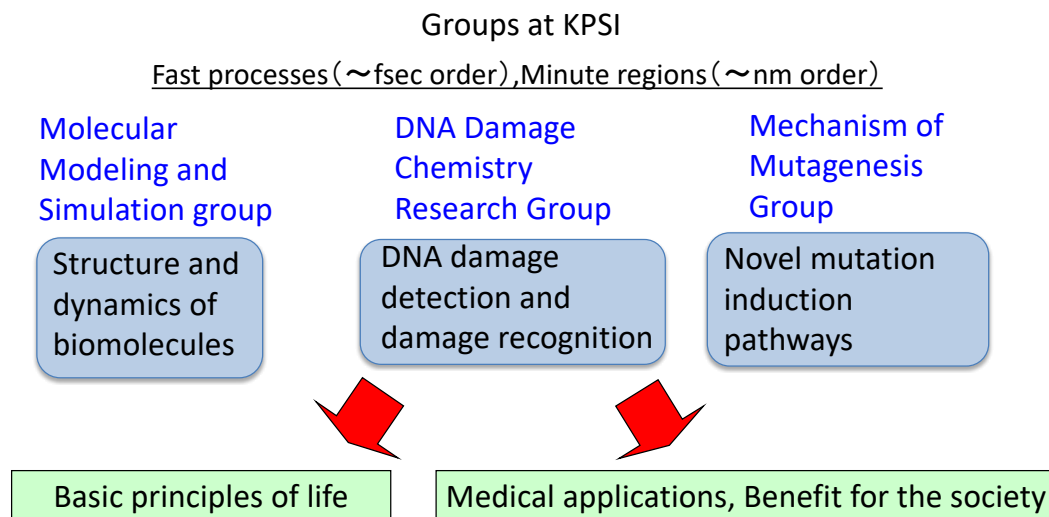


Figure 1.

anisotropy enabled (a) the estimation of the apparent base-pair separations between lesions in a cluster produced by an ion track, and (b) revealed that the yield of clustered abasic sites increased with increasing linear energy transfer of the radiation. The results demonstrate that fluorescence anisotropy analysis has the potential to be used to discover the qualitative and the quantitative differences of clusters produced not only by ionizing radiation but also by other DNA damaging agents [3]. Below in the associated report, a detailed description is given.

A goal of the Mechanism of Mutagenesis Group is to elucidate the underlying mechanisms of the induction of mutations, which are highly relevant to carcinogenesis and the evolution of life. One aspect of the research of this group focuses on the events at the very early stages (around a femtosecond to picosecond) within a space in the scale of nanometers after energy transfer from ionizing radiation, especially from ion particles. Using Monte-Carlo simulations, the research group has demonstrated that, when water is exposed to densely ionizing ion particles, some of the secondary electrons ejected from the water molecules are trapped within the electric potential created by the ionized water molecules. This result leads to the realization that the radial dose near the track of a densely ionizing ion particle is much higher than previously understood. This highly localized energy deposition is considered to produce a high yield of clustered DNA damage, and thus have important implications for the drastic effect of ion particles on cells. Another research interest of the group is the molecular mechanisms of mutagenesis. One of the unique features of the mutation frequency of bi-stranded clustered DNA damage is that its mutation frequency is significantly higher than the mutation frequencies of the isolated lesions, even when the cell lacks the ability to repair isolated lesions. This suggests that there is a pathway for mutagenesis in addition to the persistence of the mutagenic lesion. For further insight into the mutagenic process of clustered DNA damage sites, the research group used a plasmid-based assay in *Escherichia coli* cells. Their findings revealed that the strand containing a mutagenic lesion within a bi-stranded clustered DNA damage site

is preferentially used as a DNA template. The length of the region of strand preference was found to be determined by DNA polymerase I. These results suggest the presence of an unknown, strand synthesis process during the mutagenesis of clustered DNA damage [4].

Quantum life science is related to the interactions between dynamical phenomena at extremely short time scales and minute length scales, that is, from atto to femtosecond energy transfer processes at the (sub)nanometer scale. Over the long term, the field of quantum life science is expected to produce unparalleled discoveries based on the significance of quantum phenomena in biological systems. To achieve such goals, the research of the three groups of the Institute of Quantum Life Sciences at the KPSI is ongoing.

References

1. Sakuraba S, Iwakiri J, Hamada M, Kameda T, Tsuji G, Kimura Y, Abe H, Asai K. Free-Energy Calculation of Ribonucleic Inosines and Its Application to Nearest-Neighbor Parameters. *J. Chem. Theory. Comput.* 16, 5923-5935 (2020)
2. Ishida, H. and Kono, H. Torsional stress can regulate the unwrapping of the outer superhelical turn of nucleosomal DNA. *Proc. Natl. Acad. Sci. USA.* 118, e2020452118 (2021).
3. Akamatsu K, Shikazono N, Saito T. Fluorescence anisotropy study of radiation-induced DNA damage clustering based on FRET. *Anal Bioanal Chem.* 413, 1185-1192 (2021).
4. Shikazono N, Akamatsu K. Strand with mutagenic lesion is preferentially used as a template in the region of a bi-stranded clustered DNA damage site in *Escherichia coli*. *Sci. Rep.* 10, 9737 (2020).

Predicting the stability of modified RNA duplexes: the inosine-cytidine pair

Shun Sakuraba

Molecular Simulation Group, Institute of Quantum Life Sciences



Ribonucleic acids (RNAs) are one of the essential molecules in life. Unlike deoxyribonucleic acids (DNAs), which typically form double-strand helices by making Watson-Crick pairs to complementary DNA chains in living cells, most RNA molecules are single-chained. The RNA often creates Watson-Crick pairs within a single chain and forms various structures. In RNA biology, the topological information of RNA-RNA binding is referred to as the “secondary structure”. The secondary structure is strongly tied to the biological functions of RNA, and thus, the prediction of the RNA secondary structure from its primary sequence (consisting of A, C, G, or U representing RNA bases) is an important task [1]. In the prediction, the change in stability (or free-energy gains/losses) of the Watson-Crick pair formation must be assessed. Current RNA biology relies on the *nearest-neighbor parameter* [2] that describes the free energy change upon a Watson-Crick pair formation of canonical (A, C, G, or U) RNA bases.

Recent developments in RNA sequencing technology have revealed that, in addition to canonical RNA bases, several *modified bases* are used in living cells. Furthermore, these RNAs with modified bases, or *modified RNAs*, plays an important role in complex biological functions; for example, a loss-of-function mutation in an adenine-to-inosine converter enzyme leads to an epilepsy in mice [3]. Often, the modification also incites the rearrangement in the RNA secondary structure and its function. However, the change in stability of Watson-Crick pairs with base modification is largely unknown. Deriving nearest-neighbor parameters requires tens of UV-melting experiments [2], and synthesizing the modified RNAs for that many experiments is costly.

This challenge was addressed with the help of molecular dynamics (MD) simulations [4]. By performing specially designed MD simulations, the free-energy difference of the RNA-RNA binding can be calculated. In MD simulations, actually synthesizing the modified RNAs is not required; new bases can

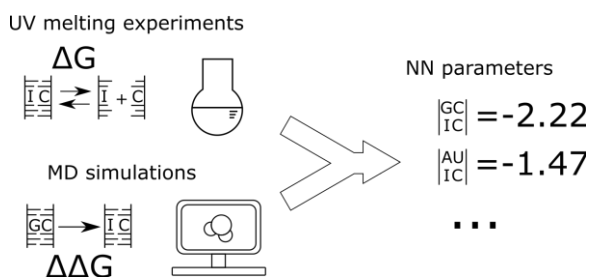


Figure 1. Schematic diagram of our parameter deriving scheme. A small number of experiments (eight synthesized sequences) and multiple MD simulations (corresponding to thirty sequences) were combined to obtain the new nearest-neighbor parameter. Adapted with permission from [4]. Copyright 2020 American Chemical Society.

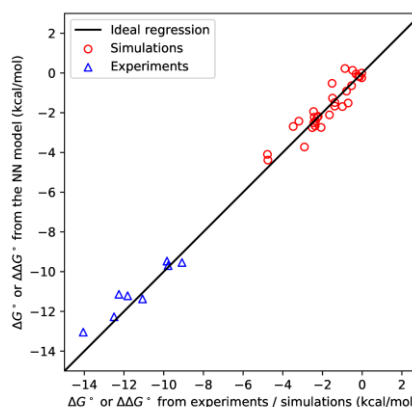


Figure 2. Experimentally and computationally obtained change in stability (measured by free energies) versus the predicted stability. Reprinted with permission from [4]. Copyright 2020 American Chemical Society.

be modeled with just a mouse-and-keyboard. To derive the nearest neighbor parameters of modified RNAs efficiently, we have developed a computational scheme to calculate the free-energy difference [5]. Additionally, we designed a new scheme to combine known experimental data with computational data (Fig. 1) based on a simple linear regression with a Gaussian error model [6].

The developed method was applied to the nearest-neighbor parameter derivation for RNAs containing inosine-cytidine pairs [7]. First, the consistency between the experiments (eight RNA duplexes were synthesized and measured), the simulation, and the newly derived parameters was tested. Figure 2 shows the observed/predicted change in stability (free-energy difference) obtained by the experiments/simulations versus the final stability prediction from the newly derived nearest-neighbor parameters. It can be clearly seen that the prediction can reproduce the experimental and computational free-energy difference. To test the possibility that the current parameter is overfitting the experimental values, a jackknife analysis was performed. I.e., one sample was removed from the dataset and the parameters used in the prediction regenerated, and the stability of the removed sample was then predicted. Figure 3 presents the experimental value and the predicted value, demonstrating that the experimental values can be reproduced with the proposed method.

The performance of the newly designed parameter was further evaluated with recently published experimental measurements of inosine-cytidine pairs containing RNAs. Table 1 shows the prediction error of the experimentally measured change in stability. The prediction error (measured by the mean unbiased error, MUE) was as low as 0.60 kcal/mol. In comparison, for the inosine-cytidine pair parameter, the MUE estimated from the fully experimentally derived (using twenty-five sequences)

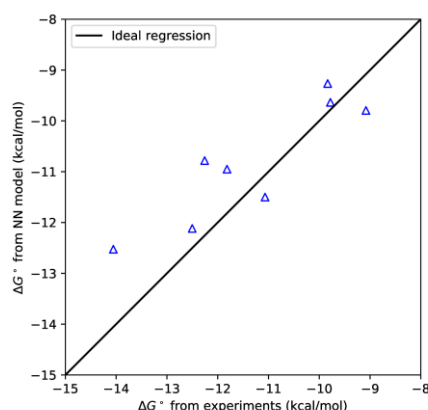


Figure 3. Experimentally obtained change in stability (measured by free energies) versus the predicted stability. Prediction was performed without using the data to be predicted (the jackknife analysis). Reprinted with permission from [4]. Copyright 2020 American Chemical Society.

	8 exps + 30 sims (this work)	25 exps, jackknife
MUE (kcal/mol)	0.60	0.75

Table 1. The accuracy estimation of the newly derived parameter. “Exps” represents the number of experimentally synthesized and measured RNA duplexes to obtain the parameter set. “Sims” represents the number of MD simulations performed to predict the RNA free-energy change. The lower the MUE the better.

parameter with the jackknife analysis was 0.75 kcal/mol. This result indicates that the newly derived parameter using only eight synthesized sequences performs at least as well as the fully experimentally derived parameter from experiments using twenty-five synthesized sequences.

In summary, a methodology was developed to derive the nearest-neighbor parameter, which describes the stability of RNA structures, for the modified bases. The methodology combines MD simulations with experimental measurements to obtain accurate nearest-neighbor parameters. The newly derived parameters were at least as accurate as the experimentally determined parameters.

Collaborators

Junichi Iwakiri,¹ Michiaki Hamada,² Tomoshi Kameda,^{3,4}

Genichiro Tsuji,^{5,6} Yasuaki Kimura,⁵ Hiroshi Abe,⁵ and Kiyoshi Asai.^{1,4}

1. Graduate School of Frontier Sciences, The University of Tokyo, Japan; 2 Faculty of Science and Engineering, Waseda University, Japan; 3 Computational Bio Big-Data Open Innovation Laboratory (CBBDOIL), National Institute of Advanced Industrial Science and Technology (AIST), Japan; 4 Artificial Intelligence Research Center (AIRC), National Institute of Advanced Industrial Science and Technology (AIST), Japan; 5 Department of Chemistry, Graduate School of Science, Nagoya University, Japan; 6 Division of Organic Chemistry, National Institute of Health Sciences, Japan.

Acknowledgments

The computations were performed using computing resources at ACCMS, Kyoto University, Japan, and at the Research Center for Computational Science, Okazaki, Japan. This work was supported by JSPS KAKENHI Grants-in-Aid for Scientific Research 16H02484 to SS, MH, TK, HA, and KA, 16K17778 to SS, and 16K16143 to JI, and by MEXT Grants-in-Aid for Scientific Research on Innovative Areas 19H05410 to SS and 16H06279 to KA.

References

- Seetin, M. G. and Mathews, D. H. RNA Structure Prediction: An Overview of Methods. *Methods Mol Biol*, **905**, 99-122 (2012).
- Xia, T. et al. Thermodynamic Parameters for an Expanded Nearest-Neighbor Model for Formation of RNA Duplexes with Watson-Crick Base Pairs. *Biochemistry*, **37** (42), 14719-14735 (1998).
- Brusa, R. et al. Early-onset epilepsy and postnatal lethality associated with an editing-deficient GluR-B allele in mice. *Science* **270**, 1677-1680 (1995).
- Sakuraba, S. et al., Free-energy calculation of ribonucleic inosines and its application to nearest-neighbor parameters. *J Chem Theory Comput*, **16** (9), 5923-5935 (2020).
- Sakuraba, S. et al., Predicting RNA duplex dimerization free-energy changes upon mutations using molecular dynamics simulations. *J Phys Chem Lett*, **6** (21), 4348-4351 (2015).
- Nishida, S. et al., Estimating energy parameters for RNA secondary structure predictions using both experimental and computational data. *IEEE/ACM Trans Comput Biol Bioinform*, **16** (5), 1645-1655 (2018).
- Wright, D. J. et al., Stability of RNA duplexes containing inosine-cytosine pairs. *Nucl Acid Res*, **46** (22), 12099-12108 (2018).

Unwrapping of two outer half superhelical turns of nucleosomal DNA under torsional stress

Hisashi Ishida



Molecular Modeling and Simulation Group, Institute for Quantum Life Science

The genome DNA of eukaryotes is compactly stored in a nucleus and folded into chromatin, a higher order structure, to protect the DNA from being damaged by radiation, etc. However, decompaction of the chromatin structure is also required for the control of gene regulation in the cellular processes for transcription, replication, repair, and recombination. The nucleosome is the fundamental structural unit of chromatin and is composed of histone proteins and DNA. Its crystal structure reveals that within the nucleosome, 146 or 147 bps of DNA wrap 1.75 times around an octameric histone core. Although the nucleosome is stable in physiological conditions, thermal fluctuations cause spontaneous partial unwrapping of nucleosomal DNA from the histone core. Experiments have found dynamic motion between an open state with partially unwrapped DNA and the closed state with fully wrapped DNA, which is often referred to as the breathing motion of the nucleosome.

In addition to the spontaneous unwrapping of outer turns of DNA, some DNA-binding proteins such as transcribing RNA polymerase (RNAP) and chromatin remodelers actively apply forces to unwrap or rewrap nucleosomal DNA. During transcription, RNAP moves along the DNA helix and generates positive and negative stresses on the DNA in front and behind the RNAP, respectively. Consequently, DNA downstream and upstream of the polymerization site are overwound (either overtwisted or positively supercoiled) and underwound (either undertwisted or negatively supercoiled), respectively. As nucleosome core particles prefer to bind negatively supercoiled DNA, overwound DNA ahead of the RNAP would destabilize the DNA-histone or histone-histone interactions in the nucleosome, and underwound DNA behind the RNAP would promote the reassembly of nucleosomes.

However, the mechanism for DNA outer turn unwrapping and rewrapping is not well understood at the atomic level. In order to understand how the torsional stress on the outer turn of DNA affects the stability of the nucleosome, all-atom molecular dynamics simulations of nucleosome under torsional stress were performed (1). Previously, the unwrapping of two half superhelical turns of nucleosomal DNA from either end of the DNA (hereinafter referred to as “two outer half turns of DNA”) was investigated without torsional stress (2-5). In the present study, the free energy under torsional stress will provide further insight into understanding the unwrapping of the outer turn of DNA.

To understand how the torsional stress affects the stability of the nucleosome, the unwrapping of two half superhelical turns of nucleosomal DNA from either end of the DNA was examined under torsional stress with all-atom molecular dynamics simulations (Fig 1).

The free energy for unwrapping the DNA was calculated against the DNA end-to-end distance d (Fig. 2(a)). The free energies had a global minimum free energy of 0.0 kcal/mol when $d = 63, 69,$ and 67 \AA under positive, negative, and no stress

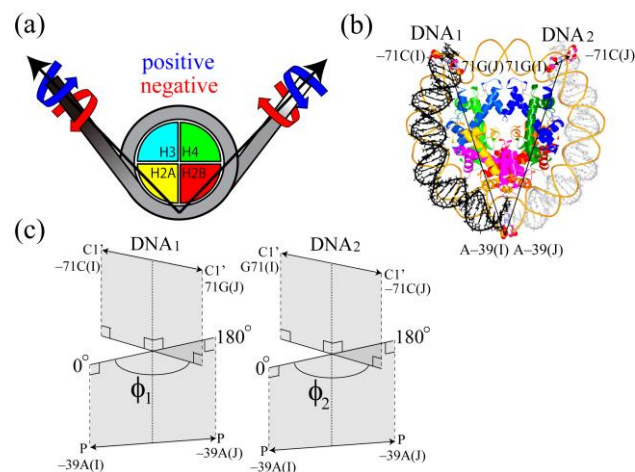


Fig. 1 The nucleosome system for simulations under torsional stress. (a) Schematic representation of the nucleosome system under a torsional stress, (b) the initial structure of the nucleosome is shown in tube model, and (c) the definition of the torsional angles.

conditions, respectively. Up to $d = 145 \text{ \AA}$, the free energy under positive stress was larger than under negative and no stress conditions, indicating that more free energy is required to extend the distance between two DNA ends d under positive stress. In particular, the differences in the free energy up to that distance among the three torsional conditions results from the sharper rise of the free energy from a d of approximately 63 to 76 \AA under positive stress as compared with the rise from a d of approximately 70 to 85 \AA under negative and no stress conditions, where the DNA started to dissociate from the H3 α N-helix. This indicates that the interaction between the DNA and the H3 α N-helix was stronger under the positive stress. A relatively moderate increase in the free energy followed the sharp rise. The gradient of the free energy under the positive stress was nearly constant up to $d = 170 \text{ \AA}$ while those under the negative and no stress conditions gradually increased with d . Eventually, the free energies became larger than under the positive stress at a d of approximately 150 \AA . When two outer half turns of DNA were fully unwrapped, the free energies were 13.5 kcal/mol at $d = 220 \text{ \AA}$, 19.5 kcal/mol at $d = 214 \text{ \AA}$, and 17.0 kcal/mol at $d = 214 \text{ \AA}$ under positive, negative and no stress conditions, respectively. After those distances, the free energies rapidly increased as the DNA started to stretch.

To interpret the unwrapping process structurally, the perspective of the free energy as a function of the total number of unwrapped base pairs (hereafter referred to as bp_{total}) (Fig. 2(b)) was changed. The nucleosome under positive, negative, and no stress conditions had a global free energy minimum of 0.0 kcal/mol at $bp_{total} = 0$. In all cases, the free energies for positive, negative, and no stress conditions reached 12.0, 19.3,

and 15.2 kcal/mol at a bp_{total} of approximately 52, respectively, when the unwrapping of two outer half turns of DNA was completed. During the unwrapping, distinctive increases in the free energy were observed at $bp_{total} = 0, \sim 13, 26, 39,$ and 52 for the three cases. A remarkably sharp increase in free energy was observed at $bp_{total} = 26$ under negative and no stress conditions but not under the positive stress.

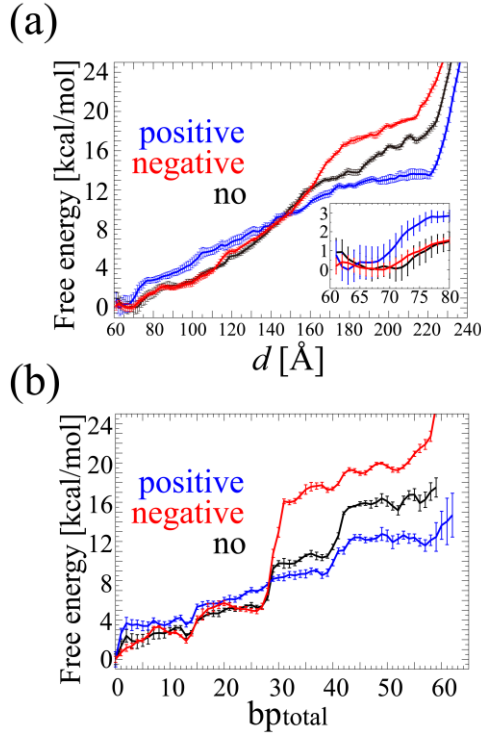


Fig. 2 Free energies for unwrapping the DNA against (a) d and (b) bp_{total} under positive (blue), negative (red), and no (black) torsional stress.

A model is proposed for the small- and large-scale asymmetric unwrapping of nucleosomal DNA as follows (Fig. 3).

First, the positive torsional stress overtwists the DNA, while the negative torsional stress undertwists the DNA. Second, the minor groove of the DNA at $SHL = \pm 6.5$ rotates and further strengthens the interaction with the H3 αN -helix under positive stress, which stabilizes the nucleosome and suppresses the transition from $sAS1$ to $S2$. Third, the change in the bendability and flexibility of the DNA influences the free energy for the DNA unwrapping. Overtwisted DNA under positive stress is straightened. The straightened DNA would increase the bending energy if the DNA retained the bent form to maintain its contact with H2A-H2B. This high bending energy in the DNA would facilitate the unwrapping of the DNA to relax the bent form of the DNA from $sAS1$ to $IAS2$. In contrast, the DNA under a negative stress is more bendable and would require less internal bending energy to wrap the DNA than under a positive stress. Consequently, it is concluded that the torsional stress has a significant impact on the affinity of the DNA and the octamer through the inherent nature of the DNA, and can change the accessibility of regulatory proteins. The present results suggest that DNA accessibility in the chromatin can be regulated by enhancing or suppressing asymmetric unwrapping without a large extension of the DNA through the torsional stress generated by proteins such as RNAP and chromatin remodeling complexes, which may explain why genes in condensed chromatin states can be expressed.

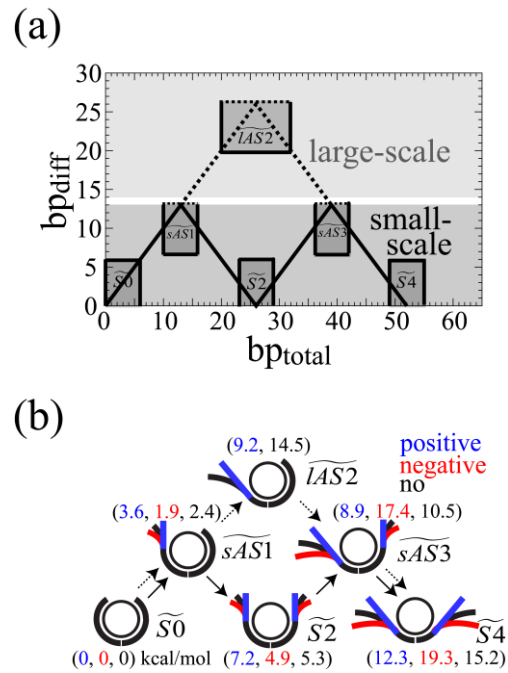


Fig. 3 Schematic representation of the model of the transitional paths for the unwrapping of two outer half turns of DNA under a torsional stress. (a) Definition of the six states: $S0$, $sAS1$, $S2$, $IAS2$, $sAS3$, and $S4$. (b) The unwrapping of two outer half turns of DNA under positive, negative, and no stress conditions is schematically shown in blue, red, and black, respectively. The transitional states are labeled as $S0$, $sAS1$, $S2$, $IAS2$, $sAS3$, and $S4$.

Acknowledgements

This work was supported by the Ministry of Education, Culture, Sports, Science, and Technology (MEXT) of Japan as "Priority Issue on Post-K computer" (Building Innovative Drug Discovery Infrastructure Through Functional Control of Biomolecular Systems) (Project ID: hp180191 and hp190171), "Program for Promoting Researches on the Supercomputer Fugaku" (Biomolecular Dynamics in a Living Cell) (hp200135), the HPCI system provided by Kyoto University (Project ID: hp180027, hp190007, and hp200029), and JSPS KAKENHI (18K06173 to HI and JP18H05534 to HK).

References

1. H. Kono, *PLOS ONE* (2015) 10:e0120635
2. J. Ikebe and H. Kono, *PLOS Comput. Biol.* (2016) 12:e1004788
3. Z. Li and H. Kono, *Sci. Rep.* (2016) 6:31437
4. H. Kono, S. Sakuraba S and H. Ishida, *PLOS Comput. Biol.* (2018) 14:e1006024
5. H. Ishida and H. Kono, *Proc. Natl. Acad. Sci. USA* (2021) 118, e2020452118. DOI: 10.1073/pnas.2020452118

Fluorescence anisotropy of radiation-induced DNA damage clustering based on FRET

Ken Akamatsu



DNA Damage Chemistry Research Group, Institute for Quantum Life Science

A clustered DNA damage site (cluster), in which there are two or more lesions within a few helical turns, is believed to be a key factor in determining the fate of a living cell exposed to a DNA damaging agent such as ionizing radiation. However, the structural details of clusters, such as the number of included lesions and their proximity, are unknown. A method is developed here to characterize clusters by fluorescence anisotropy measurements based on Förster resonance energy transfer (homo-FRET) (Fig. 1).

FRET has been used in molecular and cell biology to investigate the interaction between biomolecules as a “nanometer ruler”. It is also applied to visualize clusters in living cells. There are generally two categories of FRET: hetero-FRET and homo-FRET. Hetero- and homo-FRET can evaluate the energy transfer

phenomena between structurally different molecules (a “donor” – “acceptor” ($D-A$) pair) and same dye molecules, respectively.

We previously reported that the hetero-FRET method could estimate the localization of abasic sites (APs) by fluorescence spectroscopy of a labeled plasmid sample solution [1,2]. However, the sensitivity is insufficient, in principle, mainly because all the clustered APs cannot be labeled with a $D-A$ pair (i.e., a clustered AP labeled with a $D-D$ or $A-A$ pair is not detected as a cluster). Homo-FRET was attempted to compensate for this disadvantage [3], as the homo-FRET method is better suited than hetero-FRET due to its sensitivity and simple experimental protocol. However, the efficiency of this method must be estimated by fluorescence anisotropy as the fluorescence intensities with and without FRET for a given emission wavelength are equal. Here, the homo-FRET method is applied to estimate the AP localization in a plasmid DNA irradiated with carbon, helium ion beams, and ^{60}Co γ -rays in the solid state.

Figure 2A shows the observed fluorescence anisotropy of the irradiated DNA in the solid state as a function of the AP average density in comparison with that of the baseline heat-treated DNA with randomly distributed APs. The observed fluorescence anisotropy (r_{obs}) generally decreases with (i) increasing AP density (λ_{AP}) and (ii) increasing linear energy transfer (LET). The decrease due to (i) results from a “sequentially-produced” cluster due to overlapping two or more radiation tracks, whereas that from (ii) is caused by increasingly close AP-AP pairs accompanied by an increasing local dose of a radiation track. In addition, it is surprising that the degree of localization for ^{60}Co γ -rays is higher than for a random distribution (bold line), implying that low-energy electrons likely induces the clusters. Another possible reason for the difference may be the difference in the chemical structure of damaged sites such as an AP. Due to the heat incubation, DNA is known to be depurinated by hydrolysis to produce a typical AP, with an aldehyde moiety at C1' of the sugar. In contrast, irradiation of the “dry” DNA sample would produce a variety of electrophilic carbonyl groups that are reactive with an aminooxyl fluorescent dye used as well as the typical AP.

The anisotropy can be converted into the FRET efficiency (Fig. 2B) and apparent base separation i_{ap} (Fig. 2C). The y -intercept of each curve can elucidate the cluster formation produced by a single radiation track. However, obtaining data near the y -intercept is difficult due to the trace amounts of AP labeled with the fluorophore (i.e., $\lambda_{\text{AP}} \sim 0$). The apparent base separation i_{ap} corresponding to each lowest dose is 21.1, 19.4, and 18.7 bp, respectively. Hence, the value of the apparent base

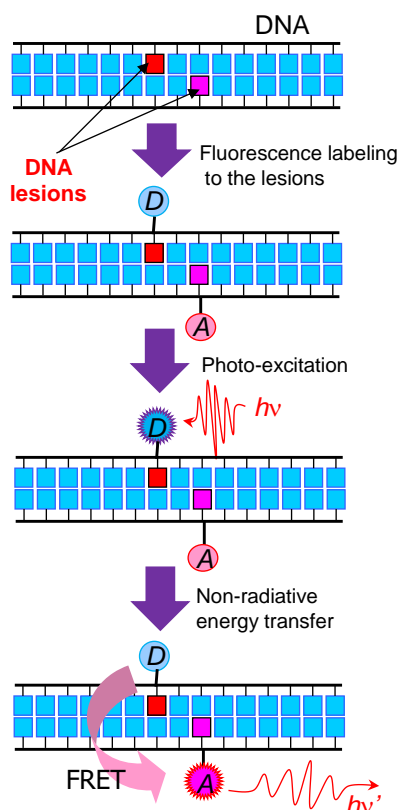


Fig. 1. Strategy for estimating the localization of DNA lesions using FRET. D and A are “donor” and “acceptor” fluorescent probes, respectively. When D and A are the same, the FRET is referred to as “homo-FRET”. When D and A are different, it is referred to as “hetero-FRET”.

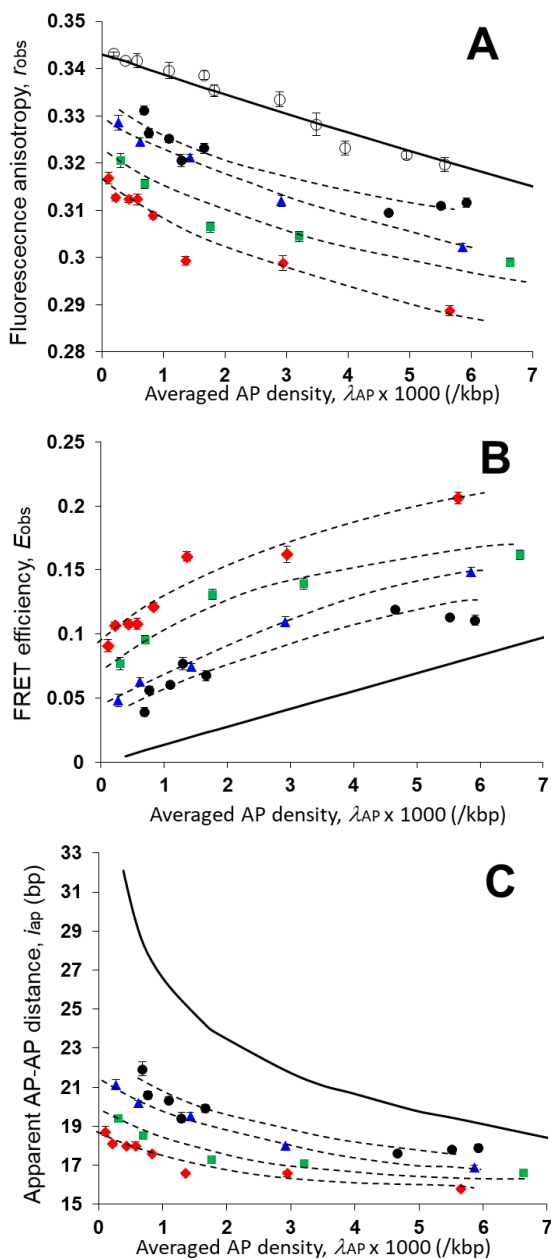


Fig. 2. Panel A: fluorescence anisotropy, Panel B: FRET efficiency, and Panel C: apparent distance between ^{60}Co γ -rays (\bullet), 2.0 MeV/u $^4\text{He}^{2+}$ (\blacktriangle), 0.52 MeV/u $^4\text{He}^{2+}$ (\blacksquare), and 0.37 MeV/u $^{12}\text{C}^{5+}$ (\blacklozenge) lesions as a function of AP density [4]. The open circles in Panel A indicate the data for the DNA incubated in the citrate buffer (pH 4.7) at 70 °C for the given period. The treatment is known to produce randomly distributed abasic sites (APs) on DNA.

separation at the lowest doses moderately reflects the degree of damage localization produced in a single radiation track.

This study primarily considers aldehyde/ketone moieties at APs as representative DNA lesions. However, ionizing radiation can produce a hundred types of lesions that incorporate APs. If lesions other than such electrophilic carbonyls are covalently labeled with a fluorescent dye, a variety of information will be obtained about the quality of the clusters at low doses.

The ultimate goal of this study is to understand the repair process of complex DNA damage by visualizing the damage itself and its subsequent biological processing. This study provides clear evidence for the existence of clusters using the photo-physicochemical method. However, the development of a labeling method for damaged genomic DNA in a cell and a technique to detect small FRET signals from a cluster is necessary to investigate the biological processing. Some high-resolution imaging techniques such as fluorescence anisotropy imaging microscopy (FAIM) will enable the observation of the repair process of a cluster.

Acknowledgments

The author thanks Drs. Naoya Shikazono and Takeshi Saito for supporting the overall experiments and γ -irradiation at the Institute for Integrated Radiation and Nuclear Science, Kyoto University. This work was supported by Grants-in-Aid for Scientific Research (for Scientific Research (C): 16K00551) from the Ministry of Education, Culture, Sports, Science, and Technology of Japan.

References

1. Akamatsu K, Shikazono N. A methodology for estimating localization of apurinic/apyrimidinic sites in DNA using fluorescence Resonance Energy Transfer. *Anal. Biochem.* 2013;433:171-180.
2. Akamatsu K, Shikazono N, Saito T. Localization estimation of ionizing radiation-induced abasic sites in DNA in the solid state using fluorescence Resonance Energy Transfer. *Radiat. Res.* 2015;183:105-113.
3. Akamatsu K, Shikazono N, Saito T. New method for estimating clustering of DNA lesions induced by physical/chemical mutagens using fluorescence anisotropy. *Anal. Biochem.* 2017;536:78-89.
4. Akamatsu K, Shikazono N, Saito T. Fluorescence anisotropy study of radiation-induced DNA damage clustering based on FRET. *Anal. Bioanal. Chem.* 2021;413:1185-1192.

Publication Lists

[Original Papers]

1. Double-Exposure Method with Synchrotron White X-ray for Stress Evaluation of Coarse-Grain Materials

Kenji Suzuki, Ayumi Shiro, Hidenori Toyokawa, Choji Saji, Takahisa Shobu
Quantum Beam Science, 4(3), 25, 2020-07, DOI:10.3390/qubs4030025

2. Antiphase oscillations in the time-resolved spin structure factor of a photoexcited Mott insulator

Kenji Tsutsui, Kazuya Shinjo, Takami Tohyama
Physical Review Letters, 126(12), 127404-1 - 127404-5, 2021-03, DOI:10.1103/PhysRevLett.126.127404

3. Multi-channel photodissociation and XUV-induced charge transfer dynamics in strong-field-ionized methyl iodide studied with time-resolved recoil-frame covariance imaging

F Allum, N Anders, M Brouard, P Bucksbaum, M Burt, B Downes-Ward, S Grundmann, J Harries, Y Ishimura, H Iwayama, L Kaiser, E Kukk, J Lee, XJ Liu, R S Minns, K Nagaya, A Niozu, J Niskanen, J O'Neal, S Owada, J Pickering, D Rolles, A Rudenko, S Saito, K Ueda, C Vallance, N Werby, J Woodhouse, D You, F Ziaee, T Driver
Faraday Discussions, 2020-11, DOI:10.1039/D0FD00115E

4. Proton beam quality enhancement by spectral phase control of a PW-class laser system

T. Ziegler, D. Albach, C. Bernert, S. Bock, F.-E. Brack, T. E. Cowan, N. P. Dover, M. Garten, L. Gaus, R. Gebhardt, I. Goethel, U. Helbig, A. Irman, H. Kiriya, T. Kluge, A. Kon, S. Kraft, F. Kroll, M. Loeser, J. Metzkes-Ng, M. Nishiuchi, L. Obst-Huebl, T. Püschel, M. Rehwald, H.-P. Schlenvoigt, U. Schramm, K. Zeil
Scientific Report, 11, 2021-03, DOI:10.1038/s41598-021-86547-x

5. 2020 roadmap on plasma accelerators

Félicie Albert, M E Couprie, Alexander Debus, Mike C Downer, Jérôme Faure, Alessandro Flacco, Leonida A Gizzi, Thomas Grismayer, Axel Huebl, Chan Joshi, M Labat, Wim P Leemans, Andreas R Maier, Stuart P D Mangles, Paul Mason, François Mathieu, Patric Muggli, Mamiko Nishiuchi, Jens Osterhoff, P P Rajeev, Ulrich Schramm, Jörg Schreiber, Alec G R Thomas, Jean-Luc Vay, Marija Vranic, Karl Zeil
New J. Phys., 23, 031101-1 - 031101-34, 2021-03, DOI:10.1088/1367-2630/abcc62

6. 赤外線レーザーを用いた採血のいらぬ血糖値センサー

山川 考一
化学工学, 85(2), 87 - 89, 2021-02

7. Fluctuating magnetism of Co- and Cu-doped NaFeAs

Jonathan Pelliciari, Kenji Ishii, Lingyi Xing, Xiancheng Wang, Changqing Jin
Applied Physics Letters, 118(11), 112604-1 - 112604-6, 2021-03, DOI:10.1063/5.0047264

8. Perpendicular magnetic anisotropy at the Fe/Au(111) interface studied by Mössbauer, x-ray absorption, and photoemission spectroscopies

Jun Okabayashi, Songtian Li, Seiji Sakai, Yasuhiro Kobayashi, Takaya Mitsui, Kiyohisa Tanaka, Yoshio Miura, Seiji Mitani
Physical Review B, 103, 104435, 2021-03, DOI:10.1103/PhysRevB.103.104435

9. EPR Theories for Selection Rules to Observe the Spin Gap

Toru Sakai
Applied Magnetic Resonance, 52, 507-521, 2020-10, DOI:10.1007/s00723-020-01298-8

10. Light reflectance and photoelectron yield spectroscopy enable acceptor level measurement in *p*-type Ba_{1-x}TiO₃ semiconductor

Saya Fujii, Jun Kano, Norihiro Oshime, Tohru Higuchi, Yuta Nishina, Tatsuo Fujii, Naoshi Ikeda, Hiromi Ota
Journal of Applied Physics, 129, 084105, 2021-02, DOI:10.1063/5.0033761

11. Ion Solvation and Water Structure in an Aqueous Sodium Chloride Solution in the Gigapascal Pressure Range

Toshio Yamaguchi, Nami Fukuyama, Koji Yoshida, Yoshinori Katayama
The Journal of Physical Chemistry Letters, 11(23), 250 - 256, 2020-12, DOI:10.1021/acs.jpcllett.0c03147

12. Post-growth annealing effects on charge and spin excitations in Nd_{2-x}Ce_xCuO₄

Kenji Ishii, Shun Asano, Masumi Ashida, Masaki Fujita, Biqiong Yu, Martin Greven, Jun Okamoto, Di-Jing Huang, Jun'ichiro Mizuki
Physical Review Materials, 5(2), 024803-1 - 024803-9, 2021-02, DOI:10.1103/PhysRevMaterials.5.024803

13. Feasibility Study of Magnetic-Domain Observation by Means of Non-Resonant Magnetic X-Ray Diffraction

Inami Toshiya, Shobu Takahisa, Ishii Kenji
IEEE Transactions on Magnetics, 57(3), 6400105, 2021-03, DOI:10.1109/TMAG.2020.3046006

14. Direct evidence of electronic ferroelectricity in YbFe₂O₄ using neutron diffraction and nonlinear spectroscopy

Fujiwara Kosuke, Fukada Yukimasa, Okuda Yohei, Seimiya Ryoto, Ikeda Naoshi, Yokoyama Keisuke, Yu Hue, Okimoto Yoichi,

Koshihara Seiya
Scientific Reports, 11, 4277, 2021-02, DOI:10.1038/s41598-021-83655-6

15. 過剰ドープ銅酸化物超伝導体における電荷秩序の探索

石井賢司, 浅野駿, 芦田万純, 藤田全基, 脇本秀一, 足立匡, 川股隆行, 小池洋二, 宮脇淳, 原田慈久, 水木純一郎
SPRING-8/SACLA 利用研究成果集, 9(1), 56 - 59, 2021-01, DOI:10.18957/rr.9.1.56

16. Analysis of Ly α dielectronic satellites to characterize temporal profile of intense femtosecond laser pulses

Sergey N. Ryazantsev, Igor Yu. Skobelev, Artem S. Martynenko, Mariya A. Alkhimova, Mikhail D. Mishchenko, Maxim V. Sedov, Tatiana A. Pikuz, Yuji Fukuda, Hiromitsu Kiriyama, Alexander S. Pirozhkov, Sergey A. Pikuz
Crystals, 11(2), 130-1 - 130-10, 2021-01, DOI:10.3390/cryst11020130

17. Emergence of low-energy electronic states in oxygen-controlled Mott insulator Ca₂RuO_{4+ δ}

Takeo Miyashita, Hideaki Iwasawa, Tomoki Yoshikawa, Shusuke Ozawa, Hironoshin Oda, Takayuki Muro, Hiroki Ogura, Tatsuhiro Sakami, Fumihiko Nakamura, Akihiro Ino
Solid State Communications, 326, 114180-1 - 114180-7, 2020-12, DOI:10.1016/j.ssc.2020.114180

18. Isotropic parallel antiferromagnetism in the magnetic field induced charge-ordered state of SmRu₄P₁₂ caused by *p-f* hybridization

Takeshi Matsumura, Shinji Michimura, Toshiya Inami, Chul-ho Lee, Masaaki Matsuda, Hironori Nakao, Masaichiro Mizumaki, Naomi Kawamura, Mitsuru Tsukagoshi, Satoshi Tsutsui, Hitoshi Sugawara, Kengo Fushiya, Tatsuma Matsuda, Ryuji Higashinaka, Yuji Aoki
Physical Review B, 102(21), 214444, 2020-12, DOI:10.1103/PhysRevB.102.214444

19. Polarization- and Strain- Mediated Control of Negative Thermal Expansion and Ferroelasticity in BiInO₃-BiZn_{1/2}Ti_{1/2}O₃

Takumi Nishikubo, Takahiro Ogata, Lalitha Kodumudi Venkataraman, Daniel Isaia, Zhao Pan, Yuki Sakai, Lei Hu, Shogo Kawaguchi, Akihiko Machida, Tetsu Watanuki, Yoichi Okimoto, Shin-ya Koshihara, Shigeo Mori, Jürgen Rödel, Masaki Azuma
Chemistry of Materials, 33(4), 1498 - 1505, 2021-02, DOI:10.1021/acs.chemmater.0c04049

20. Effects of conduction electron excitation on x-ray magnetic circularly polarized emission in itinerant ferromagnets

Akihiro Koide, Takuji Nomura, Toshiya Inami
Physical Review B, 102(22), 224425-1 - 224425-14, 2020-12, DOI:10.1103/PhysRevB.102.224425

21. Synchrotron Mössbauer Diffraction of Natural Iron Fe₃BO₆

Shin Nakamura, Takaya Mitsui, Yasuhiro Kobayashi, Masayuki Kurokuzu, Susumu Shimomura
Journal of the Physical Society of Japan, 89, 125001-1 - 125001-2, 2021-01, DOI:10.7566/JPSJ.89.125001

22. Magnetic Friedel Oscillation at the Fe(001) Surface: Direct Observation by Atomic-Layer-Resolved Synchrotron Radiation ⁵⁷Fe Mössbauer Spectroscopy

Takaya Mitsui, Seiji Sakai, Li Songtian, Tetsuro Ueno, Tetsu Watanuki, Yasuhiro Kobayashi, Ryo Masuda, Makoto Seto, Hisazumi Akai
Physical Review Letters, 125(23), 236806-1 - 236806-6, 2020-12, DOI:10.1103/PhysRevLett.125.236806

23. Demonstration of Transmission Mode Soft X-ray NEXAFS Using Third- and Fifth-Order Harmonics of FEL Radiation at SACLA BL1

Hiroshi Iwayama, Masanari Nagasaka, Ichiro Inoue, Shigeki Owada, Makina Yabashi, James R. Harries
Applied Sciences, 10(21), 7852, 2020-11, DOI:10.3390/app10217852

24. Development of carbon thin film for Laser-driven heavy ion acceleration using a XeCl excimer laser

Mitsuhiro Kusaba, Fumitaka Nigo, Kotaro Kondo, Mamiko Nishiuchi, Hironao Sakaki, Hiromitsu Kiriyama, Masaki Hashida, Shuji Sakabe
IEEJ Transactions on Electrical and Electronic Engineering, 103(11-12), 16 - 22, 2020-12, DOI:10.1002/ecj.12286

25. Generation of megatesla magnetic fields by intense-laser-driven microtube implosions

M. Murakami, J. J. Honrubia, K. Weichman, A. V. Arefiev, S. V. Bulanov
Scientific Reports, 10, 16653, 2020-10, DOI:10.1038/s41598-020-73581-4

26. Laser-driven generation of collimated quasi-monoenergetic proton beam using double-layer target with modulated interface

Martin Matys, Katsunobu Nishihara, Mariana Kecova, Jan Psikal, Georg Korn, Sergey V. Bulanov
High Energy Density Physics, 36, 10844, 2020-08, DOI:10.1016/j.hedp.2020.100844

27. Observation of gain coefficients of 15.47 nm Li-like Al soft x-ray laser in a recombining plasma pumped by a compact YAG laser

S. Namba, C. John, T. Morishita, N. Kubo, M. Kishimoto, N. Hasegawa, M. Nishikino
High Energy Density Physics, 36, 100790, 2020-08, DOI:10.1016/j.hedp.2020.100790

28. Soft X-ray spectrometers based on aperiodic reflection gratings and their application

E. N. Ragozin, E. A. Vishnyakov, A. O. Kolesnikov, Alexander Pirozhkov, A. N. Shatokhin
Physics-USpekhi, 2020-12, DOI:10.3367/UFNe.2020.06.038799

29. Electronic and crystal structures of $(\text{Na}_{1-x}\text{Ca}_x)\text{Cr}_2\text{O}_4$ with anomalous colossal magnetoresistance

Hitoshi Yamaoka, Eike F. Schwier, Yoshiya Yamamoto, Masashi Nakatake, Masahiro Sawada, Hiroya Sakurai, Naohito Tsujii, Masashi Arita, Hideaki Iwasawa, Munetaka Taguchi, Kenya Shimada, Jun'ichiro Mizuki
Physical Review B, 102, 235150, 2020-12, DOI:10.1103/PhysRevB.102.235150

30. Optimization and stabilization of a kilohertz laser-plasma accelerator

L. Rovige, J. Huijts, I. A. Andriyash, A. Vernier, M. Ouille, Z. Cheng, Takafumi Asai, Yuji Fukuda, V. Tomkus, V. Girdauskas, G. Raciukaitis, J. Dudutis, V. Stankevic, P. Gecys, R. Lopez-Martens, J. Faure
Physics of Plasmas, 28, 033105-1 - 033105-9, 2021-03, DOI:10.1063/5.0040926

31. High-resolution angle-resolved photoemission spectroscopy and microscopy

Hideaki Iwasawa
Electronic Structure, 2(4), 043001, 2020-12, DOI:10.1088/2516-1075/abb379

32. Effect of crystallization of Ni catalyst on direct precipitation of multilayer graphene using W capping layer

Jumpei Yamada, Yuki Ueda, Takahiro Maruyama, Seiji Fujikawa, Takuo Sasaki, Masamitsu Takahashi, Shigeo Naritsuka
Journal of Crystal Growth, 555, 125969, 2020-12, DOI:10.1016/j.jcrysgro.2020.125969

33. First-principles path-integral based molecular dynamics simulation of hydrogen hydrate in C_0 phase

Takashi Ikeda
Chemical Physics Letters, 763, 138222, 2020-11, DOI:10.1016/j.cplett.2020.138222

34. Dielectric continuum model examination of real-space electrostatic treatments

Yoshiteru Yonetani
Journal of Chemical Physics, 154(4), 044103, 2021-01, DOI:10.1063/5.0033053

35. The average and local structure of TiVCrNbD_x ($x = 0, 2.2, 8$) from total scattering and neutron spectroscopy

Magnus M. Nygård, Øystein S. Fjellvåg, Magnus H. Sørby, Kouji Sakaki, Kazutaka Ikeda, Jeff Armstrong, Ponniah Vajeeston, Wojciech A. Sławiński, Hyunjeong Kim, Akihiko Machida, Yumiko Nakamura, Bjørn C. Hauback
Acta Materialia, 205(15), 116496, 2020-12, DOI:10.1016/j.actamat.2020.116496

36. Mixed-valence state and structure changes of EuH_x ($x = 2$ and $2 < x \leq 3$) under high-pressure H_2 atmosphere

Keiji Kuno, Takahiro Matsuoka, Ryo Masuda, Takaya Mitsui, Makoto Seto, Akihiko Machida, Hiroshi Fujihisa, Naohisa Hirao, Yasuo Ohishi, Katsuya Shimizu, Shigeo Sasaki
Journal of Alloys and Compounds, 865(5), 158637, 2021-02, DOI:10.1016/j.jallcom.2021.158637

37. Ablation threshold and crater morphology of amorphous and crystalline SiO_2 glass for extreme ultraviolet femtosecond pulses

Tatsunori Shibuya, Kazuyuki Sakaue, Hiroshi Ogawa, Thanhhung Dinh, Daisuke Satoh, Eichi Terasawa, Masakazu Washio, Masahito Tanaka, Takeshi Higashiguchi, Masahiko Ishino, Yuya Kubota, Yuichi Inubushi, Shigeki Owada, Masaharu Nishikino, Yohei Kobayashi, Ryunosuke Kuroda
Japanese Journal of Applied Physics, 59(12), 122004-1 - 122004-3, 2020-11, DOI:10.35848/1347-4065/abc85a

38. Analysis of Glass Behavior of $\text{Lu}_2\text{Fe}_3\text{O}_7$ with Distributed Equivalent Circuit Model

Yukimasa Fukada, Ryota Fukuyama, Kosuke Fujiwara, Kenji Yoshii, Kei Shigematsu, Masaki Azuma, Naoshi Ikeda
Journal of the Physical Society of Japan (JPSJ), 90(2), 024710, 2021-01, DOI:10.7566/JPSJ.90.024710

39. Characterization of Accumulated B-Integral of Regenerative Amplifier Based CPA Systems

Stefan Bock, Franziska Marie Herrmann, Thomas Püschel, Uwe Helbig, René Gebhardt, Jakob Johannes Lötfering, Richard Pausch, Karl Zeil, Tim Ziegler, Arie Irman, Thomas Oksenhendler, Akira Kon, Mamiko Nishiuchi, Hiromitsu Kiriya, Kiminori Kondo, Toma Toncian, Ulrich Schramm
Crystals, 10(9), 847 - 869, 2020-09, DOI:10.3390/cryst10090847

40. Multiple Applications of Ion Beams in Life Science

Atsushi Tanaka
Quantum beam science, 3(4), 19 - 20, 2019-09, DOI:10.3390/qubs3040019

41. Effects of stress and plastic strain on hydrogen embrittlement fracture of a U-bent martensitic steel sheet

Yuki Shibayama, Tomohiko Hojo, Motomichi Koyama, Hiroyuki Saito, Ayumi Shiro, Ryo Yasuda, Takahisa Shobu, Takashi Matsuno, Eiji Akiyama
ISIJ International, 61, 1322 - 1329, 2021-01, DOI:https://doi.org/10.2355/isijinternational.ISIJINT-2020-569

42. Topological investigation of laser ion acceleration

Toshimasa Morita

43. Absolute response of a Fuji BAS-TR imaging plate to low-energy protons (< 0.2 MeV) and carbon ions (< 1 MeV)

Sadaoki Kojima, Tatsuhiko Miyatake, Shunsuke Inoue, Thanhung Dinh, Noboru Hasegawa, Michiaki Mori, Hironao Sakaki, Mamiko Nishiuchi, Nicholas P. Dover, Yoichi Yamamoto, Teru Sasaki, Fuyumi Itou, Kotaro Kondo, Takashi Yamanaka, Masaki Hashida, Shuji Sakabe, Masaharu Nishikino, Kiminori Kondo
Review of Scientific Instruments, 92(3), 033306, 2021-03, DOI:10.1063/5.0035618

44. Relativistic Doppler reflection of terahertz light from a moving plasma front in an optically pumped Si wafer

Nanase Kohno, Ryuji Itakura, Masaaki Tsubouchi
Physical Review B, 102(23), 235201-1 - 235201-9, 2020-12, DOI:10.1103/PhysRevB.102.235201

45. X-ray in situ observation of graphene precipitating directly on sapphire substrate with and without Ti capping layer

Shigeya Naritsuka, Jumpei Yamada, Yuki Ueda, Asato Nakashima, Tatsuya Kashio, Takahiro Maruyama, Seiji Fujikawa, Takuo Sasaki, Masamitsu Takahashi
Journal of Crystal Growth, 549, 125861-1 - 125861-9, 2020-11, DOI:10.1016/j.jcrysgro.2020.125861

46. Generation of α -Particle Beams With a Multi-kJ, Peta-Watt Class Laser System

Daniele Margarone, Alessio Morace, Julien Bonvalet, Yuki Abe, Vasiliki Kantarelou, Didier Raffestin, Lorenzo Giuffrida, Philippe Nicolai, Marco Tosca, Antonino Picciotto, Giada Petringa, Giuseppe A. P. Cirrone, Yuji Fukuda, Yasuhiro Kuramitsu, Hideaki Habara, Yasunobu Arikawa, Shinsuke Fujioka, Emmanuel D'Humieres, Georg Korn, Dimitri Batani
Frontiers in Physics, 8, 343-1, 2020-09, DOI:10.3389/fphy.2020.00343

47. Pressure-volume relationship of a Au-Al-Yb intermediate-valence quasicrystal and its crystalline approximant

Tetsu Watanuki, Akihiko Machida, Tsutomu Ishimasa
Materials Transactions, 62(3), 338 - 341, 2021-03, DOI:10.2320/matertrans.MT-MB2020006

48. Role of Nb in Improving the Cyclic Stability of V-Ti-Cr Alloys

Hyunjeong Kim, Kouji Sakaki, Kohta Asano, Daiju Matsumura, Akihiko Machida, Tetsu Watanuki, Tatsuo Noritake, Masakazu Aoki, Jin Nakamura, Tatsuya Fuura, Yumiko Nakamura
SPRING-8/SACLA Research Report, 8(2), 187 - 190, 2020-08, DOI:10.18957/tr.8.2.187

49. Effects of Residual Stress on Hydrogen Embrittlement of a Stretch-Formed Tempered Martensitic Steel Sheet

Hayato Nishimura, Tomohiko Hojo, Saya Ajito, Yuki Shibayama, Motomichi Koyama, Hiroyuki Saito, Ayumi Shiro, Ryo Yasuda, Takahisa Shobu, Eiji Akiyama
ISIJ International, 61, 1170-1178, 2020-12, DOI: <https://doi.org/10.2355/isijinternational.ISIJINT-2020-492>

50. Effects of Residual Stress and Plastic Strain on Hydrogen Embrittlement of a Stretch-Formed TRIP-aided Martensitic Steel Sheet

Tomohiko Hojo, Eiji Akiyama, Hiroyuki Saito, Ayumi Shiro, Ryo Yasuda, Takahisa Shobu, Junichiro Kinugasa, Fumio Yuse
Corrosion Science, 177, 108957, 2020-12, DOI:10.1016/j.corsci.2020.108957

51. High intensity laser driven oxygen source from CW laser heated titanium tape targets

Kotaro Kondo, Mamiko Nishiuchi, Hironao Sakaki, Nicholas Peter Dover, Hazel Frances Lowe, Takumi Miyahara, Yukinobu Watanabe, Tim Ziegler, Karl Zeil, Ulrich Schramm, Emma J. Ditter, George S. Hicks, Oliver C. Ettlenger, Zulfikar Najmudin, Hiromitsu Kiriya, Masaki Kando, Kiminori Kondo
Crystals, 10(9), 837 - 846, 2020-09, DOI:10.3390/cryst10090837

52. Initial oxidation kinetics of Si(113)-(3 \times 2) investigated using supersonic seeded molecular beams

S. Ohno, K. Tanaka, H. Kodama, M. Tanaka, A. Yoshigoe, Y. Teraoka
Surface Science, 697, 121600, 2020-07, DOI:10.1016/j.susc.2020.121600

53. Structural Dynamics of Adsorption Equilibrium for Iodine Adsorbed on Au(111)

Masashi Nakamura, Yuma Tanaka, Masamitsu Takahashi, Hiroo Tajiri, Osami Sakata, Nagahiro Hoshi
The Journal of Physical Chemistry C, 124(32), 17711 - 17716, 2020-08, DOI:10.1021/acs.jpcc.0c05330

54. High-thermal-conductivity SiC ceramic mirror for high-average-power laser system

Yasuhiro Miyasaka, Kotaro Kondo, Hiromitsu Kiriya
Crystals, 10(9), 831, 2020-09, DOI:10.3390/cryst10090831

55. Clinical trial of photodynamic therapy for peripheral-type lung cancers using a new laser device in a pilot study

Jitsuo Usuda, Tatsuya Inoue, Takaaki Tsuchida, Keishi Ohtani, Sachio Maehara, Norihiko Ikeda, Yoshinobu Ohsaki, Takaaki Sasaki, Kiyoshi Oka
Photodiagnosis and Photodynamic Therapy, 30, 101698, 2020-06, DOI:10.1016/j.pdpdt.2020.101698

56. Plasma channel formation in the knife-like focus of laser beam

O. G. Olkhovskaya, G. A. Bagdasarov, N. A. Bobrova, V. A. Gasilov, L. V. N. Goncalves, C. M. Lazzarini, M. Nevrkla, G. Grittani,

S. S. Bulanov, A. J. Gonsalves, C. B. Schroeder, E. Esarey, W. P. Leemans, P. V. Sasorov, S. Bulanov, G. Korn
Journal of Plasma Physics, 86(3), 905860307, 2020-06, DOI:10.1017/S0022377820000458

57. Tomographic reconstruction algorithms for structured gas density profiles of the targets for laser wakefield acceleration

S Lorenz, G Grittani, L V N Goncalves, C M Lazzarini, J Limpouch, M Nevrkla, S Bulanov, G Korn
Measurement Science and Technology, 31(8), 085205, 2020-05, DOI:10.1088/1361-6501/ab7cf5

58. Towards laser ion acceleration with holed targets

Prokopis Hadjisolomou, S. V. Bulanov, G. Korn
Journal of Plasma Physics, 86(3), 905860304, 2020-05, DOI:10.1017/S0022377820000379

59. Petawatt femtosecond laser pulses from titanium-doped sapphire crystal

Hiromitsu Kiriya, Alexander Pirozhkov, Mamiko Nishiuchi, Yuuji Fukuda, Akito Sagisaka, Akira Kon, Yasuhiro Miyasaka, Koichi Ogura, Nicholas Peter Dover, Kotaro Kondo, Hironao Sakaki, James Kevin Koga, Esirkepov Timur, Kai Huang, Nobuhiko Nakani, Masaki Kando, Kiminori Kondo, Stefan Bock, Tim Ziegler, Thomas Püschel, Karl Zeil, Ulrich Schramm
Crystals, 10(9), 783-1, 2020-09, DOI:10.3390/cryst10090783

60. X-ray microscope for imaging topological charge and orbital angular momentum distribution formed by chirality

Yoshiki Kohmura, Kei Sawada, Masaichiro Mizumaki, Kenji Ohwada, Tetsu Watanuki, Tetsuya Ishikawa
Optics Express, 28(16), 24115 - 24122, 2020-08, DOI:10.1364/OE.392135

61. Determination of Atomistic Deformation of Tricalcium Silicate Paste with High-Volume Fly Ash

Hyeonseok Jee, Sumin Im, Manabu Kanematsu, Hiroshi Suzuki, Satoshi Morooka, Taku Koyama, Akihiko Machida, Sungchul Bae
Journal of the American Ceramic Society, 103(12), 7188-7201, 2020-08, DOI:10.1111/jace.17404

62. Correction method for the energy spectrum of laser-accelerated protons measured by CR-39 track detectors with stepwise energy filters

Masato Kanasaki, Keita Sakamoto, Takafumi Asai, Satoshi Jinno, Satoshi Kodaira, Tomoya Yamauchi, Keiji Oda, Yuji Fukuda
High Energy Density Physics, 37, 100852, 2020-07, DOI:10.1016/j.hedp.2020.100852

63. Application of CR-39 Solid State Nuclear Track Detectors to Laser-Driven Ion Acceleration Experiments

Masato Kanasaki, Tomoya Yamauchi, Keiji Oda, Yuji Fukuda
Progress in Ultrafast Intense Laser Science XV, Topics in Applied Physics 136, 133-147, 2020-06, DOI:10.1007/978-3-030-47098-2_7

64. Spin-valley Hall phenomena driven by Van Hove singularities in blistered Graphene

M. Umar Farooq, Arqum Hashmi, Tomoya Ono, Li Huang
npj Computational Materials, 6(1), 1 - 8, 2020-12, DOI:10.1038/s41524-020-00470-9

65. Ising ferromagnetism and robust half-metallicity in two-dimensional honeycomb-kagome Cr2O3 layer

Arqum Hashmi, Kenta Nakanishi, Muhammad Umar Farooq, Tomoya Ono
npj 2d Materials and Applications, 4(1), 1 - 8, 2020-11, DOI:10.1038/s41699-020-00174-0

66. Local Linear Coupling between Polarization and Strain in KF-substituted Barium Titanate Crystals Probed by Brillouin Scattering and Dielectric Properties

Shinya Tsukada, Kenji Ohwada, Seiji Kojima, Yukikuni Akishige
Journal of the Physical Society of Japan, 89, 124702, 2020-11, DOI:10.7566/JPSJ.89.124702

67. Ion species discrimination method by linear energy transfer measurement in Fujifilm BAS-SR Imaging Plate

Mamiko Nishiuchi, Hironao Sakaki, Nicholas Peter Dover, Takumi Miyahara, Keiichi Shiokawa, Shunya Manabe, Tatsuhiko Miyatake, Kotaro Kondo, Keietsu Kondo, Yoshiyuki Iwata, Yukinobu Watanabe, Kiminori Kondo
Review of Scientific Instruments, 91(9), 093305, 2020-09, DOI:10.1063/5.0016515

68. Single-shot measurement of post-pulse-generated pre-pulse in high power laser systems

Akira Kon, Mamiko Nishiuchi, Hiromitsu Kiriya, Masaki Kando, Stefan Bock, Tim Ziegler, Thomas Püschel, Karl Zeil, Ulrich Schramm, Kiminori Kondo
Crystals, 10(8), 657 - 666, 2020-08, DOI:10.3390/cryst10080657

69. Dynamics of laser-driven heavy-ion acceleration clarified by ion charge states

Mamiko Nishiuchi, Nicholas Peter Dover, Masayasu Hata, Hironao Sakaki, Kotaro Kondo, Hazel Frances Lowe, Takumi Miyahara, Hiromitsu Kiriya, James Kevin Koga, Natsumi Iwata, Mariya Alkhlmova, Alexander Pirozhkov, Alatory Faenov, Pikuz Tatiana, Akito Sagisaka, Yukinobu Watanabe, Masaki Kando, Kiminori Kondo, Emma Jane Ditter, Oliver Ettliger, George Hicks, Najmudin Zufkar, Tim Ziegler, Karl Zeil, Ulrich Schramm, Yasuhiko Sentoku
Physical Review Research, 2(3), 033081, 2020-07, DOI:10.1103/PhysRevResearch.2.033081

70. New algorithm using L1 regularization for measuring electron energy spectra

Hironao Sakaki, Tomohiro Yamashita, Takashi Akagi, Mamiko Nishiuchi, Nicholas Peter Dover, Hazel Frances Lowe, Kotaro Kondo, Akira Kon, Masaki Kando, Yasuhiko Tachibana, Takayuki Obata, Keiichi Shiokawa, Tatsuhiko Miyatake, Yukinobu Watanabe

71. Characterization of laser-induced vibration on concrete surface toward highly efficient laser remote sensing

Noboru Hasegawa, Katsuhiko Mikami, Toshiyuki Kitamura, Hajime Okada, Shuji Kondo, Masaharu Nishikino
Japanese Journal of Applied Physics, 59(7), 076502-1 - 076502-9, 2020-07, DOI:10.35848/1347-4065/ab9849

72. Polarity reversal of wakefields driven by ultrashort pulse laser

P. Valenta, Esirkepov Timur, James Kevin Koga, A. Necas, G. M. Grittani, C. M. Lazzarini, O. Klimo, G. Korn, Sergey Bulanov
Physical Review E, 102, 053216-1 - 053216-5, 2020-11, DOI:10.1103/PhysRevE.102.053216

73. Laser resonance frequency analysis of pedicle screw stability: a cadaveric model bone study

Daisuke Nakashima, Katsuhiko Mikami, Shunsuke Kikuchi, Masaharu Nishikino, Toshiyuki Kitamura, Noboru Hasegawa, Morio Matsumoto, Masaya Nakamura, Takeo Nagura
Journal of Orthopaedic Research, 2021-02, DOI:10.1002/jor.24983

74. Reaction paths via a new transient phase in non-equilibrium hydrogen absorption of LaNi_2Co_3

Yumiko Nakamura, Kouji Sakaki, Hyunjeong Kim, Kohta Asano, Tetsu Watanuki, Akihiko Machida
International Journal of Hydrogen Energy, 45(41), 21655 - 21665, 2020-08, DOI:10.1016/j.ijhydene.2020.05.237

75. In-situ X-ray diffraction analysis of GaN growth on graphene-covered amorphous substrates

Seiya Fuke, Takuo Sasaki, Masamitsu Takahashi, Hiroki Hibino
Japanese Journal of Applied Physics, 59, 070902-1 - 070902-4, 2020-06, DOI:10.35848/1347-4065/ab9760

76. Hydrogen embrittlement resistance of pre-strained ultra-high-strength low alloy TRIP-aided steel

Tomohiko Hojo, Bakuya Kumai, Motomichi Koyama, Eiji Akiyama, Hiroyuki Waki, Hiroyuki Saitoh, Ayumi Shiro, Ryo Yasuda, Takahisa Shobu, Akihiko Nagasaka
International Journal of Fracture, 224(2), 253 - 260, 2020-06, DOI:10.1007/s10704-020-00451-5

77. Electromagnetic solitons in quantum vacuum

Sergey V. Bulanov, P. V. Sasorov, F. Pegoraro, H. Kadlecová, S. S. Bulanov, T. Zh. Esirkepov, N. N. Rosanov, G. Korn
Physical Review D, 101(1), 016016, 2020-06, DOI:10.1103/PhysRevD.101.016016

78. Hydrodynamic computational modelling and simulations of collisional shock waves in gas jet targets

Stylianios Passalidis, Oliver C. Ettliger, George S. Hicks, Nicholas Peter Dover, Zulfikar Najmudin, Emmanouil P. Benis, Evaggelos Kaselouris, Nektarios A. Papadogiannis, Michael Tatarakis, Vasilis Dimitriou
High Power Laser Science and Engineering, 8, e7, 2020-03, DOI:10.1017/hpl.2020.5

79. Picosecond burst pulse machining with temporal energy modulation

Akino Nakamura, Tomoki Mizuta, Yasuhiko Shimotsuna, Masaki Sakakura, Tomohito Otobe, Masahiro Shimizu, Kiyotaka Miura
Chinese Optics Letters, 18(12), 123801-1 - 123801-5, 2020-09, DOI:10.3788/COL202018.123801

80. Hydrogenation reaction of Co_3Ti alloy under high pressure and high temperature

Hiroyuki Saitoh, Masahiro Morimoto, Tetsu Watanuki, Toyoto Sato, Shigeyuki Takagi, Shin-ichi Orimo
International Journal of Hydrogen Energy, 45, 33675 - 33680, 2020-06, DOI:10.1016/j.ijhydene.2020.06.027

81. Single-shot electro-optic sampling on the temporal structure of laser wakefield accelerated electrons

Kai Huang, Hideyuki Kotaki, Michiaki Mori, Yukio Hayashi, Nobuhiko Nakanii, Masaki Kando
Crystals, 10(8), 640, 2020-07, DOI:10.3390/cryst10080640

82. Crystal and Magnetic Structures of Double Hexagonal Close-Packed Iron Deuteride

Hiroyuki Saitoh, Akihiko Machida, Riko Iizuka-Oku, Takanori Hattori, Asami Sano-Furukawa, Ken-ichi Funakoshi, Toyoto Sato, Shin-ichi Orimo, Katsutoshi Aoki
Scientific Reports, 10, 9934, 2020-06, DOI:10.1038/s41598-020-66669-4

83. Compact Thomson parabola spectrometer with variability of energy range and measurability of angular distribution for low-energy laser-driven accelerated ions

Sadaoki Kojima, Shunsuke Inoue, Thanh Hung Dinh, Noboru Hasegawa, Michiaki Mori, Hironao Sakaki, Yoichi Yamamoto, Teru Sasaki, Keiichiro Shiokawa, Kotaro Kondo, Takashi Yamanaka, Masaki Hashida, Shuji Sakabe, Masaharu Nishikino, Kiminori Kondo
Review of Scientific Instruments, 91, 1 - 11, 2020-05, DOI:10.1063/5.0005450

84. Electron temperature and soft x-ray intensity scaling in laser heavy element plasma interaction

Hiromu Kawasaki, Atsushi Sunahara, Yuta Shimada, Takeo Ejima, Tadashi Hatano, Weihua Jiang, Gerry O'Sullivan, Masaharu Nishikino, Shinichi Namba, Takeshi Higashiguchi
AIP Advances, 10(6), 065306, 2020-06, DOI:10.1063/5.0009946

85. Fluorescence Time Delay in Multistep Auger Decay as an Internal Clock

S Kosugi, F Koike, M Iizawa, M Oura, T Gejo, K Tamasaku, J Harries, R Guillemin, M N Piancastelli, M Simon

Physical Review Letters, 124(18), 183001, 2020-05, DOI:10.1103/PhysRevLett.124.183001

86. Photon scattering by a 4π -spherically-focused ultrastrong electromagnetic wave

Tae Moon Jeong, Sergey Bulanov, Pavel V. Sasorov, Georg Korn, James Kevin Koga, Stepan S. Bulanov
Physical Review A, 102, 023504-1 - 023504-14, 2020-08, DOI:10.1103/PhysRevA.102.023504

87. Photon Energy-Dependent Ultrafast Photoinduced Terahertz Response in a Microcrystalline Film of $\text{CH}_3\text{NH}_3\text{PbBr}_3$

Hiroto Okochi, Hiroyuki Katsuki, Masaaki Tsubouchi, Ryuji Itakura, Hisao Yanagi
The Journal of Physical Chemistry Letters, 11(15), 6068 - 6076, 2020-07, DOI:10.1021/acs.jpcllett.0c01393

88. Revisiting the Phase Diagram of T^* -type $\text{La}_{1-x/2}\text{Eu}_{1-x/2}\text{Sr}_x\text{CuO}_4$ using O K -edge X-ray Absorption Spectroscopy

Shun Asano, Kenji Ishii, Kohei Yamagami, Jun Miyawaki, Yoshihisa Harada, Masaki Fujita
Journal of the Physical Society of Japan, 89(6), 075002-1 - 075002-2, 2020-06, DOI:10.7566/JPSJ.89.075002

89. Local structure analysis around Ti in lead zirconate-titanate by X-ray fluorescence holography

Kouichi Hayashi, Cong Lu, Artoni Kevin R. Ang, Kenji Ohwada, Yujuan Xie, Wen Hu, Tomohiro Matsushita, Naohisa Happo, Shinya Hosokawa, Alexei A. Bokov, Zuo-Guang Ye
Physica Status Solidi B: Basic Solid State Physics, 257(11), 2000191, 2020-07, DOI:10.1002/pssb.202000191

90. Charge-separated spectra of suprathreshold highly charged bismuth ions in a dual laser-produced plasma soft x-ray source

Hiromu Kawasaki, Toshiki Tamura, Atsushi Sunahara, Masaharu Nishikino, Shinichi Namba, Gerry O'Sullivan, Takeshi Higashiguchi
Review of Scientific Instruments, 91(8), 086103, 2020-08, DOI:10.1063/5.0012225

91. Understanding water-mediated DNA damage production by molecular dynamics calculation of solvent accessibility

Yoshiteru Yonetani, Hiroshi Nakagawa
Chemical Physics Letters, 749, 137441, 2020-06, DOI:10.1016/j.cplett.2020.137441

92. 中赤外光パルスを用いた固体高次高調波発生とその偏光特性

石井 順久, 金島 圭佑, 夏 沛宇, 斎藤 成之, 金井 輝人, 板谷 治郎
レーザー研究, 48(4), 168 - 173, 2020-04

93. Unveiling Nanoscale Compositional and Structural Heterogeneities of Highly Textured $\text{Mg}_{0.7}\text{Ti}_{0.3}\text{H}_y$ Thin Films

Hyunjeong Kim, Herman Schreuders, Kouji Sakaki, Kohta Asano, Yumiko Nakamura, Naoyuki Maejima, Akihiko Machida, Tetsu Watanuki, Bernard Dam
Inorganic Chemistry, 59(10), 6800 - 6807, 2020-05, DOI:10.1021/acs.inorgchem.0c00059

94. Simultaneous Measurement of γ -ray and Conversion Electron Mössbauer Spectra of Fe Films under Total Reflection Conditions Using Synchrotron Mössbauer Source

Takaya Mitsui, Ko Mibu, Masaki Tanaka, Shinji Kitao, Yasuhiro Kobayashi, Ryo Masuda, Makoto Seto
Journal of the Physical Society of Japan, 89, 054707-1 - 054707-6, 2020-04, DOI:10.7566/JPSJ.89.054707

95. Soft x-ray laser beamline for surface processing and damage studies

Masahiko Ishino, Thanhhung Dinh, Yuji Hosaka, Noboru Hasegawa, Kimio Yoshimura, Hiroki Yamamoto, Tadashi Hatano, Takeshi Higashiguchi, Kazuyuki Sakaue, Satoshi Ichimaru, Masatoshi Hatayama, Akira Sasaki, Masakazu Washio, Masaharu Nishikino, Yasunari Maekawa
Applied Optics, 59(12), 3692 - 3698, 2020-04, DOI:10.1364/AO.387792

96. Laser-induced damage thresholds and mechanism of silica glass induced by ultra-short soft x-ray laser pulse irradiation

Katsuhiro Mikami, Masahiko Ishino, Thanhhung Dinh, Shinji Motokoshi, Noboru Hasegawa, Akira Kon, Yuichi Inubushi, Shigeki Owada, Hiroo Kinoshita, Masaharu Nishikino
Optics Letters, 45(8), 2435 - 2438, 2020-04, DOI:10.1364/OL.389288

97. Capturing roaming molecular fragments in real-time

Tomoyuki Endo, Simon P. Neville, Vincent Wanie, Samuel Beaulieu, Chen Qu, Jude Deschamps, Philippe Lassonde, Bruno E. Schmidt, Hikaru Fujise, Mizuho Fushitani, Akiyoshi Hishikawa, Paul L. Houston, Joel M. Bowman, Michael S. Schuurman, François Légaré, Heide Ibrahim
Science, 370(6520), 1072 - 1077, 2020-11, DOI:10.1126/science.abc2960

98. Optical parametric amplification of phase-stable terahertz-to-mid-infrared pulses studied in the time domain

Natsuki Kanda, Nobuhisa Ishii, Jiro Itatani, Ryusuke Matsunaga
Optics Express, 29(3), 3479 - 3489, 2021-02, DOI:10.1364/OE.413200

99. Optical probing of relativistic plasma singularities

Esirkepov Timur, Jie Mu, Yanjun Gu, Tae Moon Jeong, Petr Valenta, Ondrej Klimo, James Kevin Koga, Masaki Kando, David Neely, Georg Korn, Sergey Bulanov, Alexander Pirozhkov
Physics of plasmas, 27, 052103-1 - 052103-9, 2020-07, DOI:10.1063/5.0004525

- 100. Coherent strain evolution at the initial growth stage of AlN on SiC(0001) proved by in-situ synchrotron X-ray diffraction**
Hidetoshi Suzuki, Fumitaro Ishikawa, Takuo Sasaki, Masamitsu Takahashi
Applied Physics Express, 13, 055501-1 - 055501-5, 2020-04, DOI:10.35848/1882-0786/ab84bf
- 101. Localized character of charge excitations for $\text{La}_{2-x}\text{Sr}_x\text{NiO}_{4-\delta}$ revealed by oxygen *K*-edge resonant inelastic X-ray scattering**
Kohei Yamagami, Kenji Ishii, Yasuyuki Hirata, Keisuke Ikeda, Jun Miyawaki, Yoshihisa Harada, Masanori Miyazaki, Shun Asano, Masaki Fujita, Hiroki Wadati
Physical Review B, 102(16), 165145-1 - 165145-7, 2020-10, DOI:10.1103/PhysRevB.102.165145
- 102. Surface processing of PMMA and metal nano-particle resist by sub-micrometer focusing of coherent extreme ultraviolet high-order harmonics pulses**
Kazuyuki Sakaue, Hiroto Motoyama, Ryosuke Hayashi, Atsushi Iwasaki, Hidekazu Mimura, Kaoru Yamanochi, Tatsunori Shibuya, Masahiko Ishino, Thanhhung Dinh, Hiroshi Ogawa, Takeshi Higashiguchi, Masaharu Nishikino, Ryunosuke Kuroda
Optics Letters, 45(10), 2926 - 2929, 2020-06, DOI:10.1364/OL.392695
- 103. Neutron diffraction study on the deuterium composition of nickel deuteride at high temperatures and high pressures**
Hiroyuki Saitoh, Akihiko Machida, Takanori Hattori, Asami Sano-Furukawa, Ken-ichi Funakoshi, Toyoto Sato, Shin-ichi Orimo, Katsutoshi Aoki
Physica B, 587, 412153, 2020-06, DOI:10.1016/j.physb.2020.412153
- 104. セシウム含有モンモリロナイトの軟 X 線放射光光電子分光**
寺岡 有殿
電気学会論文誌 C, 140(4), 412 - 416, 2020-04, DOI:10.1541/ieejc.140.412
- 105. High-speed terahertz color imaging using a 100 kHz line scan camera**
Masaaki Tsubouchi, Keisuke Nagashima
Optics Express, 28(12), 17820 - 17831, 2020-06, DOI:10.1364/OE.394312
- 106. XeCl エキシマレーザを用いた高強度レーザ駆動重イオン加速用炭素薄膜の開発**
草場 光博, 兒子 史崇, 近藤 康太郎, 西内 満美子, 榊 泰直, 桐山 博光, 橋田 昌樹, 阪部 周二
電気学会論文誌 A, 140(8), 395 - 400, 2020-08, DOI:10.1541/ieejfms.140.395
- 107. Tensile deformation and recrystallization of aluminum single crystals with sub-grained structures studied by synchrotron X-ray radiation**
Ayumi Shiro, Tatsuya Okada, Takahisa Shobu
Mechanical Engineering Journal, 7(2), 19-00634, 2020-04, DOI:10.1299/mej.19-00634
- 108. 固体高分子形燃料電池コアシェル触媒 Pt の価電子帯電子状態観察による高活性化に関する研究**
原田 慈久, 丹羽 秀治, 干鯛 将一, 宮脇 淳, 木内 久雄, 尾嶋 正治, 石井 賢司
SPRING-8/SACLA 利用研究成果集, 8(2), 219 - 222, 2020-08, DOI:10.18957/rr.8.2.219
- 109. Demonstration of repetitive energetic proton generation by ultra-intense laser interaction with a tape target**
Nicholas Peter Dover, Mamiko Nishiuchi, Hironao Sakaki, Kotaro Kondo, M. A. Alkhimova, A. Ya. Faenov, M. Hata, N. Iwata, Hiromitsu Kiriyama, James Kevin Koga, Takumi Miyahara, T. A. Pikuz, Alexander Pirozhkov, Akito Sagisaka, Y. Sentoku, Y. Watanabe, Masaki Kando, Kiminori Kondo, Hazel Frances Lowe, E. J. Ditter, O. C. Ettlinger, G. S. Hicks, Z. Najmudin, U. Schramm, T. Ziegler, K. Zeil
High Energy Density Physics, 37, 100847, 2020-07, DOI:10.1016/j.hedp.2020.100847
- 110. Electron-positron pair creation in the electric fields generated by micro-bubble implosions**
James Kevin Koga, Masakatsu Murakami, Alexey V. Arefiev, Yoshihide Nakamiya, Stepan S. Bulanov, Sergey Bulanov
Physics Letters A, 384(34), 126854-1 - 126854-7, 2020-12, DOI:10.1016/j.physleta.2020.126854
- 111. 4pi-spherically focused Electromagnetic Wave: Diffraction Optics Approach and High-Power Limits**
Tae Moon Jeong, Sergey Bulanov, Pavel Sasorov, Stepan S. Bulanov, James Kevin Koga, Georg Korn
Optics Express, 28(9), 13991 - 14006, 2020-04, DOI:10.1364/OE.387654
- 112. Parametric attosecond pulse amplification far from the ionization threshold from high order harmonic generation in He^+**
C Serrat, J Seres, E Seres, T H Dinh, N Hasegawa, M Nishikino, S Namba
Optics Express, 28(16), 24243 - 24252, 2020-08, DOI:10.1364/OE.398595
- 113. Propagation of THz irradiation energy through aqueous layers: Demolition of actin filaments in living cells**
Shota Yamazaki, Masahiko Harata, Yuya Ueno, Masaaki Tsubouchi, Keiji Konagaya, Yuichi Ogawa, Goro Isoyama, Chiko Otani, Hiromichi Hoshina
Scientific Reports, 10, 9008, 2020-06, DOI:10.1038/s41598-020-65955-5
- 114. Role of Nonlinear Virtual Population for High Harmonic Generation in Solids**

Yasuyuki Sanari, Hideki Hirori, Tomoko Aharen, Hirokazu Tahara, Yasushi Shinohara, Kenichi L. Ishikawa, Tomohito Otobe, Peiyu Xia, Nobuhisa Ishii, Jiro Itatani, Shunsuke A. Sato, Yoshihiko Kanemitsu
Physical Review B, 102, 041125(R)-1 - 041125(R)-7, 2020-07, DOI:10.1103/PhysRevB.102.041125

115. Robust spin-orbit coupling induced semimetallic state in hyperkagome iridate $\text{Li}_3\text{Ir}_3\text{O}_8$

T. Takayama, A. N. Yaresko, A. S. Gibbs, K. Ishii, D. Kukusta, H. Takagi
Physical Review Materials, 4(7), 075002-1 - 075002-7, 2020-07, DOI:10.1103/PhysRevMaterials.4.075002

116. Observation of ultrafast impact ionization in diamond driven by mid-infrared femtosecond pulses

M. Kozak, M. Martinek, T. Otobe, F. Trojanek, P. Maly
Journal of Applied Physics, 128, 015701-1 - 015701-9, 2020-07, DOI:10.1063/5.0001983

117. Plane photoacoustic wave generation in liquid water using irradiation of terahertz pulses

Masaaki Tsubochi, Hiromichi Hoshina, Masaya Nagai, Goro Isoyama
Scientific Reports, 10, 18537, 2020-10, DOI:10.1038/s41598-020-75337-6

118. Relativistic flying forcibly oscillating reflective diffraction grating

Jie Mu, Timur Zh. Esirkepov, Petr Valenta, Yanjun Gu, Tae Moon Jeong, Alexander S. Pirozhkov, James K. Koga, Masaki Kando, Georg Korn, Sergei V. Bulanov
Physical Review E, 102, 053202, 2020-11, DOI:10.1103/PhysRevE.102.053202

119. Modifying angular and polarization selection rules of high-order harmonics by controlling electron trajectories in k-space

Yasuyuki Sanari, Tomohito Otobe, Yoshihiko Kanemitsu, Hideki Hirori
Nature Communications, 11, 3069-1 - 3069-7, 2020-06, DOI:10.1038/s41467-020-16875-5

120. Free-energy calculation of ribonucleic inosines and its application to nearest-neighbor parameters

Shun Sakuraba, Junichi Iwakiri, Michiaki Hamada, Tomoshi Kameda, Genichiro Tsuji, Yasuaki Kimura, Hiroshi Abe, Kiyoshi Asai
Journal of the Computational and Theoretical Chemistry, 16(9), 5925 - 5935, 2020-09, DOI:10.1021/acs.jctc.0c00270

121. Nucleosome unwrapping and unstacking

Hidetoshi Kono, Hisashi Ishida
Current Opinion in Structural Biology, 64, 119 - 125, 2020-10, DOI:10.1016/j.sbi.2020.06.020

122. Neutron crystallography of copper amine oxidase reveals keto/enolate interconversion of the quinone cofactor and unusual proton sharing

Takeshi Murakawa, Kazuo Kurihara, Mitsuo Shoji, Chie Shibazaki, Tomoko Sunami, Taro Tamada, Naomine Yano, Taro Yamada, Katsuhiko Kusaka, Mamoru Suzuki, Yasuteru Shigeta, Ryota Kuroki, Hideyuki Hayashi, Takato Yano, Katsuyuki Tanizawa, Motoyasu Adachi, Toshihide Okajima
Proceedings of the National Academy of Sciences of United States of America, 117(20), 10818 - 10824, 2020-05, DOI:10.1073/pnas.1922538117

123. Structural basis for an array of engrailed homeodomains

Tomoko Sunami, Yuu Hirano, Taro Tamada, Hidetoshi Kono,
Acta Crystallographica Section D, 76(9), 824 - 833, 2020-08, DOI:10.1107/S2059798320009237

124. Torsional stress can regulate the unwrapping of two outer half superhelical turns of nucleosomal DNA

Hisashi Ishida, Hidetoshi Kono
Proceedings of the National Academy of Sciences, 118(7), e2020452118, 2021-02, DOI:10.1073/pnas.2020452118

125. A common allosteric mechanism regulates homeostatic inactivation of auxin and gibberellin

Sayaka Takehara, Shun Sakuraba, Bunzo Mikami, Hideki Yoshida, Hisako Yoshimura, Aya Itho, Masaki Endo, Nobuhisa Watanabe, Takayuki Nagae, Makoto Matsuoka, Miyako Ueguchi-Tanaka
Nature communications, 11, 2143, 2020-05, DOI:10.1038/s41467-020-16068-0

126. Observation of water-window soft x-ray emission from laser-produced Au plasma under optically thin condition

Christian John, Maki Kishimoto, Yasuhiro Matsumoto, Takehiro Morishita, Takeshi Higashiguchi, Takuma Endo, Atsushi Sunahara, Tomoyuki Johzaki, Shinichi Namba
High Energy Density Physics, 37, 100845, 2020-11, DOI:10.1016/j.hedp.2020.100845

127. Fluorescence anisotropy study of radiation-induced DNA damage clustering based on FRET

Ken Akamatsu, Naoya Shikazono, Takeshi Saito
Analytical and Bioanalytical Chemistry, 413, 1185 - 1192, 2020-11, DOI:10.1007/s00216-020-03082-w

128. Participation of TDP1 in the repair of formaldehyde-induced DNA-protein cross- links in chicken DT40 cells

Toshiaki Nakano, Mahmoud I. Shoukamy, Masataka Tsuda, Hiroyuki Sasanuma, Kouji Hirota, Minoru Takata, Shin-ichiro Masunaga, Shunichi Takeda, Hiroshi Ide, Tadayoshi Bessho, Keizo Tano
PLOS ONE, 15(6), e0234859, 2020-06, DOI:10.1371/journal.pone.0234859

129. Strand with mutagenic lesion is preferentially used as a template in the region of a bi-stranded clustered DNA damage site in Escherichia coli

Naoya Shikazono, Ken Akamatsu
Scientific Reports, 10, 9737, 2020-06, DOI:10.1038/s41598-020-66651-0

130. Insight into the Formation Mechanism of "Unprotected" Metal Nanoclusters

Lifang Chen, Yulv Yu, Masako Kuwa, Tao Cheng, Yan Liu, Hiroshi Murakami, Masafumi Harada, Yuan Wang
Acta Physica-Chimica Sinica, 36(1), 1907008, 2020-08, DOI:10.3866/PKU.WHXB201907008

[Proceedings]

1. X線吸収分光法を用いた血清内アクチニドのキレート剤による除染評価

上原 章寛, 松村 大樹, 葉丸 晴子, 城 鮎美, 田中 泉, 辻 卓也, 齋藤 寛之, 石原 弘, 武田 志乃
Fundamental of Toxicological Sciences, Suppl 7, 147, 2020-11

2. Quantum spin nematic liquid in the S=1 antiferromagnetic chain with the biquadratic interaction

Toru Sakai
AIP Advances, 11, 015306-1 - 015306-4, 2021-01, DOI:10.1063/9.0000032

3. Recent developments in soft X-ray emission spectroscopy microscopy

寺内 正己, 羽多野 忠, 小池 雅人, ピロジコフ アレキサンダー, 笹井 浩行, 長野 哲也, 高倉 優, 村野 孝則
IOP Conference Series: Materials Science and Engineering, 891, 012022, 2020-08, DOI:10.1088/1757-899X/891/1/012022

4. Development of single-shot frequency-resolved optical gating for characterizing the instantaneous intensity and phase of LFEX laser pulses

Sadaoki Kojima, Yugo Ochiai, Shunsuke Inoue, Yasunobu Arikawa, Mao Takemura, Masaki Hashida, Shinsuke Fujioka, Shuji Sakabe
High Energy Density Physics, 37, 100855, 2020-11, DOI:10.1016/j.hedp.2020.100855

[表彰]

1. 創意工夫功労賞

「X線磁気円偏光発光のメカニズムを理論的に解明」

小出 明広
国立研究開発法人量子科学技術研究開発機構, 2021-03-26

2. 第15回(2021年)日本物理学会若手奨励賞

「強誘電体における電気分極由来の傾斜したバンド構造の研究」

押目 典宏
日本物理学会, 2021-03-13

3. 日本材料学会 令和2年度研究・開発賞

「放射光によるアルミニウム単結晶の引張変形挙動と内部ひずみ測定」

城 鮎美
日本材料学会 X線材料強度部門委員会, 2021-02-19

4. 日本物理学会学生優秀発表賞

「原子核乾板スタック内での多重クローン散乱過程を利用したサブ GeV 級レーザー加速陽子線評価手法の開発」

浅井 孝文
日本物理学会, 2020-10-10

5. 研究開発功績賞

「核共鳴蛍光散乱による核物質の非破壊検知測定技術開発」

森 道昭
日本原子力研究開発機構, 2020-10-01

6. OPTO2020 若手ポスター賞

“Study of SiC ceramic mirror for high-power laser system”

宮坂 泰弘
国立研究開発法人量子科学技術研究開発機構 関西光科学研究所、大阪大学レーザー科学研究所, 2020-09-29

7. OPTO2020 若手ポスター賞

「小型重粒子線加速器のためのレーザー駆動炭素イオンの高繰り返し発生」

小島 完興

大阪大学レーザー科学研究所 国立研究開発法人量子科学技術研究開発機構 関西光科学研究所, 2020-09-29

8. 日本材料学会 令和元年度論文賞

「二重露光法による粗大粒材の応力測定」

城 鮎美

日本材料学会, 2020-05-30

9. 量子生命科学会第2回大会 優秀発表賞

“Understanding the Dinucleosome Structural Dynamics at All Atom Resolution”

クマール アマラジート、松本 淳、河野 秀俊

量子生命科学会, 2020-12-23

[特許登録]

1. 組織識別装置、組織識別システム、組織識別方法、内視鏡システム、組織識別プログラムおよび記録媒体
山川 考一、青山 誠、森岡 孝満、今岡 達彦、小川 奏、特許第 6839400 号 (2021-02-17)

2. ラミナー型回折格子

小池 雅人、浮田 龍一、特許第 6695550 号 (2020-4-24)

3. 回折格子

今園 孝志、小池 雅人、長野 哲也、特許第 6700649 号 (2020-05-18)

[特許出願]

1. 磁化測定方法

稲見 俊哉、菅原 健人、綿貫 徹、小出 明広、野村 拓司、特願 2021-58759 (2021-03-30)

2. APPARATUS AND METHOD FOR MICROSCOPIC OBSERVATION OF MAGNETIC BODY

稲見 俊哉、菅原 健人、綿貫 徹、小出 明広、野村 拓司、米国出願 63/121,552 (2020-12-04)

3. 多孔性シリカを含むナノ粒子およびその製造方法、ならびに放射線治療用医薬組成物

玉野井 冬彦、松本 光太郎、齋藤 寛之、城 鮎美、田島 俊樹、PCT/JP2020/036367 (2020-9-25)

4. 合金、水素取出システム、水素吸蔵材、および合金の製造方法

山本 春也、齋藤 寛之、田口 富嗣、八巻 徹也、特願 2020-183096 (2020-10-30)

5. 磁化測定装置及び磁化測定方法

稲見 俊哉、菅原 健人、綿貫 徹、小出 明広、野村 拓司、特願 2021-002445 (2021-01-08)

6. 炭素イオン発生装置

近藤 康太郎、小島 完興、桐山 博光、西内 満美子、榊 泰直、橋田 昌樹、井上 俊介、特願 2020-183098 (2020-10-30)

7. 新規ヒトインターロイキン-18 変異体及びその用途

田中 義正、櫻庭 俊、特願 2021-19418 (2021-2-10)

The Kids' Science Museum of Photons

きつづ光科学館ふおとんは、新型コロナウイルスの感染拡大防止のため、(2020年2月27日より)臨時休館を続けています。2020年度については、臨時休館期間を利用して、工作の実演動画の発信、受付業務の練習や工作準備、新しくなったプラネタリウム機器の操作練習などに取り組んできました。

4月には、科学技術週間(4月13日~4月19日)に係るイベント登録に関連し、科学館で行っている工作の実演の動画をホームページ上で公開するなどの情報発信の取り組みも行い、第1弾として、三角万華鏡(ダイヤモンドスコープ)工作のビデオを撮影し公開しました。その後、蓄光スライム、UV Detector、光の三原色の影の体験、日光写真、UV レジン工作を「きつづ光科学館ふおとん on YouTube」にアップしました。



ふおとん YouTube チャンネル

<https://www.youtube.com/channel/UC2xgeump6cehlSreH7zjIBQ>



プラバン、レジン、キラキラツリー、万華鏡工作等の演習練習

10 月には、量研主催イベント等の開催自粛の緩和の決定を受け、科学館の一部再開（プラネタリウムの上映）に向け、アルコール等消毒液の確保、サーマルカメラやフロアマーキング、座席制限標の設置などを行い、11 月には、近隣の小学校 1 年生 4 クラスが、2 週 4 日にわたり来館、プラネタリウム（学習投影のための特別上映）を鑑賞いただきました。2020 年 2 月末の臨時休館開始以来、約 8 ヶ月ぶりの受入れとなりました。入館前の手指消毒や検温、間隔を空けての移動などに、ご協力いただきました。さらに、12 月には、2 年生 4 クラスに、プラネタリウムを鑑賞いただきました。今年度の入館者数は 300 人でした。



入館前の手指消毒



サーマルカメラによる検温



プラネタリウムドーム内



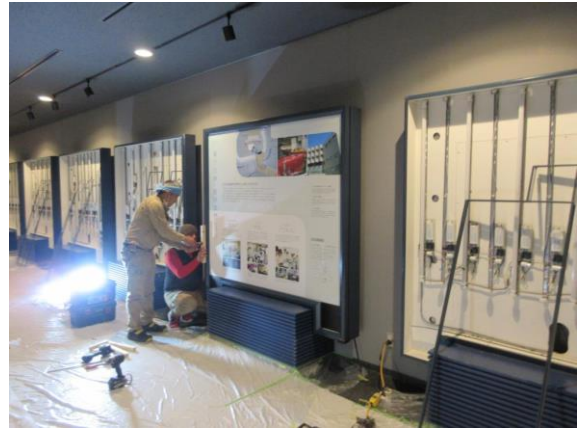
スタッフによる座椅子等の消毒作業

近隣の小学生の来館受入れの様子

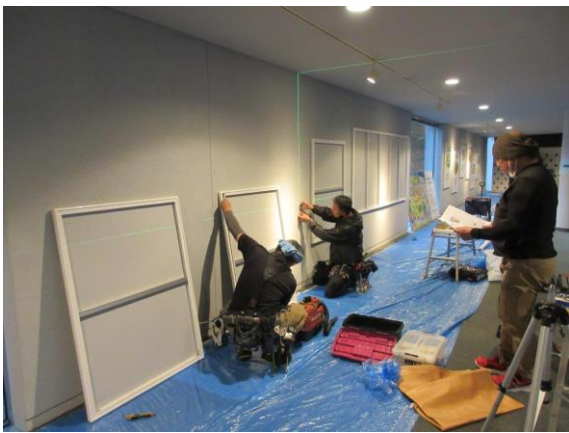
3 月には、広報課ならびに関西研庶務課とともに準備を進めてきた、展示コーナー（エネルギーコーナー、量研コーナー、フロンティアコーナー）のサイン（パネル等）更新のための改修作業が完了しました。エネルギーコーナーには、「地上に太陽を ー核融合エネルギーでつくる未来ー」のサインを新たに設置しました。量研コーナーについては、各部門の活動等を紹介する内容を更新するとともに、フロンティアコーナーには、「量子科学技術でつくる私たちの未来」（QST パンフレットにも掲載されています）を再編集して展示しました。



エネルギーコーナー



量研コーナー



フロンティアコーナー

科学館展示コーナーの改修

Appendix

共同研究課題、施設共用課題

1) 木津地区

【共同研究課題】

共同研究先	共同研究課題名	担当研究グループ
慶應義塾大学、近畿大学	レーザーを活用した整形外科インプラント設置強度評価機構の開発	X線レーザー研究グループ
㈱島津製作所	高耐性光学デバイスの開発研究	X線レーザー研究グループ
宇都宮大学、広島大学、東北大学	高輝度軟X線発生に関する基礎研究	X線レーザー研究グループ
九州大学	高効率フェムト秒レーザーアブレーションに関する基礎研究	X線レーザー研究グループ
京都大学	TW 級チタンサファイアレーザーを用いた量子ビーム発生に関する研究	X線レーザー研究グループ
奈良女子大学	レーザー誘起振動波計測への機械学習手法の適用に関する研究	X線レーザー研究グループ
㈱フォトンラボ	レーザー誘起振動波計測技術の小型化に関する研究	X線レーザー研究グループ
芝浦工業大学	レーザー誘起振動波計測技術の高度化に関する研究	X線レーザー研究グループ
建設技術研究所	レーザー誘起振動波計測技術によるコンクリート診断の高度化に関する研究	X線レーザー研究グループ
NTTアドバンステクノロジー㈱	高耐性力軟X線光学素子に関する基礎研究	X線レーザー研究グループ
東京学芸大学	リラクサー強誘電体のドメイン形成に関する研究	X線レーザー研究グループ
核融合科学研究所、京都工芸繊維大学、富山高等専門学校	凝縮相の量子・分子動力学計算に関する研究	X線レーザー研究グループ
京都大学	レーザー誘起弾性波技術によるインフラ構造物診断の高度化に関する研究	X線レーザー研究グループ
同志社大学	フェムト秒パルスレーザーの位相受動整合コヒーレント加算に関する研究	先端レーザー技術開発グループ
神戸大学	固体飛跡検出器を用いた高エネルギーイオン検出手法開発	先端レーザー技術開発グループ
神戸大学、名古屋大学	原子核乾板を用いた 100MeV 級レーザー加速プロトンの特性評価	先端レーザー技術開発グループ

京都大学	高強度レーザーと構造的媒質との相互作用に関する研究	先端レーザー技術開発グループ
大阪大学	宇宙物理の手法に基づく粒子加速・電磁放射に関する研究	先端レーザー技術開発グループ
大阪大学、東北大学	シンチレータを用いた相対論的イオン検出手法の開発	先端レーザー技術開発グループ
東京大学、神戸大学	水素クラスターをターゲットとした 100 MeV を超えるレーザー陽子加速の実証	先端レーザー技術開発グループ
東北大学、(株)島津製作所	極端紫外線領域の低入射角回折格子の開発	先端レーザー技術開発グループ
兵庫県立粒子線医療センター	量子メスに向けた粒子線照射計測及び制御技術に関する研究	高強度レーザー科学研究グループ
大阪大学	ステーjingレーザー加速の安定化研究	高強度レーザー科学研究グループ
大阪大学	超高強度レーザーと固体物質からのガンマ線発生及び核物理に関する研究	高強度レーザー科学研究グループ
理化学研究所	テラヘルツパルス光源による高分子高次構造の制御	超高速光物性研究グループ
大阪大学	高強度テラヘルツパルス光源による新規物質創成と新規物性発現に関する研究	超高速光物性研究グループ
奈良先端科学技術大学院大学	有機半導体におけるフォノン-励起子相互作用を利用した状態制御に関する基盤技術開発	超高速光物性研究グループ
東京大学	半古典 Vlasov 方程式に基づくレーザー加工シミュレータの研究開発	超高速光物性研究グループ
日本電信電話(株) NTT 物性科学基礎研究所	アト秒パルスの波形計測と時間分解計測に関わる基盤技術開発	超高速光物性研究グループ
東京大学	薄ディスクレーザー励起光パラメトリックチャープ増幅装置に関する研究開発	超高速光物性研究グループ
ライトタッチテクノロジー(株)	中赤外レーザーを用いたがん診断技術の開発	光量子科学研究部
ライトタッチテクノロジー(株)	中赤外レーザーを用いた非侵襲血糖値センサーの開発	光量子科学研究部
住友重機械工業(株)	量子メス用レーザー加速入射器の評価手法の開発	光量子科学研究部
日立造船(株)	量子メス用レーザー加速入射器のターゲット駆動装置に関する研究開発	光量子科学研究部
日本原子力研究開発機構	中性子散乱による生体高分子のダイナミクス解析に関する研究	生体分子シミュレーショングループ

【施設共用課題】

令和2年度施設共用課題

課題番号	利用区分	施設装置	利用課題
2020A-K01	公開	J-KAREN-P レーザー装置	非線形逆コンプトン散乱によるガンマ線渦の発生とらせん波面測定
2020A-K04	公開	J-KAREN-P レーザー装置	J-KAREN-P レーザーを用いた誘導コンプトン散乱の実験

2) 播磨地区

【共同研究課題】

共同研究先	共同研究課題名	担当研究グループ
物質・材料研究機構	原子二体分布関数法による機能性材料の先進的ナノ構造研究	高圧・応力科学研究グループ
京都大学	同位体特定による局所状態解明のための先進的メスbauer分光法の開発研究	磁性科学研究グループ
京都大学、分子科学研究所、理化学研究所	コヒーレント X 線を利用したナノ粒子計測に関する研究	コヒーレント X 線利用研究グループ
広島大学	コヒーレント X 線を利用した強誘電体一粒子計測	コヒーレント X 線利用研究グループ
京都大学	ナノ粒子を取り込んだがん細胞に及ぼす高エネルギー単色 X 線照射の影響に関する研究	高圧・応力科学研究グループ
JEF テクノリサーチ(株)	磁気円偏光発光を用いた方向性珪素鋼板の内部磁区観察のための研究開発	磁性科学研究グループ
日本原子力研究開発機構	放射光による物質科学に関する研究	放射光科学研究センター
産業技術総合研究所	水素雰囲気その場・時分割放射光 X 線全散乱を利用した水素吸蔵合金の構造変化の観測	高圧・応力科学研究グループ

【施設共用課題】

播磨地区では 2012 年度より文部科学省のナノテクノロジープラットフォーム事業を受託しており、放射光科学研究施設を成果公開型課題で利用する外部研究者に対して、特に専用ビームラインにおける研究支援を強化しています。課題は年 2 回、SPring-8 を運営する公益財団法人高輝度光科学研究センターの一般課題募集時期（5 月及び 11 月）に合わせて募集していますが、2020 年度は新型コロナウイルス感染症拡大防止のため、5 月の課題募集は行いませんでした。

令和2年度施設共用課題

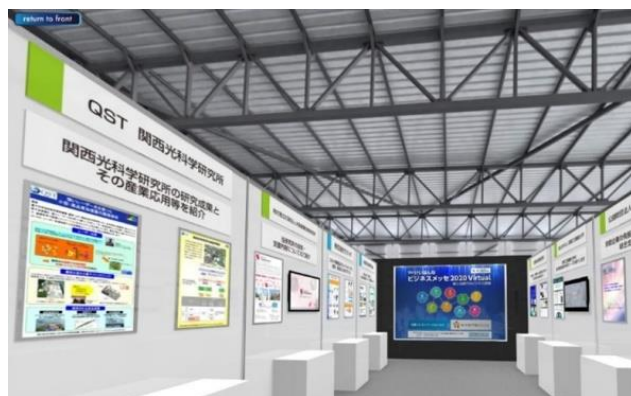
課題番号	利用区分	利用装置	研究課題
2020A-H02	公開	放射光メスbauer分光装置	放射光メスbauer分光を用いた高圧下での ϵ -FeOOHの鉄スピン転移の観察
2020A-H03	公開	放射光メスbauer分光装置	単分子磁石の磁気緩和過程探査のためのDy放射光メスbauer吸収分光法の開発研究
2020A-H04	公開	放射光メスbauer分光装置	放射光メスbauer回折による自然鉄試料のサイト選択的スペクトル測定(2)
2020A-H06	公開	共鳴X線非弾性散乱装置	範囲拡張EXAFSによるV/TiO ₂ およびヘテロポリ酸担持遷移金属触媒の構造解析
2020A-H07	公開	表面X線回折計	RF-MBE法による窒化物半導体成長初期過程のXRDその場観察
2020A-H08	公開	表面X線回折計	機械学習予測に基づく結晶成長その場制御のための基礎検討
2020A-H09	公開	表面X線回折計	ナノダイヤモンドを原料としたグラフェン析出成長のその場X線回折測定
2020A-H10	公開	表面X線回折計	六方晶窒化ホウ素上でのGa ₂ N結晶成長過程のリアルタイムX線回折
2020A-H11	公開	表面X線回折計	InGa ₂ N自立基板製作に向けたその場X線回折測定による成長制御
2020A-H12	公開	高温高圧プレス装置	六方晶鉄水素化物の最大水素量の決定
2020A-H13	公開	高温高圧プレス装置	FCC-YH ₃ 高圧相の元素置換による安定化メカニズムのin situ XRD解析
2020A-H14	公開	高温高圧プレス装置	高圧下水素化技術による鉄鋼材料の新奇無拡散相の探索
2020A-H15	公開	高温高圧プレス装置	超高圧水素化技術を活用した長周期積層(LPSO)合金の新規水素化物の合成
2020A-H16	公開	高温高圧プレス装置	水素9配位錯イオンの形成過程におけるLi ₂ O添加効果の解明
2020A-H17	公開	高温高圧プレス装置	水素吸蔵した高強度低合金TRIP鋼の残留オーステナイト変態挙動と引張変形時の相応力分配挙動の解析
2020A-H18	公開	高温高圧プレス装置	異種材料抵抗スポット溶接継手の熔融金属における3次元攪拌状態のIn-situ測定
2020A-H19	公開	ダイヤモンドアンビルセル回折計	溶接部深部の残留応力評価法の開発

2020A-H20	公開	ダイヤモンド アンビルセル回折計	高温型水素雰囲気下X線全散乱実験用試料セルの開発とそれを活用した新規発熱現象の理解2
2020A-H21	公開	ダイヤモンド アンビルセル回折計	加熱および载荷によるM-S-Hの構造解析および変形挙動特性の解明
2020A-H22	公開	ダイヤモンド アンビルセル回折計	Local structure investigation on metal-insulator transition and negative thermal expansion in Ca_2RuO_4
2020A-H23	公開	大型X線回折計	フェムト秒レーザーピーニングによってアルミニウム単結晶中に形成されたひずみ状態計測
2020A-H24	公開	大型X線回折計	レーザーピーニング加工試料の新しい回収手法と残留応力測定の実証
2020A-H25	公開	大型X線回折計	レーザー照射履歴を有する電子デバイス材料のX線回折実験
2020A-H26	公開	大型X線回折計	レーザー急冷法によるリラクサー強誘電体における不均一競合相の解明2
2020A-H27	非公開	共鳴X線非弾性散乱装置	RIXSを駆使した鉄鋼材料の水素吸蔵時における電子状態解明
2020A-H28	非公開	共鳴X線非弾性散乱装置	高分解能XRFおよび XAFSを駆使した $\text{Nd}_2\text{Fe}_{14}\text{B}$ 焼結磁石の磁性発現メカニズムの解明

関西光科学研究所での各種シンポジウム・施設公開・出展・アウトリーチ活動

新型コロナウイルス感染症の影響で、2020年度は対面での活動が大きく制限されました。そのような状況下ですが、関西研（木津地区、播磨地区）の各種シンポジウム、セミナー、研究会等について主なものを記載します。

例年、行っている年1回の施設公開（播磨地区（毎年4月ごろ）、木津地区（毎年10月ごろ））については、中止となりました。



けいはんなビジネスメッセ 2020 での仮想空間での出展

【木津地区】

1	29-SEP-2020	Web 開催	主催：大阪大学レーザー科学研究所、量研関西光科学研究所
	光・量子ビーム科学合同シンポジウム 2020 OPTO2020 Symposium on Photon and Beam Science		
2	27, 28-OCT-2020	Web 開催	主催：京都スマートシティエクスポ運営協議会、関西文化学術研究都市推進機構
	京都スマートシティエクスポ 2020、けいはんなビジネスメッセ 2020		

3	5-7-NOV-2020	Web 開催	主催：けいはんな R&D フェア 2020 実行委員会
	けいはんな R&D フェア 2020		
4	3-FEB-2021	Web 開催	主催：RIKEN-RAP & QST- KPSI
	第 4 回 RIKEN-RAP & QST-KPSI ジョイントセミナー		

【播磨地区】

1	12-15-JUL-2020	SPring-8 (兵庫県佐用郡佐用町)	主催：兵庫県立大学理学部／大学院物質理学研究科・生命理学研究科、関西学院大学理工学部・大学院理工学研究科、東京大学 放射光分野融合国際卓越拠点、岡山大学大学院自然科学研究科、大阪大学未来戦略光科学連携センター・蛋白質研究所・核物理研究センター、茨城大学大学院理工学研究科、(公財)高輝度光科学研究センター (JASRI)、理化学研究所 放射光科学研究センター、日本原子力研究開発機構 物質科学研究センター
	第 20 回 SPring-8 夏の学校		
2	21-AUG-2020	オンライン開催	主催：国立研究開発法人物質・材料研究機構微細構造解析プラットフォーム推進室
	微細構造解析プラットフォームワークショップ 2020		
3	3, 4-SEP-2020	オンライン開催	主催：国立研究開発法人物質・材料研究機構ナノテクノロジープラットフォームセンター
	文部科学省ナノテクノロジープラットフォーム令和 2 年度利用成果発表会		
4	15-SEP-2020	オンライン開催	主催：国立研究開発法人物質・材料研究機構ナノテクノロジープラットフォームセンター
	令和 2 年度文部科学省ナノテクノロジープラットフォーム学生研修プログラム成果発表会		
5	18-SEP-2020	オンライン開催	主催：SPring-8 ユーザー協同体 (SPRUC)、(公財)高輝度光科学研究センター、理化学研究所放射光科学研究センター
	SPring-8 シンポジウム 2020		
6	4-6-NOV-2020	オンライン開催 会場：高崎量子応用研究所	主催：国立研究開発法人量子科学技術研究開発機構
	第 4 回 QST 国際シンポジウム 4th QST International Symposium —Innovation from Quantum Materials Science—		
7	11-13-NOV-2020	幕張メッセ国際展示場 (千葉県千葉市)	主催：一般社団法人日本分析機器工業会、一般社団法人日本科学機器協会
	Japan Analytical & Scientific Instruments Show (JASIS) 2020		
8	20-NOV-2020	オンライン開催	主催：日本顕微鏡学会
	日本顕微鏡学会 第 63 回シンポジウム「顕微鏡オンラインフォーラム 2020」 共催セッション「微細構造解析プラットフォーム特別講演会 (成果事例報告)」		

9	3-DEC-2020	オンライン開催	主催：AIST 微細構造解析プラットフォーム、 JAEA 微細構造解析プラットフォーム、QST 微細構造解析プラットフォーム
			文部科学省ナノテクノロジープラットフォーム微細構造解析プラットフォーム 令和2年度第1回地域セミナー：産総研-原子力機構-量研合同セミナー
10	9-11-DEC-2020	オンライン開催 会場：東京ビッグサイト	主催：nano tech 2021 実行委員会
		第20回国際ナノテクノロジー総合展・技術会議（nano tech 2021）	
11	11-DEC-2020	オンライン開催 会場：東京ビッグサイト	主催：文部科学省ナノテクノロジープラットフォーム、国立研究開発法人物質・材料研究機構ナノテクノロジープラットフォームセンター
		文部科学省ナノテクノロジープラットフォーム第19回ナノテクノロジー総合シンポジウム JAPAN NANO 2021 マテリアル革新力強化のための次世代プラットフォーム	
12	21-DEC-2020	オンライン開催	QST 微細構造解析プラットフォーム、JAEA 微細構造解析プラットフォーム
		令和2年度文部科学省ナノテクノロジープラットフォーム事業 JAEA&QST 微細構造解析プラットフォーム放射光設備利用講習会 ―反応解析とバルク・表面の構造解析―	
13	8-10-JAN-2021	オンライン開催	主催：第34回日本放射光学会年会・放射光科学合同シンポジウム組織委員会
		第34回日本放射光学会年会・放射光科学合同シンポジウム	
14	5-MAR-2021	オンライン開催	主催：京大微細構造解析プラットフォーム最先端構造観察・計測共用拠点、QST 微細構造解析プラットフォーム、JAEA 微細構造解析プラットフォーム、産総研微細構造解析プラットフォーム
		令和2年度文部科学省ナノテクノロジープラットフォーム事業京大・産総研・JAEA・QST 微細構造解析プラットフォーム合同地域セミナー「最新の微細構造・反応解析」	
15	31-JAN-2021	オンライン開催	主催：国立研究開発法人物質・材料研究機構ナノテクノロジープラットフォームセンター
		令和2年度文部科学省ナノテクノロジープラットフォーム技術スタッフ交流プログラム報告会	

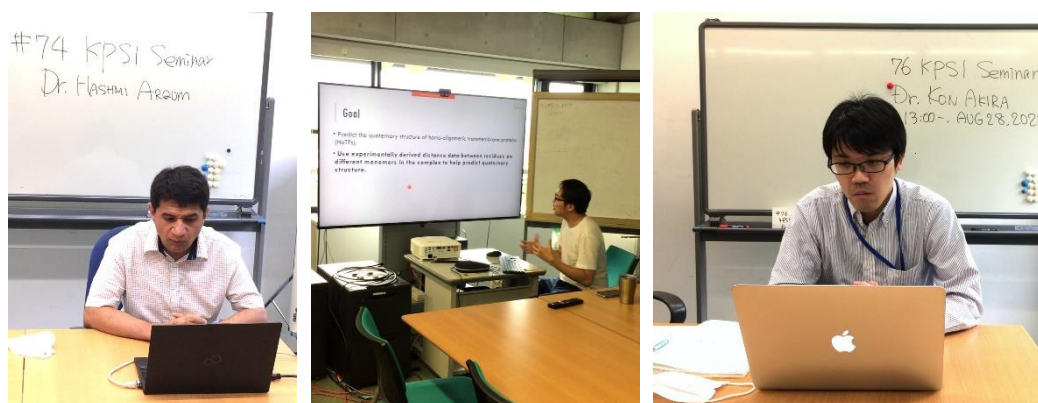
KPSI セミナー（第74回～78回）

QST 木津地区では国内外の著名な研究者をお招きして学術的に最先端の専門的なセミナーを開催しています。今年度は合計5回、全て Web によるセミナーを開催しました。開催にあたっては KPSI Web サイトやメーリングリストを活用し、関西研内外に開催案内を行っています。また報告については Web サイト、関西研だより等を活用しています。（参加費無料・事前登録制）

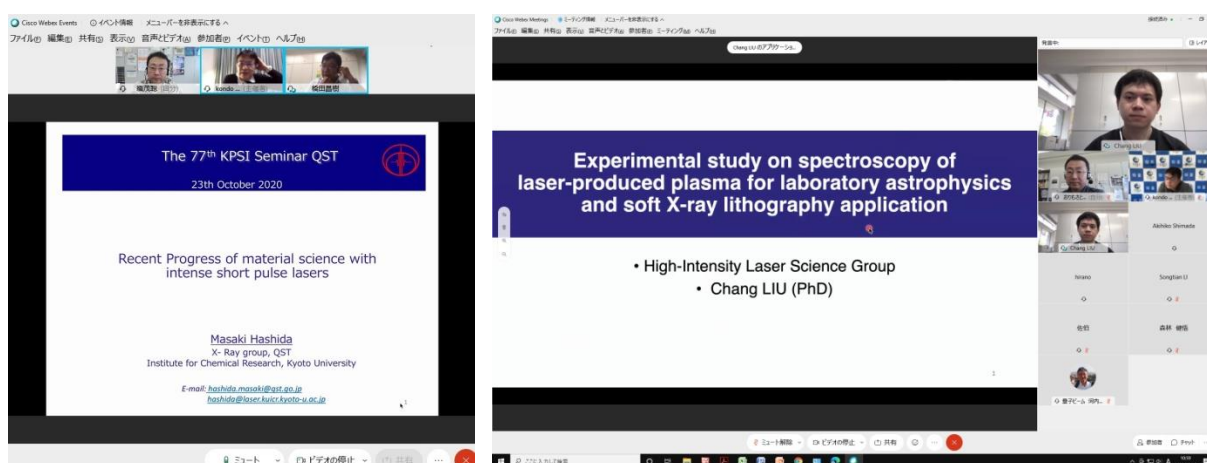
Web サイト：<https://www.qst.go.jp/site/kansai-topics/29853.html>

74	16-JUL-2020	Dr. Hashmi Arqum	Ultrafast Dynamics Group, QST
			Theory and modelling of low dimensional materials
75	30-JUL-2020	Dr. Chan Wai Soon	Molecular Modeling and Simulation Group, QST

	Predicting the Quaternary Structures of Homo-Oligomeric Transmembrane Proteins (HoTPs)		
76	28-AUG-2020	Dr. KON Akira	Department of Advanced Photon Research, QST
	Single-shot measurement of pre-pulse generated by post-pulse		
77	19-OCT-2020	Dr. HASHIDA Masaki	Advanced Research Center for Beam Science Institute for Chemical Research, Kyoto University/ Department of Advanced Photon Research, QST
	Recent progress of material science with intense short pulse lasers		
78	10-MAR-2021	Dr. Chang Liu	High-Intensity Laser Science Group, QST
	Experimental study on spectroscopy of laser-produced plasma for laboratory astrophysics and soft X-ray lithography application		



左から、第 74 回、第 75 回、第 76 回 (Web 配信場所の様子)



左から、第 77 回、第 78 回の発表題目 (Web 配信・パソコンモニター表示)

QST 播磨セミナー（第 15 回～第 21 回）

播磨地区では国内外の著名な研究者をお招きして学術的に最先端の専門的なセミナーを開催していますが、2020 年度は新型コロナウイルス感染症防止対策のため、QST 播磨地区に常勤する研究者のセミナーとしました。

15	23-September-2020	Dr. Fujiwara Kosuke	Magnetism Research Group, QST
Structural transition near room temperature owing to the short-range magnetic ordering in the electronic ferroelectric RFe_2O_4			
16	21-October-2020	Dr. Norihiro Oshime	High Pressure Science and Stress Research Group, QST
Direct observation of skewed band structure induced by electric polarization in ferroelectrics			
17	25-November-2020	Dr. Iwase Hideaki	Magnetism Research Group, QST
Local electronic structure explored by spatially-resolved ARPES			
18	23-December-2020	Dr. Akihiro Koide	Magnetism Research Group, QST
Theoretical calculation for x-ray magnetic circularly polarized emission			
19	27-January-2021	Dr. Takaya Mitsui	Magnetism Research Group, QST
Investigations on local magnetic properties of magnetic thin films using synchrotron-radiation Mössbauer spectroscopy			
20	24-February-2021	Dr. James Harries	Coherent X-ray Research Group, QST
Using the effect of fluorescence on post-collision interaction as an attosecond stopwatch - a new method for observing inner-shell dynamics on the attosecond timescale -			
21	24-March-2021	Dr. Takashi Ikeda	Condensed Matter Theory Group, QST
First principles centroid molecular dynamics simulation of high pressure ices			



第 16 回、第 17 回の発表題目（Web 配信・パソコンモニター表示）

S-cube（スーパーサイエンスセミナー）

中学高校生を中心に一般の方に光科学についての理解を深めていただくことを目的に、第一線の研究者による講義「S-cube（エスキューブ：スーパーサイエンスセミナー）」を開講しています。

2020年度は新型コロナウイルス感染症の感染拡大防止と感染リスクの低減を図るため、開催しておりません。

Web サイト：<https://www.qst.go.jp/site/kansai-topics/29911.html>

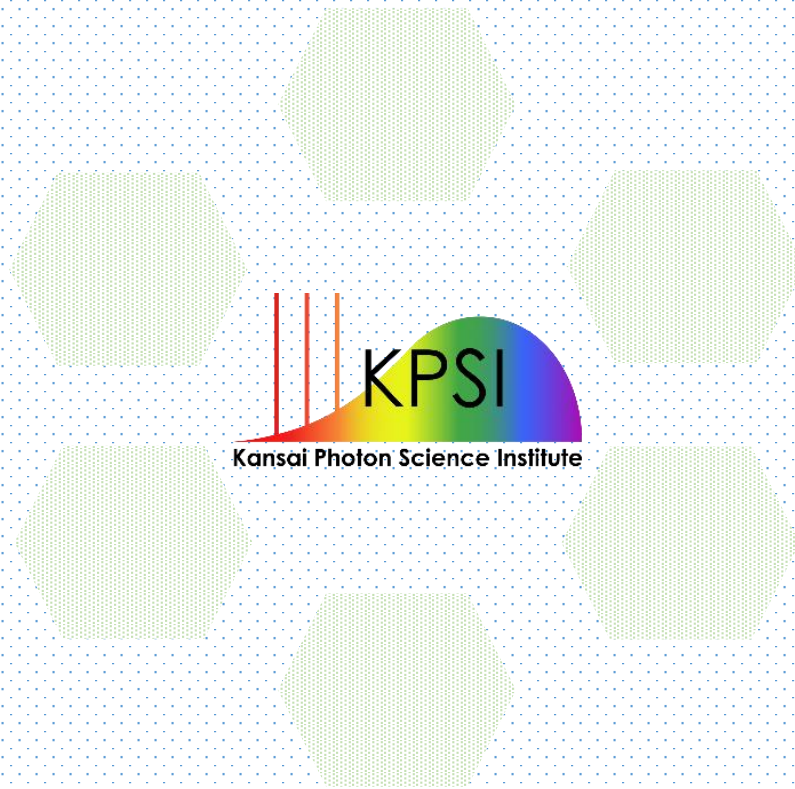
関西光科学研究所2020年度年報
KPSI Annual Report 2020

【発行】
2021(令和3)年6月

【編集・発行】
国立研究開発法人量子科学技術研究開発機構
関西光科学研究所 管理部庶務課

【印刷】
株式会社 春日

©2021 国立研究開発法人量子科学技術研究開発機構



Kansai Photon Science Institute
Quantum Beam Science Research Directorate
National Institutes for Quantum and Radiological Science and Technology

8-1-7, Umemidai, Kizugawa-shi, Kyoto 619-0215, Japan
<https://www.qst.go.jp/site/kansai-english/>